Toward Using Membrane Distillation for Brine Treatment: Understanding Energy Efficiency and the Challenge of Mineral Scaling

By

Kofi S. S. Christie

Dissertation
Submitted to the Faculty of the
Graduate School of Vanderbilt University
in partial fulfillment of the requirements
for the degree of

DOCTOR OF PHILOSOPHY
in
Environmental Engineering

May 8th, 2020
Nashville, Tennessee

Approved:
Shihong Lin, Ph.D.
Alan Bowers, Ph.D.
G. Kane Jennings, Ph.D.
Florence Sanchez, Ph.D.
Tiezheng Tong, Ph.D.

For my family

who helped me keep a positive mental attitude

ACKNOWLEDGEMENTS

I couldn't have made it to this point without the support from my encouraging advisor, Shihong Lin. His guidance has been critical to my progress. As the very first PhD student to join his research group, I was educated on both how to carry out the investigation of strong research questions and how to build and lead a research group, and I expect to apply the lessons that he has taught me about patience, tenacity, and flexibility to my future career endeavors. I am also extraordinarily grateful to the other lab members in our research group who have helped to enrich my graduate school training with long conversations about science, news, and everything in between. Thank you Zhangxin Wang, Li Wang, Yuanzhe Liang, Yu-Xi Huang, Drew Horseman, Ruoyu Wang, and Rui Chen. I would also like to thank the visiting researchers who have passed through our lab and broadened my outlook on potential research directions throughout the years.

The research engineers and technicians that work in the Civil and Environmental Engineering (CEE) Department deserve my deepest gratitude. Thank you Rossane DeLapp, Rich Teising, Dalesha Blackwell, Lesa Brown, and Deela McGill for helping me with my experiments. Also, I very much appreciate the work of the past and present administrative and facilities staff members of CEE Department and of Featheringill/Jacobs Hall, including Karen Fuller, Beverly Piatt, Charity Hasty, Tonya Brown, Lewis Saettel, and Jackie White.

I consider myself fortunate to have encountered several vibrant groups of graduate students at Vanderbilt University who have truly made the good times great and the bad times bearable. Whether at softball games, community service events, half-marathons, chess matches, or weekend hangouts, I am glad to have spent time with ValaRae Partee, Cole Brubaker, Nate Barnes, Ross Dingwall, Kevin Lubin, Jade Bing, Abraham Liddell, Ashley Jones, and Brittany Allison. I am also deeply indebted to the professors and staff members throughout Vanderbilt University who have helped me along the way. Thank you, Gene LeBoeuf, James Clarke, Douglas LeVan, Paul Laibinis, Don Brunson, Doug Adams, Ruth Schemmer, and Sheri Kimble, for your support.

One of my most enjoyable challenges during my graduate school experience was teaching. I am thankful to the staff and administrators of the School for Science and Math at Vanderbilt, the Vanderbilt Institute of Nanoscale Science and Engineering, and Programs for Talented Youth for giving me the opportunity to mentor and to teach K-12 students. This includes David Dunn, Emilie Hall, Sarah DeLisle, Sarah Ross, Greg Walker, and Angela Eeds.

I am immensely grateful to the friends that I have made outside of Vanderbilt University who have nodded politely while I talk about the details of my research and have made my time in Nashville enjoyable. I do not have the words necessary to express how deeply I have cherished being a part of the DTB crew. Every Tuesday Night Skate, every Sunday Blade, every kayaking trip, every hot yoga session, every Colorado Road Trip, every “What Year Is It” weekend at Woodward, every trip to Chattanooga, Memphis, and the Smokey Mountains, and, most of all, every second that I have spent within the four walls of Asphalt Beach Inline Skate Shop. Thank you Steve Larios, Cameron Martin, Julian Mire, Zach Leavell, Ethan Pugh, Joseph Pachacos, Austin Black, Brandon Harden, Taylor Popham, Tony Woodland, Andrew Kingery, Read Davis, Marshall Bolton, Dagger, Chris Kelley, Kai Parkerson, and Geo Navarette.

I must thank the friends who have helped to make my experience in Music City musical. Thank you to all of the artists who have inspired me, and thank you to each of the following friends who decided against good judgement to start a band with me: Claudia Dunn and Izzy Ramos of Tourettes, Adam Martin, Nick McKenzie, and Aziz Nooh of T-34, and Dale Kirk and Aziz Nooh (again) of Tre. I promise I’ll practice more often.

Lastly, I’d like to acknowledge the members of my immediate family who have gone above and beyond to provide me with the reassurance and confidence necessary to complete my doctoral degree. Oral, Ornell, Omari, and Malikah Christie, I love you guys. Thank you for always having my back.

TABLE OF CONTENTS

Page

Chapter

3. Distinct Behaviors between Gypsum and Silica Scaling in Membrane Distillation 48

4. Decoupling the Effects of Feed Temperature and Water Flux on Gypsum Scaling in Membrane Distillation 65

5. Conclusions and Future Work 82

LIST OF TABLES

Page

LIST OF FIGURES

NOMENCLATURE

Abbreviation or symbol	**Description**
ZLD	Zero-liquid discharge
MSF	Multistage flash distillation
RO	Reverse osmosis
MD	Membrane distillation
DCMD	Direct-contact membrane distillation
HX	Heat exchanger
α	Flow rate ratio (i.e., the ratio between the distillate flow rate and feed flow rate)
α^*	Critical flow rate ratio
η_{th}	Thermal efficiency, i.e., the percentage of trans-membrane heat transfer that is contributed by the transfer of latent heat
η_{ws}	Waste-heat utilization efficiency
$\eta_{ws,k}$	Waste-heat utilization efficiency for the kth stage
c_F	Specific heat capacity of the feed solution
c_D	Specific heat capacity of the distillate
c_{ws}	Specific heat capacity of the waste heat stream
GOR	Gained output ratio
$\bar{h}_{vap}$	Enthalpy of vaporization (i.e., latent heat)
P_{th}	(Thermal) power of heat absorbed in the heat source
$P_{th,max,ws}$	(Thermal) power of the available heat in the waste heat stream
Q_D	Distillate flow rate
Q_F	Feed flow rate
Q_{ws}	Flow rate of the waste heat stream
ΔQ	Change of either feed or distillate stream flow rate (they are the same), which is also the cross-membrane vapor flow rate.
ΔQ_{max}	Maximum cross-membrane vapor flow rate
R	Water recovery in a single pass
R_{max}	Maximum water recovery in a single pass
R_{max}^{DLR}	Maximum water recovery in a single pass when the system is in distillate limited regime
R_{max}^{FLR}	Maximum water recovery in a single pass when the system is in feed limited regime
SEC_{th}	Specific thermal energy consumption, i.e., energy consumed to generate a unit mass of distillate
$SEC_{th,k}$	Specific thermal energy consumption for the kth stage
SY	Specific yield
ΔT	Temperature difference between the influent temperatures of the feed and distillate streams (i.e., $T_H - T_C$)
T_C	Influent temperature of the feed stream
T_H	Influent temperature of the distillate stream

ΔT_{HS}	Temperature gain of the feed stream after going through the heat source (=$T_H - T_{mix}$)
ΔT_{HX}	Temperature difference between the hot and cold streams in the HX
ΔT_{MD}	Trans-membrane difference in the DCMD module
T_{mix}	Temperature of the stream obtained from mixing the feed water and the effluent of the MD feed stream
$T_{ws,i}$	Influent temperature of the waste heat stream
$T_{ws,\mathrm{e}}$	Effluent temperature of the waste heat stream

CHAPTER 1

1. Introduction

1.1. Motivation

Water scarcity is a grand global challenge. The United Nations estimates that over 2 billion people live in areas with high water stress, and over 3.5 billion people live in areas with severe water scarcity during at least 1 month per year. Access to clean water is heavily impacted by extreme weather events, rapid urbanization, and aquifer depletion, so this number is expected to rise beyond 5 billion people by 2050.[1] In water-stressed areas, populations extract most of the available fresh water from conventional sources like surface waters (i.e., rivers, lakes, and streams) and groundwater and must rely on the local cycle of rain to replenish these natural sources.

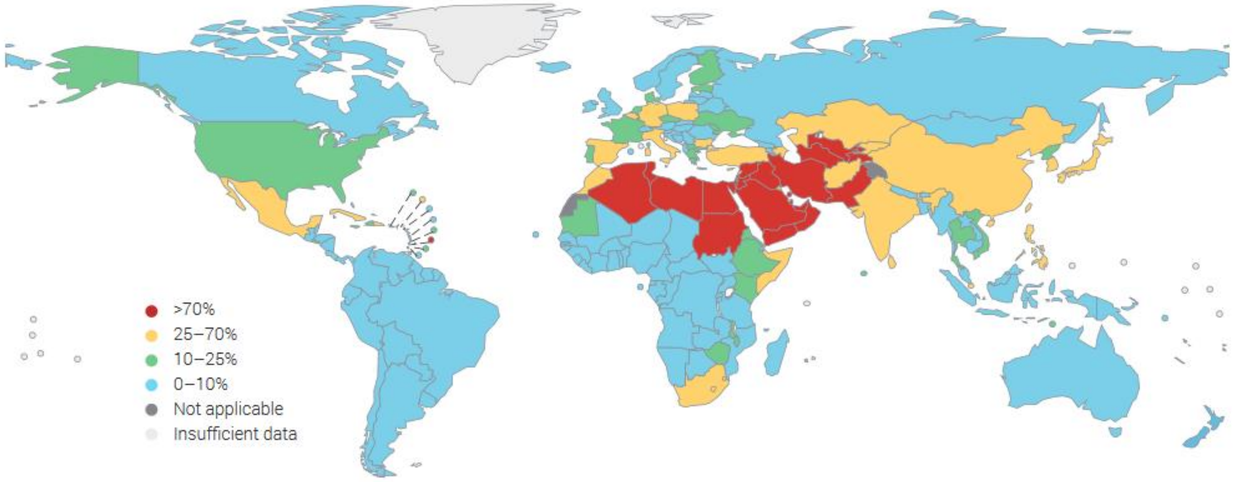

Figure 1.1 – Global physical water stress, defined as the ratio of total freshwater withdrawn annually by all major sectors, including environmental water requirements, to the total amount of renewable freshwater resources, expressed as a percentage.[1]

To deal with the growing inaccessibility of fresh water, many localities can improve their water usage efficiency by encouraging the transition away from water-intense agricultural and lifestyle practices and by transferring water into the locality from distant areas that have water surpluses.[2] However, the relative benefit from improving water usage efficiency may not meet future demands, especially as developing nations face pressures to broaden agricultural options, not narrow them, and to reduce costs in such a way that will make piping in water from other areas prohibitive.

One way that we can augment and slow down the rapid decline of our global supply of surface water is through the desalination of saline sources like seawater, brackish groundwater, and industrial wastewater to produce fresh water. Aligned with this effort is the zero-liquid discharge (ZLD) principle, an emerging framework that has gained interest recently for both the reduction in the volume of freshwater consumed by industrial facilities and the improvement of environmental stewardship. Facilities in the power generation industry, chemical and electronics manufacturing industries, and inland desalination industry are the primary targets for ZLD mandates by municipalities,[3] and they are targeted because they typically discharge brine into evaporation ponds, surface waters, deep well injection sites, land application sites, or municipal wastewater treatment facilities.[4] These short-term solutions may have long-term consequences including ecosystem shock, increased burden on public resources, and even seismic activity.[5,6] The increasing recognition of the value of ZLD necessitates the development of sustainable liquid separation technologies, especially those that are capable of efficiently treating highly saline brine streams.[7]

Many nations today, such as Saudi Arabia and Israel, provide a majority of their inhabitants' water through wastewater reuse and desalination.[8] Arid nations like these in the Middle East were early adopters of thermal desalination strategies such as multistage flash distillation (MSF) and pressure-driven strategies such as reverse osmosis (RO). While these technologies have been greatly expanded over the last several decades, large amounts of energy are still needed to desalinate brine for potable use,[9] and it is of great advantage to optimize desalination processes such that the lowest-cost energy can be utilized with the highest efficiency.[9–12] There currently exists an urgent need for the further development of sustainable water treatment technologies. Membrane distillation (MD), a thermal liquid separation strategy of growing interest, has been targeted as a promising technique for desalination due to its numerous advantages over MSF and RO, including greater resistance to fouling, reduced need for pretreatment, the ability to be operated sustainably when coupled with waste heat or renewable heat sources, and improved product water quality.[13]

1.2. Objectives and Approach

The efficient application of MD for brine treatment is influenced by the source of thermal energy, the operating parameters chosen, and the resistance to process failure by fouling and wetting. The purpose of this work is to quantitatively investigate 1) optimization of the efficiency of water production during MD, 2) the mechanisms of mineral scaling and wetting during MD, and 3) the effect of operating parameters on the acceleration or delay of mineral scaling during MD. The central hypothesis of this work states that MD performance, and therefore the competent application of MD, will depend heavily on:

- The appropriate understanding of the value of latent heat recovery and the utilization of waste heat to drive MD
- The composition of the MD feed water and the appropriate understanding of the specific attachment mechanisms of the nucleating species
- The improved understanding of the role of MD operating parameters in scaling mitigation

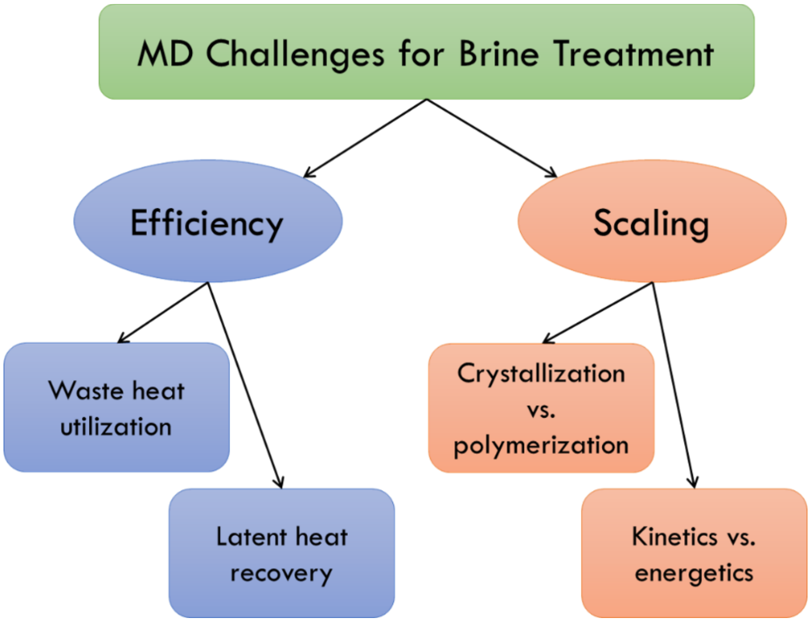

Figure 1.2 – Scope of dissertation

1.3. Structure of Dissertation

This thesis is directed toward addressing two of the greatest challenges surrounding the widespread application of MD for brine treatment: efficiency and scaling.[14,15] Following the above objectives and approach, this dissertation is divided into five chapters.

In Chapter 2, an intuitive analysis is presented to clarify the differences between the various operating regimes employed for MD and to expose problematic assumptions surrounding the application of latent heat recovery and waste heat coupling in MD systems. Based on the principle of equal heat capacity flows, we derive a simple expression for the optimal flow rate ratio between the feed and distillate streams to best recover latent heat. Following the principle of energy balance, we derive simple expressions for the specific thermal energy consumption (SEC_{th}) and gained output ratio (GOR) of DCMD with and without a coupled HX for latent heat recovery, revealing an intuitive critical condition that indicates whether DCMD should or should not be coupled with HX. A new metric, namely specific yield, is proposed to quantify the performance of DCMD powered by waste heat stream.

In Chapter 3, a comparative analysis is presented to differentiate the distinct mechanisms and consequences of different types of scalants in MD. Several characterization techniques (i.e. scanning electron microscopy, energy-dispersive X-ray spectroscopy, electrical impedance spectroscopy, and tensile strength testing) were used to compare gypsum scaling and silica scaling and to determine that their mechanistic differences can result in dramatically different impacts on membrane performance.

In Chapter 4, the individual effects of water flux and feed temperature on gypsum scaling in MD are systematically evaluated. By conducting two series of MD experiments to isolate the independent effects of water flux and feed temperature, then analyzing the critical water recovery at the point of flux decline (the generally accepted gypsum induction point), conclusions are drawn about the sensitivity of gypsum induction to either operating parameter. The influence of both temperature polarization and concentration polarization are considered through simple calculations based in established mass and heat transfer theory. The thermodynamic stability of the system is quantified using saturation index, and the energetic driving force for gypsum nucleation is considered using the Gibbs free energy for nucleation.

Finally, Chapter 6 provides a summary of this dissertation. The novelty and broader impact of the presented work is discussed. Then, by bringing together all of the reported information from each preceding chapter and synthesizing the conclusions and implications of the findings collectively, considerations for future work are presented.

CHAPTER 2

2. Energy Efficiency of Membrane Distillation: Simplified Analysis, Heat Recovery, and the Use of Waste Heat

A version of this work was published in *Environmental International* in 2020. Permission for reproduction in this dissertation was granted.

https://doi.org/10.1016/j.envint.2020.105588

2.1. Introduction

Membrane distillation (MD) is a thermally-driven liquid separation process which shows promise for desalination and the treatment of highly saline wastewater.[13,16,17] In direct contact MD (DCMD), a microporous and hydrophobic membrane is used to separate a heated feed solution and a cool distillate solution. Water vapor passes across the MD membrane from the feed solution to the distillate solution due to a partial vapor pressure difference between the two streams. Unlike reverse osmosis in which the applied pressure must exceed the brine osmotic pressure and thus become unpractical with high-salinity feed solution, the applicability of MD is less sensitive to feed salinity due to the relatively weak dependence of partial vapor pressure on salinity. This advantage, along with the fact that MD can be operated using low-grade waste heat, contribute to the interest in MD for desalination, hypersaline brine management, and zero liquid discharge.[18–23]

As water vapor crosses the membrane in MD, the transfer of heat and mass are fundamentally connected. The mass transfer rate across the membrane is driven by the membrane permeability and the partial vapor pressure gradient, which is predominantly a function of temperature. Heat is transferred across the membrane with the vapor via convection, where the rate is governed by the vapor flux, and via conduction through the vapor-membrane system, where the rate is a function of the system's thermal conductivity. An abundance of literature has been presented on the investigation of simultaneous heat and mass transfer across the MD boundary layers.[24–30] They often involve the resolution of large systems of coupled equations for which the results give accurate predictions of how varying membrane properties and operating conditions affect the transmembrane vapor flux. These studies have even been confirmed in benchtop experiments with membrane coupons[27,29,31–34].

The rigorous heat and mass transfer modelling in the aforementioned studies does not readily extend to an analysis of overall energy expenditure in MD, especially on the module scale. While studies have compared the energy efficiency of common MD configurations[35,36], module scale analysis is important because industrial application of MD requires much larger membrane surface areas and the effect of the temperature drop along the module is typically overlooked.[37–42] Module scale modelling is also important because energy consumption in MD typically exceeds that of other non-thermal desalination processes,[41,43,44] so industrial application of MD hinges upon successful measures of latent heat recovery. Previous studies that have explored the MD-HX system[45–53] lack the simplicity required to build an intuitive understanding of the tradeoffs and opportunities inherent within the typical range of operation. Further, the clarity surrounding the discussion of heat energy utilization and process efficiency can be improved. That is, the grand scheme regarding how energy efficiency should be analyzed is still missing.

In this work, we present a module-scale thermodynamic analysis to explore the energy efficiency of direct contact membrane distillation (DCMD) through the introduction of simplified thermodynamic criteria for MD design and operation. We evaluate energy consumption in MD with and without a coupled HX system to recover latent heat from condensation in the distillate stream. We also consider the energy efficiency and waste-heat source energy utilization efficiency when operating MD with and without coupled HX for latent heat recovery with a waste-heat stream as the heat source (as theorized for industrial application). We apply reasonable simplifying assumptions to the MD process to demonstrate how the key parameters in MD behave on the module scale. Our analysis establishes a framework for evaluating the thermodynamic efficiency of the MD process and facilitates an intuitive understanding of how operational and configurational decisions affect the energy efficiency of MD.

2.2. Simplified Thermodynamic Criteria for MD Design and Operation

Before performing energy efficiency analysis for an MD system, we would like to first re-visit the basic criteria for optimizing design and operation of a module-scale DCMD system and system's performance limit based on thermodynamics. While these principles have been presented before in more rigorous forms, the goal of the discussion here is to simplify the governing equations of these principles to impart an intuitive understanding with minimal loss of accuracy. The first step in assembling the relationships necessary to evaluate the thermodynamic limits of MD performance is to describe the system of governing equations that can represent the mass and heat transfer within the MD module:

$$\frac{dQ_F(x)}{dx} = \frac{A_{MD}}{L_{MD}} K_{m,MD} [T_F(x) - T_D(x) - \Delta T_{th}(x)] \qquad \text{Eq. 2.1}$$

$$\frac{dQ_D(x)}{dx} = \frac{A_{MD}}{L_{MD}} K_{m,MD} [T_F(x) - T_D(x) - \Delta T_{th}(x)] \qquad \text{Eq. 2.2}$$

$$\frac{d[Q_F(x) h_L(C(x), T_F(x))]}{dx} = \frac{dQ_F(x)}{dx} \left[h_{vap}\left(C(x), T_F(x)\right) + h_L\left(0, T_F(x)\right)\right] + \frac{A_{MD}}{L_{MD}} \zeta_F(x) \qquad \text{Eq. 2.3}$$

$$\frac{d[Q_D(x) h_L(0, T_D(x))]}{dx} = \frac{dQ_D(x)}{dx} \left[h_{vap}\left(0, T_D(x)\right) + h_L\left(0, T_D(x)\right)\right] + \frac{A_{MD}}{L_{MD}} \zeta_D(x) \qquad \text{Eq. 2.4}$$

Where $\frac{dQ(x)}{dx}$ is the differential mass flowrate through either the feed or distillate channel (designated with an "F" or "D" subscript, respectively) with x as the axial position within the MD module, A_{MD} is the active area of the MD membrane, L_{MD} is the length of the active membrane area, $K_{m,MD}$ is the empirical mass transfer coefficient in the DCMD process, $T_F(x)$ is the feed stream temperature at position x, $T_D(x)$ is the distillate stream temperature at position x, $\Delta T_{th}(x)$ is the threshold temperature difference, h_{vap} is the specific enthalpy of vaporization of a saline solution, h_L is the specific enthalpy of a saline solution, and $\zeta(x)$ is the conductive heat flux at the membrane-solution interface. The threshold temperature difference ($\Delta T_{th}(x)$) accounts for the fact that the presence of solute in the feed solution lowers the partial vapor pressure of water at the feed-membrane interface.[54] The trans-membrane partial vapor pressure difference vanishes when delT reaches $\Delta T_{th}(x)$ and mass transfer is halted. Mathematically, $\Delta T_{th}(x)$ is given by:

$$\Delta T_{th}(x) = T_F^*(x) - T_D(x) \qquad \text{Eq. 2.5}$$

Where $T_F^*(x)$ is the threshold feed temperature defined such that:

$$p_W\big(C(x), T_F^*(x)\big) = p_W\big(0, T_D(x)\big) \qquad \text{Eq. 2.6}$$

Where p_W is the partial vapor pressure of water as a function of temperature and solute concentration, and $C(x)$ is the solute concentration of the feed at position x. That is, the feed stream at temperature $T_F^*(x)$ and concentration $C(x)$ has the same partial vapor pressure as the distillate stream ($C(x) = 0$) at temperature $T_D(x)$. The p_W expression above represents the condition of zero driving force. Similarly, $\Delta T_{th}(x)$ can also be defined as:

$$\Delta T_{th}(x) = T_F(x) - T_D^*(x) \qquad \text{Eq. 2.7}$$

Where $T_F^*(x)$ is the threshold feed temperature defined such that:

$$p_W\big(C(x), T_F(x)\big) = p_W\big(0, T_D^*(x)\big) \qquad \text{Eq. 2.6}$$

The boundary conditions for the system of equations (Eqs. 1-4) which describe the mass and heat transfer within the MD module are given as:

$$Q_F(L_{MD}) = Q_F^0 \qquad \text{Eq. 2.7}$$

$$Q_D(0) = Q_D^0 \qquad \text{Eq. 2.8}$$

$$T_F(L_{MD}) = T_F^0 = T_H \tag{Eq. 2.9}$$

$$T_D(0) = T_D^0 = T_C \tag{Eq. 2.10}$$

Where T_H and T_D are the working temperatures of the heated stream and the cooled stream for MD operation. If the membrane is a perfect thermal insulator, then $\zeta_F(x)$ approaches zero while $\zeta_D(x)$ approaches $J_m c_{p,V}(T_F - T_D)$. For this ideal case, the system of differential equations that govern the heat and mass transfer through the MD module simplifies to:

$$\frac{dQ_F(x)}{dx} = \frac{A_{MD}}{L_{MD}} K_{m,MD}[T_F(x) - T_D(x) - \Delta T_{th}(x)] \tag{Eq. 2.11}$$

$$\frac{dQ_D(x)}{dx} = \frac{A_{MD}}{L_{MD}} K_{m,MD}[T_F(x) - T_D(x) - \Delta T_{th}(x)] \tag{Eq. 2.12}$$

$$\frac{d[Q_F(x) h_L(C(x), T_F(x))]}{dx} = \frac{dQ_F(x)}{dx}\left[h_{vap}\big(C(x), T_F(x)\big) + h_L\big(0, T_F(x)\big)\right] \tag{Eq. 2.13}$$

$$\begin{aligned} &\frac{d[Q_D(x) h_L(0, T_D(x))]}{dx} \\ &\qquad = \frac{dQ_D(x)}{dx}\left[h_{vap}\big(0, T_D(x)\big) + h_L\big(0, T_D(x)\big) + c_{p,V}(T_F(x) - T_D(x))\right] \end{aligned} \tag{Eq. 2.14}$$

Where $c_{p,V}$ represents the heat capacity of water vapor and the same boundary conditions (Eqs 2.7 – 2.10) from the general case of a thermally conductive membrane apply. By solving this system of governing equations for MD (Eqs. 2.11 – 2.14) numerically, the temperature and flow rate distributions along the module are revealed. This enables the identification of several operating regimes and mass recovery rates based on the flow conditions simulated. The nuanced differences between each operating regime can be most easily examined analytically (i.e., not numerically). An analytical expression can be obtained for the critical flow rate ratio which shows strong agreement to the numerical solution:

$$\alpha \geq \alpha_{FLR} = \alpha^* = \frac{(T_H - T_C^*)\left(\frac{\bar{h}_{v,F}}{c_D} + \frac{T_H + T_C^*}{2} - T_H^*\right)}{(T_H^* - T_C)\left(\frac{\bar{h}_{v,F}}{c_F} + \frac{c_D}{c_F}\frac{T_H + T_C^*}{2} - T_C^*\right)} \qquad \text{Eq. 2.15}$$

2.2.1. Flow Balancing Rule

It is convenient to use an equal flow rate for both the feed and distillate streams, in which case the flow rate ratio, α (i.e., the ratio of the distillate to the feed flow rate, Q_D/Q_F) is simply unity. However, recent studies have found that $\alpha = 1$ is generally not an optimal operating condition.[42,55] Because the feed salinity is typically very high in the context of MD, the specific heat capacity of the feed stream, c_F, is substantially lower than that of the distillate stream, c_D. If the same flow rate, Q, is used for both streams, the heat capacity flow (i.e., heat capacity per time) of the feed stream, as quantified by Qc_F, is substantially lower than that of the distillate stream as quantified by Qc_D. This unbalance in heat capacity flow between the two streams will lead to sub-optimal system performance in terms of membrane utilization and energy efficiency.[42,55,56]

The critical flow rate ratio, α^*, for a DCMD process with counter-current flows has been previously derived via thermodynamic analysis of a DCMD module.[55] This critical flow rate ratio represents the condition in which the operation is optimal. However, the expression for α^* is complicated and involves functions that have to be evaluated numerically. That is, the threshold temperature difference (Eqs. 2.5 and 2.7), or the T* components, are quantities that cannot be solved for directly. Therefore, assumptions would have to be made about the threshold temperature differences to carry out the thermodynamic analysis presented in this work. By simplifying the FRR to exclude T*, a more direct analysis is achieved without sacrificing accuracy. Following the principle of balancing heat capacity flow (i.e., $Q_F c_F = Q_D c_D$),[56] a simple approximation of α^* is the ratio between the specific heat capacities of feed stream, c_F, and that of the distillate stream, c_D (i.e., $\alpha^* = c_F/c_D$). Such a simple approximation of α^* can deviate from the exact α^* to a substantial extent (Figure 2.1A), primarily due to the changes of flow rates in the DCMD module as water recovery reduces the feed flow rate and increases the distillate flow rate.

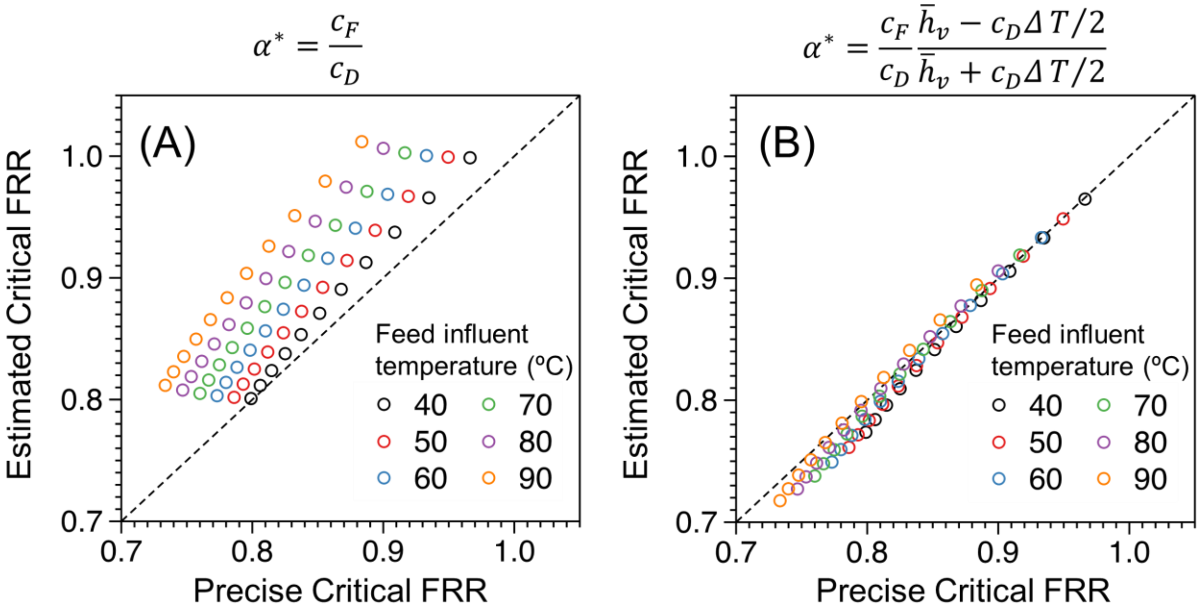

Figure 2.1 – Estimated critical flow rate ratio (FRR, α^*) vs. precise critical FRR as given by Eq. A1. The estimated α^* is calculated using the approximate equation given on the top of each panel. In each panel, six feed influent temperatures, T_H, are used in the simulation. In each series, the molality of the feed solution ranges from 0 to 5 mole kg^{-1} (of water). The distillate temperature is fixed at 20 ºC. The molality of the distillate is assumed to be zero. The FRR agreement is plotted from 0.7 to 1.05 because α^* was found to lie around 0.9 in related work.[55]

Here, we present an alternative approximation of α^* that does not involve any function requiring numerical evaluation. This is advantageous because the thermodynamic insights gained from the following analysis are more readily approached when applying analytical rather than numerical evaluation. This approximation is obtained based on equation 37 of Lin et. al[55] by removing or adjusting terms that are not intrinsic properties of the solution and cannot be directly determined. The alternative approximation is given as:

$$\alpha^* = \frac{c_F}{c_D}\frac{\bar{h}_{vap} - c_F \Delta T/2}{\bar{h}_{vap} + c_D \Delta T/2} = \frac{c_F}{c_D}\varphi(\bar{h}_{vap}, c_D, c_F, \Delta T) \qquad \text{Eq. 2.16}$$

where $\bar{h}_{vap}$ is the average enthalpy of vaporization of water and ΔT is the difference between the influent temperature of the saline feed stream (T_H) and that of the distillate stream (T_C). Because $\bar{h}_{vap}$ is slightly dependent on temperature, its value can be evaluated using the average temperature of T_H and T_C. We note that enthalpy of vaporization only has very weak dependence on salinity and we therefore use the h_v for pure water throughout our discussion in this paper. Eq. 2.16 is derived simply by ignoring the “threshold temperature difference” (Eqs. 2.5 and 2.7). This equation of α^* differs from $\alpha^* = c_F/c_D$ by a correction factor, $\varphi(\bar{h}_{vap}, c_D, c_F, \Delta T)$, that is always higher than unity. This correction factor roughly accounts for the change of the heat capacity flows of both the feed and distillate streams due to the decrease of the feed stream flow rate and increase of the distillate stream flow rate during the DCMD operation. This modified expression (Eq. 2.16), simple and without obscure functions, can provide an outstanding approximation of the exact α^* (Figure 2.1B).

2.2.2. Thermodynamic Limit of Single-Pass Water Recovery

Another important observation from module-scale thermodynamic analysis is the presence of the limit for a single-pass water recovery, R_{max} . The presence of this limit can be explained by a relatively simple principle. When there is sufficient membrane area to allow for the greatest extent of heat and vapor transport possible, there are two possible scenarios. In scenario (1) called distillate limiting regime (DLR, where $\alpha < \alpha^*$), the distillate water is limited as compared to the feed water. In this case, when a fraction of the feed water evaporates, the evaporation transfers sufficient amount of latent heat to warm up the distillate stream to an extent that the driving force for vapor transport (i.e., the partial vapor pressure difference) vanishes (Figure 2.2A). In scenario (2) called feed limiting regime (FLR) where $\alpha > \alpha^*$, when a sufficient fraction of the feed water evaporates, the evaporation carries away a large amount of latent heat and thereby cools down the feed stream to an extent that the driving force for vapor transport vanishes (Figure 2.2B). Here, membrane area is considered “sufficient” if the overall transport of vapor and heat through the membrane is maximized. This resistance to this transport is a function of the membrane’s porosity, thermal characteristics, area, and thickness. In both scenario 1 and scenario 2, this fraction represents the limit for single-pass water recovery as it is thermodynamically infeasible to recover a fraction of the feed water larger than this theoretical limit in a single-pass.

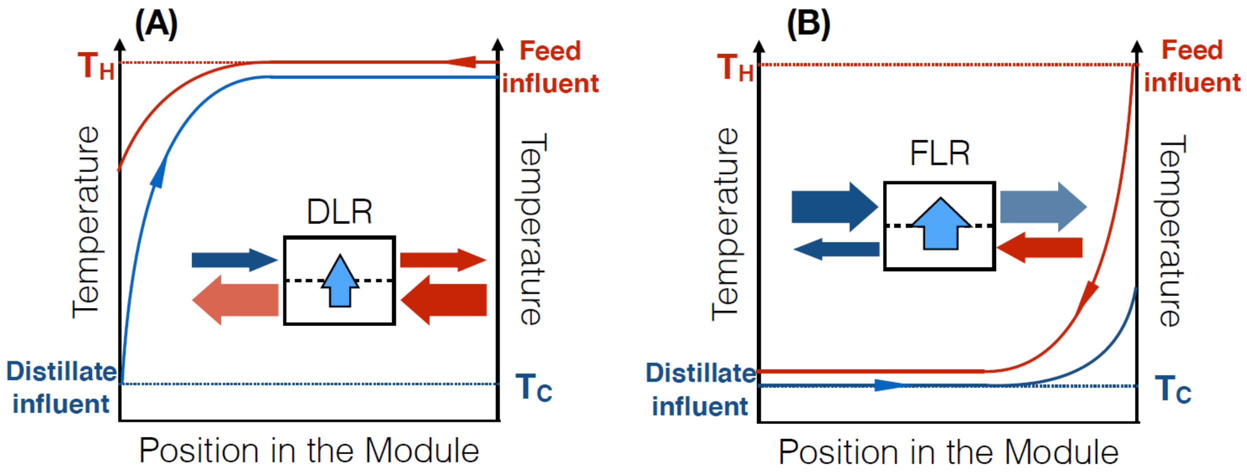

Figure 2.2 – Schematic illustrations of (A) distillate limiting regime (DLR) and (B) feed limiting regime (FLR) in a DCMD module. In DLR, the distillate flow rate is small compared to the feed flow rate, so that the distillate temperature rises up in the module to approach the feed influent temperature. In FLR, the feed flow rate is small compared to the distillate flow rate, so that the feed temperature drops in the module to approach the distillate influent temperature. In both cases, the difference in salinity of the two streams leads to a small temperature difference when the driving force (i.e., partial vapor pressure difference between the two streams) vanishes to zero.

Here we derive simple and intuitive approximations of the limits of the single-pass recovery in both the DLR and FLR, considering the impact of the conductive heat transfer as quantified by thermal efficiency, η_{th}. Briefly, η_{th} is the ratio of the amount of heat transferred via vapor transport over the total amount of heat transferred via both vapor transport and thermal conduction. In the DLR, the distillate temperature will increase by approximately ΔT, i.e., from T_C to T_H, if we neglect the threshold temperature difference. Therefore, the heat gained by the distillate stream is roughly $Q_D c_D \Delta T$, if we do not consider the minor change in the distillate flow rate. Only part of this heat gain, which is $\eta_{th} Q_D c_D \Delta T$, is from the latent heat of condensation. If the mass of the vapor transferred across the membrane is ΔQ, the latent heat of condensation is roughly $\Delta Q \bar{h}_{vap}$. When membrane area is sufficient, ΔQ reach its maximum ΔQ_{max}, which can be described using the following equation based on energy balance and the definition of flow rate ratio α (Q_D/Q_F).

$$\eta_{th}\alpha Q_F c_D \Delta T = \Delta Q_{max}\bar{h}_{vap} \qquad \text{Eq. 2.17}$$

Based on these relationships, we arrive in the approximate expression for the theoretical maximum recovery (assuming sufficient membrane area) for DLR:

$$R_{max}^{DLR} = \frac{\Delta Q_{max}}{Q_F} = \frac{\eta_{th}c_D}{\bar{h}_{vap}}\alpha\Delta T \qquad \text{Eq. 2.18}$$

Following a similar logic, the feed temperature will decrease by approximately ΔT, i.e., from T_H to T_C, when the system is in a FLR with sufficient membrane area and $\alpha > \alpha^*$. In this case, the heat loss in the feed stream is roughly $Q_F c_F \Delta T$, if we do not consider the minor change in the feed flow rate. Part of this heat loss, roughly $\eta_{th}Q_F c_F \Delta T$, provides the latent heat for evaporation which is approximately $\Delta Q\bar{h}_{vap}$. With sufficient membrane area, ΔQ reaches its maximum ΔQ_{max}, which leads to the following energy balance equation:

$$\eta_{th}Q_F c_F \Delta T = \Delta Q_{max}\bar{h}_{vap} \qquad \text{Eq. 2.19}$$

The approximate expression for the theoretical maximum recovery (assuming sufficient membrane area) in FLR is then given by:

$$R_{max}^{FLR} = \frac{\Delta Q_{max}}{Q_F} = \frac{\eta_{th}c_F}{\bar{h}_{vap}}\Delta T \qquad \text{Eq. 2.20}$$

Combining Eqs. 18, 19 and 20 suggest that R_{max}^{FLR} is always higher than R_{max}^{DLR}, which is reasonable because only in FLR does the distillate stream have enough heat capacity flow to ensure that the maximum evaporation of the feed stream can be achieved. Therefore, R_{max}^{FLR} is the ultimate limit for single-pass water recovery for counter-current flow DCMD.

Even though derived with a few simplifying assumptions, Eq. 2.20 provides a remarkable approximation of the maximum single-pass water recovery predicted from more detailed and accurate analysis reported in the previous work (Figure 2.3).[55] In an ideal scenario with perfect thermal efficiency, R_{max} simply becomes $c_F \Delta T/\bar{h}_{vap}$. For seawater, $c_F/\bar{h}_v$ is roughly 1/600 K^{-1}. Therefore, even with a temperature difference ΔT of 60 K, the theoretical maximum single-pass recovery is only 10%. With the finite membrane area and realistic thermal efficiency, η_{th}, the realistic single pass-recovery can be significantly lower. Readers with interest in the impacts of system size and thermal efficiency can refer to the recent work by Swaminathan et al[42].

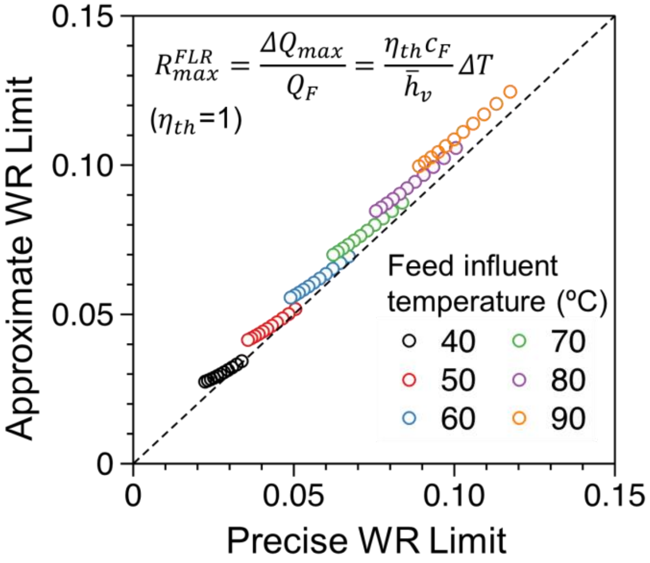

Figure 2.3 – Estimated maximum single pass water recovery (WR, R_{max}^{FLR}) versus the precise WR given by Eq. A6. The estimated R_{max}^{FLR} is calculated using the equation given in the top of the figure assuming ideal thermal efficiency ($\eta_{th} = 1$). Six feed influent temperatures, T_H, are used in the simulation. In each series, the molality of the feed solution ranges from 0 to 5 mole kg^{-1} (of water). The distillate temperature is fixed at 20 ºC. The molality of the distillate is assumed to be zero.

2.3. Energy Efficiency Analysis for MD Driven by a Conventional Heat Source

In this section we present a simple framework to analyze the energy efficiency of a DCMD system powered by conventional heat source with and without a heat exchanger (HX). A conventional heat source is defined as a heat source with a constant temperature. Its function is to increase the temperature of the feed stream to T_H by providing the required amount of power, w. In comparison, when a stream containing waste-heat is used as the heat source, the temperature of the heat source decreases as more heat is extracted. Whether the temperature of the heat source changes when it transfers thermal energy to the feed stream in MD is the primary difference between a conventional heat source and a stream with waste-heat as the heat source.

We have shown in Section 2.2.2. that only a small fraction of the feed water can be recovered in a single pass. Because feed water needs to be pretreated and is thus associated with certain cost, recycling of the feed stream effluent is likely practiced in most practical operation. When the feed stream is recycled, a stream of feed water with the same flow rate as the trans-membrane flow rate, ΔQ, should be supplemented to the feed loop to maintain steady-state of the flows (Figure 2.4A, Figure 2.5A). The same flow rate ΔQ is also extracted from the distillate loop. We note that even though steady-state for the flows can be achieved, the system still behaves transiently due to the accumulation of the salt in the feed loop. There are two different designs for a counter-current DCMD system with recycled feed and distillate streams. The primary difference is that an HX is not implemented in the first design (Figure 2.4A) but implemented for heat recovery in the second design (Figure 2.5A).

It is reasonable to assume that the temperature differences across the membrane in the DCMD module and across the HX are both spatially uniform along the module and HX, respectively, as long as the membrane area and the size of the HX are not impractically large and the flow rates are optimized based on the critical flow rate ratio. This assumption of constant temperature difference, which is reasonable based on pervious simulations, highly simplifies the following analysis. Here, we are not interested in developing or applying a predictive model to describe system performance. Instead, we aim to develop a simple framework for quantifying energy efficiency provided that we know the trans-membrane temperature difference in the MD system, ΔT_{MD}, the temperature difference in the HX, ΔT_{HX}, the working temperatures T_H and T_C, and finally, the thermal efficiency, η_{th}.

2.3.1. Specific Energy Consumption for a DCMD System without HX

If the trans-membrane temperature difference is ΔT_{MD} throughout the MD module, the effluent feed temperature is ΔT_{MD} higher than the influent temperature of the distillate and is thus $T_C + \Delta T_{MD}$. In the absence of HX, the effluent of the feed stream with a flow rate of $Q_F - \Delta Q$ is blended with the supplementing new feed stream with a flow rate of ΔQ (Figure 2.4A). This blending reduces the temperature of the feed effluent by a small degree. The temperature of the blended stream, T_{mix}, can be calculated based on energy balance:

$$T_{mix} = T_C + (1 - R)\Delta T_{MD} \qquad \text{Eq. 2.21}$$

where R is the single-pass water recovery which is usually negligibly small. To further simplify our analysis, we ignore R and treat T_{mix} as $T_C + \Delta T_{MD}$, which would lead to slight underestimation of the energy consumption but much simpler expressions.

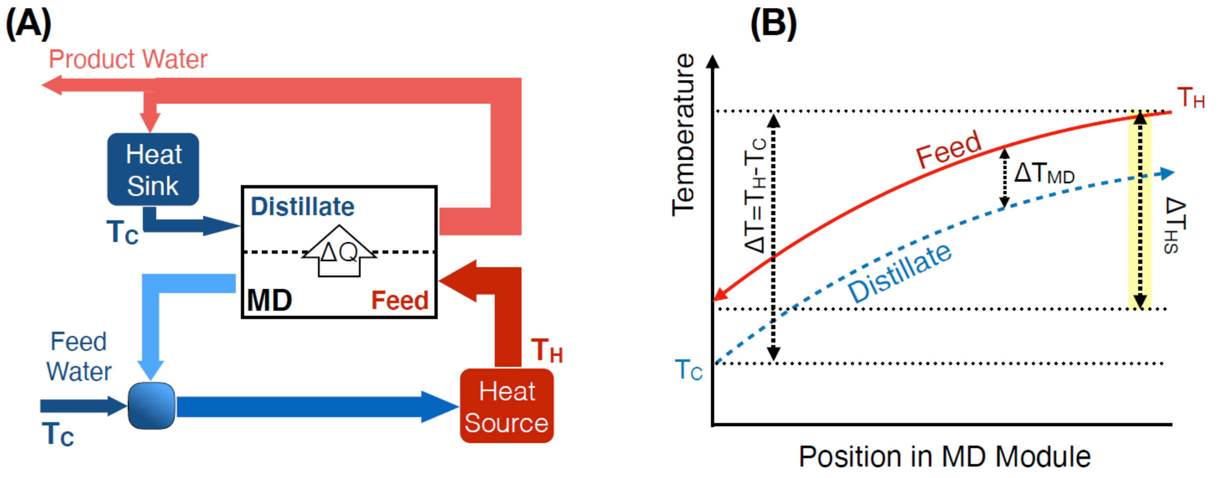

Figure 2.4 – (A) Countercurrent DCMD system with recycled feed and distillate streams in the absence of HX to recover latent heat from the distillate stream. A heat source is required to maintain the working temperature (T_H) and a heat sink is required to maintain the distillate inlet temperature (T_C). (B) Temperature profiles of the feed and distillate streams along the module in (A). The DCMD feed inlet temperature, initially at T_H, drops along the module due to evaporative cooling and conduction, reaching $T_C + \Delta T_{MD}$ at the feed outlet. The transmembrane vapor flux, ΔQ, is added to supplement the feed stream (at T_C) to maintain constant flow rate ratio, bringing the feed loop temperature down very slightly to T_{mix}. Before returning to the feed inlet, the feed passes a heat source where it undergoes the temperature change ΔT_{HS}, which is related to the power input into the system. The distillate inlet temperature, initially at T_C, increases along the module

due to vapor condensation and conduction, reaching $T_H - \Delta T_{MD}$ at the distillate outlet. The transmembrane vapor flux, ΔQ, is removed from the system to maintain constant flow rate ratio and the remaining distillate passes a heat sink where it reaches the operating temperature, T_C.

In the absence of an HX, the feed stream after blending needs to go through the heat source so that its temperature is raised to the working temperature T_H (Figure 2.4B). The temperature gain of the feed stream in the heat source, ΔT_{HS}, is given by:

$$\Delta T_{HS} = T_H - T_{mix} \approx T_H - T_C - \Delta T_{MD} = \mathit{\Delta} T - \Delta T_{MD} \qquad \text{Eq. 2.22}$$

Therefore, the thermal power of heat absorbed in the heat source, P_{th}, is simply:

$$P_{th} = c_F Q_F \Delta T_{HS} \qquad \text{Eq. 2.23}$$

After quantifying the power of heat input from the heat source, we also need to evaluate the product water flow rate which is essentially the transmembrane flow rate, ΔQ (Figure 2.4A). This can be performed using similar energy balance approach as shown in Section 2.2.2. Specifically, the temperature drop along the feed stream is $\mathit{\Delta} T - \Delta T_{MD}$ and the heat lost along the feed stream is roughly $c_F Q_F(\mathit{\Delta} T - \Delta T_{MD})$. The trans-membrane flow rate can therefore be expressed as:

$$\mathit{\Delta} Q = \frac{c_F Q_F (\mathit{\Delta} T - \Delta T_{MD}) \eta_{th}}{\bar{h}_{vap}} \qquad \text{Eq. 2.24}$$

The energy efficiency of the process can be quantified using the specific thermal energy consumption, SEC_{th}, defined as the energy consumed to generate a unit mass of distillate which is essentially the power required to generate a unit flow rate of distillate:

$$SEC_{th} = \frac{P_{th}}{\mathit{\Delta} Q} = \frac{\bar{h}_{vap}}{\eta_{th}} \qquad \text{Eq. 2.25}$$

Eq. 2.10 is rather intuitive as η_{th} quantifies the fraction of the heat transfer that is attributable to vapor transfer. According to Eq. 2.25, DCMD without HX can be even more energy intensive than just evaporating water due to the presence of conductive heat loss. While c_F appears in both Eqs. 2.23 and 2.24, it cancels out in Eq. 2.25, which has the following important implication. Although the salt concentration in the feed loop increases as more water is recovered from the feed solution, the build-up of salt concentration theoretically has little impact on SEC_{th} because (1) the significant impact of salt concentration on c_F applies equally to both w and ΔQ which offset each other, and (2) the impact of salt concentration on $\bar{h}_{vap}$ is very small. The independence of SEC_{th} on salt concentration allows us to apply Eq. 2.25 for analyzing the energy consumption of the system even if the system is transient due to the feed solution being concentrated.

2.3.2. Specific Energy Consumption for a DCMD System with HX

The SEC_{th} can be significantly reduced by coupling an HX with a DCMD system to recover the latent heat of condensation[43]. Specifically, the distillate stream in the DCMD module warms up by acquiring the heat transferred from the feed stream via both vapor transfer and conductive heat transfer. The heat that accumulates in the warm distillate effluent can be harvested to pre-heat the feed stream to a certain temperature to reduce the required power from the heat source to raise the influent feed stream temperature to T_H (Figure 2.5).

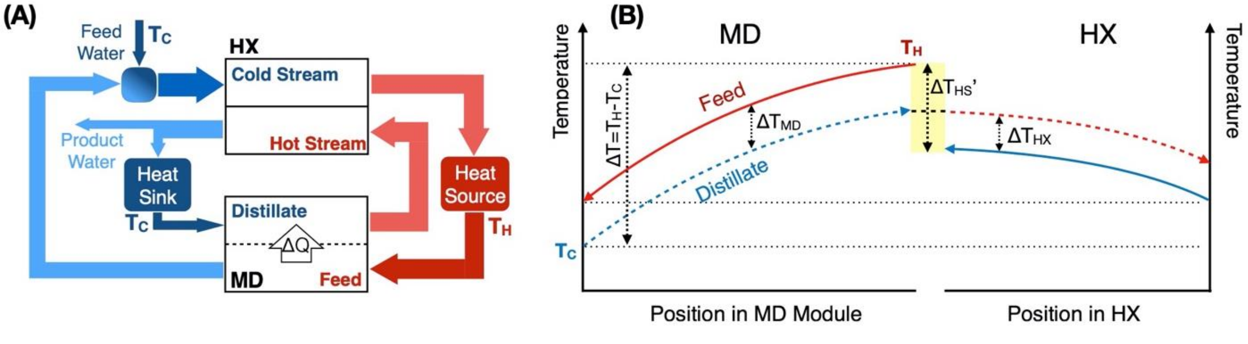

Figure 2.5 – (A) Countercurrent DCMD system with recycled feed and distillate streams and an HX to recover latent heat from the distillate stream. A heat source is required to maintain the working temperature (T_H) and a heat sink is required to maintain the distillate inlet temperature (T_C). (B) Temperature profiles of the feed and distillate streams along the DCMD module and HX in (A). The DCMD feed inlet temperature, initially at T_H, drops along the DCMD module due to

evaporative cooling and conduction, reaching $T_C + \Delta T_{MD}$ at the feed outlet. The transmembrane vapor flux, ΔQ, is added to supplement the feed stream (at T_C) to maintain constant flow rate ratio, bringing the feed temperature down very slightly to T_{mix}. Before returning to the feed inlet, the feed passes the HX, where it increases in temperature to $T_H - \Delta T_{MD} - \Delta T_{HX}$, then the heat source, where it increases in temperature by $\Delta T'_{HS}$ or back to the working temperature, T_H. Here $\Delta T_{HS}{}'$, which is related to the power input into the system, is reduced due to the presence of the HX. The distillate loop temperature, initially at T_C, increases along the module due to vapor condensation and conduction, reaching $T_H - \Delta T_{MD}$ at the distillate outlet. The distillate then passes the HX, decreasing in temperature as the latent heat is used to preheat the feed stream, then the transmembrane vapor flux, ΔQ, is removed from the system to maintain constant flow rate ratio. Finally, the remaining distillate passes a heat sink where it reaches the operating temperature, T_C, and enters back into the DCMD module.

If we again apply the assumption of negligible temperature change due to the blending of the supplementing feed water into the feed loop, then the temperature-rise of the feed stream flowing through the heat source is given by the follow equation according to the temperature profiles in Figure 2.5B:

$$\Delta T'_{HS} = \Delta T_{MD} + \Delta T_{HX} \qquad \text{Eq. 2.26}$$

where ΔT_{HX} is the temperature difference between the hot and cold streams in the HX. In this case, the specific energy consumption, SEC', can be quantified as:

$$SEC'_{th} = \frac{P_{th}}{\Delta Q} = \frac{c_F Q_F \Delta T_{HS}{}'}{c_F Q_F (\mathit{\Delta} T - \Delta T_{MD}) \eta_{th} / \bar{h}_{vap}} = \frac{\bar{h}_v}{\eta_{th}} \frac{\Delta T_{MD} + \Delta T_{HX}}{\mathit{\Delta} T - \Delta T_{MD}} \qquad \text{Eq. 2.27}$$

Here, the term $(\Delta T_{MD} + \Delta T_{HX})/(\Delta T - \Delta T_{MD})$ accounts for impact of the latent heat recovery. Eq. 2.12 suggests that SEC'_{th} can be reduced by reducing ΔT_{MD} and/or ΔT_{HX}. A smaller ΔT_{MD} indicates more heat from the influent feed stream (into the DCMD module) is transferred and stored in the effluent of the distillate stream, while a smaller ΔT_{HX} indicates a larger fraction of the heat stored in the distillate stream is recovered to heat up the feed stream in the HX. However, we note that, with the same feed and distillate stream flow rates, the achievement of smaller ΔT_{MD} and ΔT_{HX} requires larger MD membrane area and HX area, respectively, which consequently leads to lower vapor flux in the DCMD module and lower heat flux in the HX. This is a classic tradeoff between "kinetics and energy efficiency",[44,45] which is manifested in this case as a positive correlation between vapor/heat fluxes and SEC'.[35]

Lastly, we note that the implementation of HX does not guarantee energy saving. Mathematically, this can be shown by the critical condition where SEC_{th} in Eq. 2.25 equals SEC'_{th} in Eq. 2.27:

$$\Delta T = 2\Delta T_{MD} + \Delta T_{HX} \qquad \text{Eq. 2.28}$$

With this critical condition, the same specific energy is consumed regardless of whether the HX is implemented or not. This critical condition corresponds to the scenario where the effluent temperature of the feed stream in the DCMD module, $T_C + \Delta T_{MD}$, is the same as the effluent temperature of the feed stream in the HX, $T_H - \Delta T_{MD} - \Delta T_{HX}$, so that heating up either stream using the external heat source requires the same amount of power. If the effluent temperature of the feed stream in the DCMD module is even higher than that in the HX, i.e., $\Delta T < 2\Delta T_{MD} + \Delta T_{HX}$, it would become more energy efficient to simply eliminate the HX and operate the system as in Figure 2.4A, because the feed stream effluent in the DCMD module would not be able to receive any heat from a stream with even lower temperature. An extreme case of such a condition would be $\Delta T < 2\Delta T_{MD}$, which suggests that the effluent of the feed stream is even warmer than the effluent of the distillate stream in the DCMD module and thus no latent heat can possibly be recovered. This usually occurs when there is insufficient membrane area to recover enough feed water, which leads to poor single-pass water recovery (as compared to the thermodynamic limit) but relatively high vapor flux due to the conservation of driving force (i.e., transmembrane temperature difference). The very extreme case for such a scenario is when a small membrane coupon is used instead of membrane module: due to the insufficient residence time of the feed and distillate streams, very little water is recovered and the temperatures of the feed and distillate streams also experience negligible change.

2.3.3 Gained Output Ratio

In thermal desalination processes, the gained output ratio, or GOR, is often used as a metric to quantify the energy efficiency. GOR is defined as the mass of distillate produced per mass of vapor generated, which in effect quantifies the “number of times” latent heat of condensation is reused. Therefore, GOR is mathematically the ratio between the latent heat and the specific energy consumption. Its non-dimensionality and the use of latent heat as reference make it an informative alternative to specific energy consumption for quantifying the energy efficiency of an MD process. For DCMD without HX, GOR is simply η_{th}. When HX is employed, GOR can be described as:

$$GOR \approx \eta_{th} \frac{\mathit{\Delta} T - \Delta T_{MD}}{\Delta T_{MD} + \Delta T_{HX}} \qquad \text{Eq. 2.29}$$

Eq. 2.29 clearly suggests that GOR depends on four parameters, η_{th}, $\mathit{\Delta} T$, ΔT_{MD} and ΔT_{HX}. If we assume that $\Delta T_{MD} = \Delta T_{HX}$, which is practically unnecessary but would nonetheless simplify our analysis, we can illustrate the results from Eq. 2.29 using Figure 2.6. GOR can be improved by (1) improving η_{th}, (2) reducing ΔT_{MD} and ΔT_{HX}, and (3) using a larger $\mathit{\Delta} T$ which is equivalent to using a higher influent feed temperature T_H if we assume T_C to be fixed. With a $\mathit{\Delta} T$ of 60 ºC (e.g., $T_H =$ 80ºC and T_C = 20 ºC), a ΔT_{MD} and a ΔT_{HX} of 5 ºC (practical minima), and a thermal efficiency, η_{th}, of 80% (in the high practical range), the corresponding GOR according to Eq. 2.29 is 4.4. Based on such an analysis, it is practically challenging to push the GOR beyond five. If a GOR of 5 can indeed be achieved, the ΔT_{MD} and ΔT_{HX} must be so small that vapor flux for the MD process and heat flux in the HX are both impractically low.

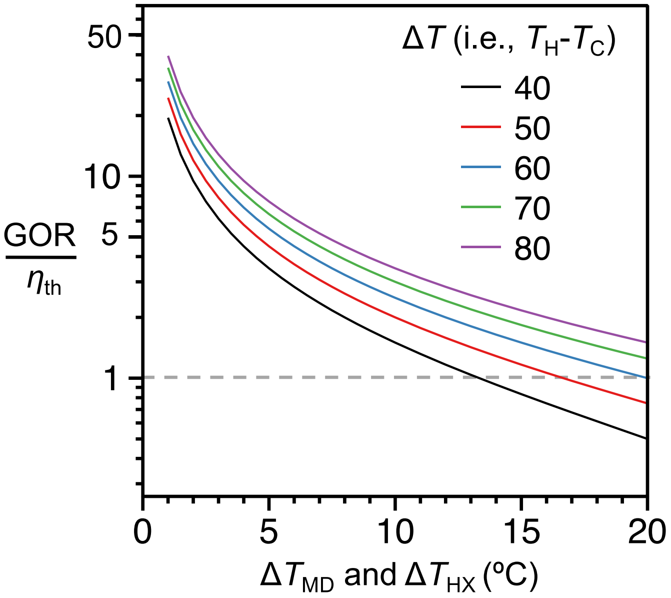

Figure 2.6 – Gained output ratio (GOR) over thermal efficiency (η_{th}) plotted as a function of transmembrane temperature difference (ΔT_{MD}) and the temperature difference between the hot and cold streams along the HX (ΔT_{HX}) according to Eq. 2.29. ΔT_{MD} and ΔT_{HX} were assumed to be constant for ease of analysis. A series of six ΔT values, or the difference between the DCMD feed inlet (T_H) and the distillate inlet (T_C), relevant to MD were included in the analysis. A dashed line is shown at $\frac{GOR}{\eta_{th}} = 1$ to represent the lowest logically acceptable energy consumption for water production.

2.4. Energy Efficiency Analysis for MD Powered by Waste Heat Streams

While waste heat may exist in different forms, one major source of waste heat is hot streams from power generation and industrial processes. The major difference of hot streams from a conceptual constant temperature heat source as defined earlier is the change of stream temperature as a hot stream gives away heat. The schematics of DCMD system powered by an external hot stream as the heat source and the corresponding temperature profiles in different components are presented in Figure 2.7 and Figure 2.8 for two system designs, one with HX and the other without. The heat source is essentially an additional HX exchanging heat between the feed stream and waste heat stream. We refer to this additional HX as HX_2 in the following discussion. A DCMD system always requires an HX_2 for extracting heat from the waste heat stream, whereas HX_1 is for recovering the latent heat stored in the warm distillate effluent and is thus optional.

For DCMD without an HX for recovering the accumulated heat in the distillate, the cool effluent of the feed channel in the MD module blends with the supplementary feed stream and then enters the HX_2 to absorb heat from the waste-heat stream (ws) (Figure 2.7A). The temperature of WS decreases from the influent (i) temperature, $T_{ws,i}$, to the effluent (e) temperature $T_{ws,e}$ due to the release of heat to the feed stream (Figure 2.7B). To describe the behavior of HX_2, we denote the temperature difference of the two exchanging streams at the exit of the waste-heat stream (i.e., the entrance of the cold stream in HX_2) as ΔT_{HX2}. We note that (1) this temperature difference is dependent on the flow rates of the two stream and the available area for heat transfer in the HX; and (2) unlike in the DCMD module or HX_1 where the flows of heat capacity for the two streams are similar when operation is optimized, there is no required relationship between the flow rates of the two streams in HX_2. Therefore, ΔT_{HX2} is only defined at the exit of the waste-heat stream and does not necessarily apply to other position in HX_2. The effluent temperature of waste-heat stream, after surrendering the power of w, is:

$$T_{ws,e} = T_H - \Delta T_{HS} + \Delta T_{HX2} = T_C + \Delta T_{MD} + \Delta T_{HX2} \qquad \text{Eq. 2.30}$$

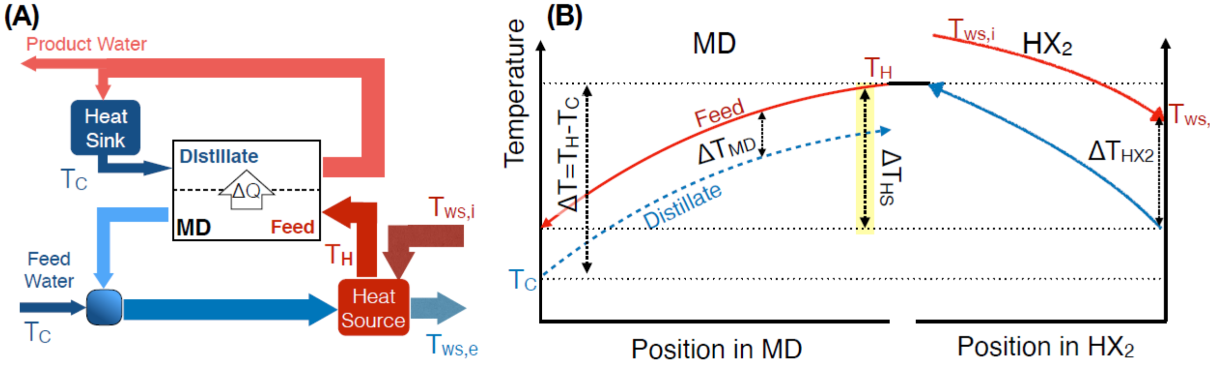

Figure 2.7 – (A) Countercurrent DCMD system with recycled feed and distillate streams and an HX (HX_2) to recover heat from a waste-heat stream (ws) as the heat source. The heat source is required to maintain the working temperature (T_H) and a heat sink is required to maintain the distillate inlet temperature (T_C). (B) Temperature profiles of the feed and distillate streams along the DCMD module and HX_2 in (A). The DCMD feed inlet temperature, initially at T_H, drops along the DCMD module due to evaporative cooling and conduction, reaching $T_C + \Delta T_{MD}$ at the feed outlet. The transmembrane vapor flux, ΔQ, is added to supplement the feed stream (at T_C) to maintain constant flow rate ratio, bringing the feed temperature down very slightly to T_{mix}. Before returning to the feed inlet, the feed passes HX_2 where it increases in temperature by ΔT_{HS} back to the working temperature. Here ΔT_{HX2} is the temperature difference at the outlet of both streams in

HX_2. The temperature difference along HX_2 is not important to this analysis as we are only concerned with the total power delivered from the heat source. The waste-heat stream decreases in temperature from the inlet ($T_{ws,i}$) to the effluent ($T_{ws,e}$) as heat transfers into the feed stream, bringing it back to the working temperature. The distillate loop temperature, initially at T_C, increases along the module due to vapor condensation and conduction, reaching $T_H - \Delta T_{MD}$ at the distillate outlet. The transmembrane vapor flux, ΔQ, is removed from the system distillate to maintain constant flow rate ratio. The remaining distillate passes a heat sink where it reaches the operating temperature, T_C, and enters back into the DCMD module.

When a waste-heat stream is used as the heat source for the DMCD system equipped with an HX for heat recovery, the system is designed following the schematic shown in Figure 2.8A. Accordingly, the temperature profiles in the MD module and in HX (for heat recovery) and HX_2 (as the heat source) are shown in Figure 2.8B. In this case, the effluent temperature of waste-heat stream, after surrendering the power of w, is:

$$T'_{ws,e} = T_H - \Delta T'_{HS} + \Delta T_{HX2} = T_H - \Delta T_{MD} - \Delta T_{HX} + \Delta T_{HX2} \qquad \text{Eq. 2.31}$$

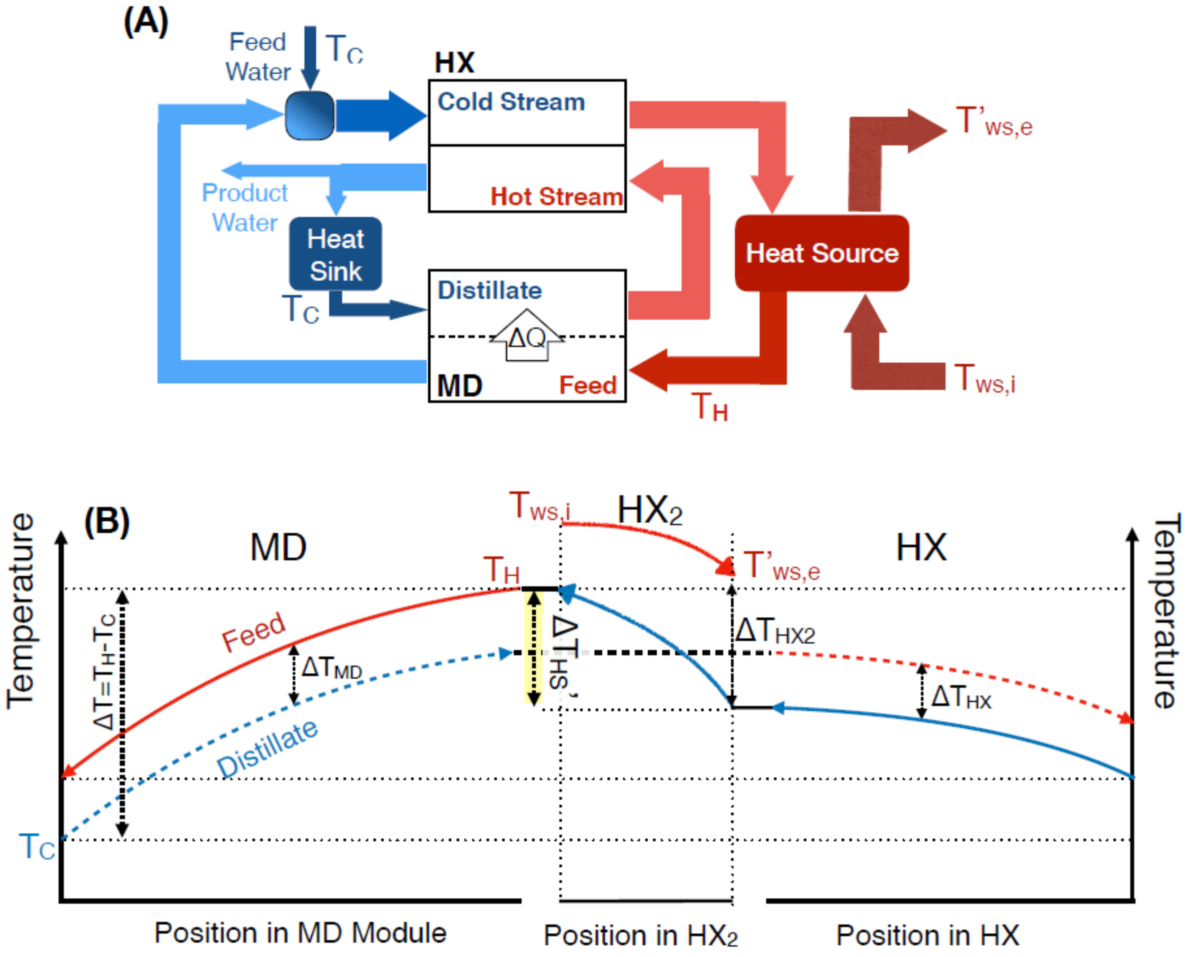

Figure 2.8 – (A) Countercurrent DCMD system with recycled feed and distillate streams and HX1 to recover heat from the distillate stream and HX2 to harness heat from a waste-heat stream (ws) as a heat source. The heat source is required to maintain the working temperature (T_H) and a heat sink is required to maintain the distillate inlet temperature (T_C). (B) Temperature profiles of the feed and distillate streams along the DCMD module, HX1, and HX2 in (A). The DCMD feed inlet temperature, initially at T_H, drops along the MD module due to evaporative cooling and conduction, reaching $T_C + \Delta T_{MD}$ at the feed outlet. The transmembrane vapor flux, ΔQ, is added to supplement the feed stream (at T_C) to maintain constant flow rate ratio, bringing the feed temperature down very slightly to T_{mix}. The feed then passes HX1, where it increases in temperature to $\Delta T_H - \Delta T_{HS}$. Here ΔT_{HS} is the heat that must be supplied by the heat source, HX2. The feed then passes HX2 where it is brought back to the working temperature. Here ΔT_{HX2} is the temperature difference at the outlet of both streams in HX2. The temperature difference along HX2 is not important to this analysis as we are only concerned with the total power delivered from the heat source. The waste-heat stream decreases in temperature from the inlet ($T_{ws,i}$) to the effluent ($T'_{ws,e}$) as heat transfers into the feed stream, bringing it back to the working temperature. The distillate loop temperature, initially at T_C, increases along the module due to vapor condensation

and conduction, reaching $T_H - \Delta T_{MD}$ at the distillate outlet. The distillate then passes HX1 where it decreases in temperature to $T_C + \Delta T_{MD} + \Delta T_{HX}$. The transmembrane vapor flux, ΔQ, is removed from the system distillate to maintain constant flow rate ratio and the remaining distillate passes a heat sink to bring it to the operating temperature, T_C, where it re-enters the DCMD module.

2.4.1. Gained Output Ratio when a Waste Heat Stream is used as the Heat Source

While the system schematics and the temperature distribution profiles appear to be more complicated when a waste-heat stream replaces a constant-temperature heat source, the way to calculate SEC_{th} and GOR, are no different from those as described in Section 2.3. This is because, the analysis in Section 3 only assumes that a certain power is extracted from the heat source but does not specify the working mechanism of the heat source. Therefore, whether the heat source is a constant-temperature heat source or a waste-heat stream does not affect the calculation and results of the SEC_{th} and GOR. Based on these metrics of energy efficiency, installing an HX for recovering the heat accumulated in the distillate effluent stream, as depicted in Figure 2.7A, is of paramount importance even if a waste-heat stream is used as the heat source. However, comparing Figure 2.7B and Figure 2.8B suggests that, because of the different power extracted from the waste-heat stream, the effluent temperatures of the waste-heat streams also differ depending on whether heat recovery from distillate stream is implemented. A lower effluent temperature of the waste-heat stream suggests that a larger fraction of the available waste-heat is utilized. This is another piece of important information that is not reflected by conventional metrics for energy efficiency, such as SEC_{th} and GOR.

2.4.2. Specific Yield and Waste Heat Utilization Efficiency

When waste-heat streams are used as the heat source, we propose an alternative metric to describe “energy efficiency”, namely the specific yield (SY). SY is defined as the ratio between the trans-membrane vapor flow rate and the power of the “available heat,” $P_{th,ws,max}$, which can be quantified as:

$$P_{th,ws,max} = c_{ws} Q_{ws} (T_{ws,i} - T_C) \qquad \text{Eq. 2.32}$$

where c_{ws} and Q_{ws} are the specific heat capacity and the flow rate of the waste-heat stream. The difference between $T_{ws,i}$ and T_C determines w_{max} because the waste-heat stream theoretically would not be able to provide any more heat to the feed stream once its temperature approaches T_C (i.e., there will not be any driving force). Because c_{ws} and Q_{ws} are independent of any property in the MD system, for any given waste-heat stream we can treat $P_{th,ws,max}$ as a constant that is independent of the design (e.g., whether to include heat recovery or not) and operation of the MD system. Based on the definition of SY and Eq. 2.24:

$$SY = \frac{\Delta Q}{P_{th,ws,max}} = \frac{c_F Q_F (\Delta T - \Delta T_{MD}) \eta_{th}}{\bar{h}_{vap} P_{th,ws,max}} \qquad \text{Eq. 2.33}$$

Eq. 2.33 suggests that SY is roughly fixed as long as feed stream properties (e.g. c_F and Q_F) and operating conditions (e.g. ΔT and ΔT_{MD}) are maintained constant. In other words, for a given waste-heat stream with a certain power, how much water can be generated in a unit time is only dependent on how the DCMD process is operated but not on whether latent heat recovery is implemented.

To further elucidate this point, we define waste-heat utilization efficiency, η_{ws}, as the ratio between the power of the heat absorbed by the MD system for water production, w, and the power of the available heat, $P_{th,ws,max}$. We note that η_{ws} is essentially the *effectiveness* of HX$_2$, defined as the ratio between the actual heat transfer rate and the maximum possible heat transfer rate[21]. According to such a definition, η_{ws}, can be expressed as:

$$\eta_{ws} = \frac{P_{th}}{P_{th,ws,max}} = \frac{T_{ws,i} - T_{ws,e} (or\ T'_{ws,e})}{T_{ws,i} - T_C} \qquad \text{Eq. 2.34}$$

Here, $T_{ws,e}$ as in Eq. 2.34 is used when latent heat recovery is not implemented, whereas $T'_{ws,e}$ is used when an HX is integrated to recover the latent heat accumulated in the distillate effluent stream. Given the same waste-heat stream (i.e., the same c_{ws}, Q_{ws}, and $T_{ws,i}$), $T'_{ws,e}$ is always higher than $T_{ws,e}$, and η_{ws} is thus lower when latent heat recovery is implemented. The relationship between η_{ws}, SEC_{th}, and SY can be more clearly illustrated using the following expression derived by combining Eq. 2.33 and the definition of SEC:

$$SY = \frac{\eta_{ws}}{SEC_{th}} \qquad \text{Eq. 2.35}$$

We note that Eq. 2.34 and Eq. 2.35 are valid if we consider a liquid waste heat stream (e.g., a stream of hot water) that would not undergo phase change, which will be the focus of this analysis for its simplicity. However, if a low pressure/temperature steam is used as the waste heat stream, then the apparent heat due to the temperature change of the stream in both vapor and liquid phase and latent heat due to phase change must be all considered.

Because we have shown that SY is independent of the presence or the degree of latent heat recovery, Eq. 2.35 simply suggests that the ratio between η_{ws} and SEC_{th} is constant. The constant η_{ws}/SEC can be interpreted as following: when latent heat recovery is implemented, the MD process as a whole is more energy efficient with a lower SEC_{th} (except when $\Delta T < 2\Delta T_{MD} + \Delta T_{HX}$), but at the same time, a smaller fraction of the available waste-heat is utilized to drive the MD process (i.e., η_{ws} is smaller); in contrast, when latent recovery is not implemented, the MD process is less energy efficient as indicated by a higher SEC_{th}, but a larger fraction of the available waste-heat is utilized. It therefore does not matter whether latent heat recovery is implemented, or to what extent is implemented, if the performance metric chosen to assess the system is SY.

2.4.3. Improving Specific Yield with Multiple Stages

Following the above discussion, substantial enhancement of SY must involve improving η_{ws} and SEC_{th} simultaneously. This can be achieved by implementing multi-stage DCMD with each stage integrating an HX for heat recovery (Figure 2.9). Here, each stage is essentially an independent DCMD system absorbing heat from the waste-heat stream at a certain temperature range. We note that the definition of a multi-stage system here is different from the multi-stage or multi-effect vacuum MD or air-gap MD where the multiple stages or effects are implemented to maximize latent heat recovery. The multiple stages in Figure 2.9 are implemented to maximize the utilization of the thermal energy in the waste-heat stream. In the case when n stages are implemented, the specific yield, SY is given by the following expression:

$$SY = \sum_{k=1}^{n} \frac{\eta_{ws,k}}{SEC_{th,k}} \qquad \text{Eq. 2.36}$$

where $\eta_{ws,k}$ and $SEC_{th,k}$ are the waste-heat utilization efficiency (defined by Eq. 2.34) and the specific energy consumption (defined by Eq. 2.27) for the k stage, respectively.

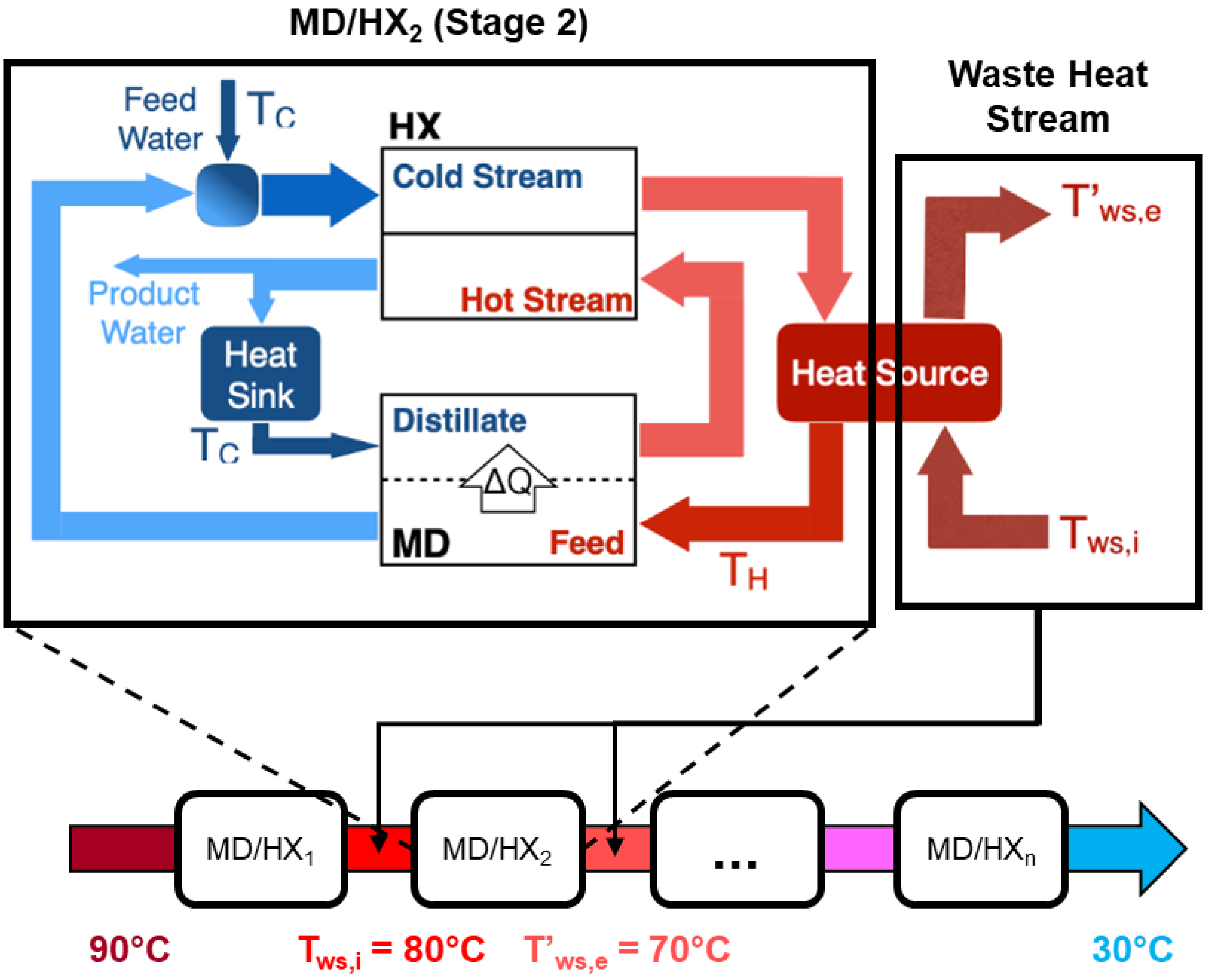

Figure 2.9 – Multiple stages of DCMD module integrated with an HX to recover latent heat from its distillate stream. The heat implemented into the system to maintain the working temperature is transferred via heat exchanger (HX_2) from a waste-heat stream. Including multiple MD/HX stages

increases the waste-heat usage efficiency. Each individual stage consists of the system analyzed in Figure 2.8.

Implementing more stages will certainly enhance the overall specific yield, but it requires substantially more capital investment. Due to the dependence of SEC_{th} on ΔT, the SEC_{th} of later stages is higher if ΔT_{MD} and ΔT_{HX} are maintained the same (Eq. 2.27), i.e., the MD/HX systems are less efficient in later stages. We also expect the vapor flux to be substantially lower in later stages as the partial vapor pressure difference corresponding to the same ΔT_{MD} is significantly smaller when the average of the feed and the distillate stream temperatures is lower[45,46]. Both the considerations of SEC and vapor flux suggest a diminishing return for installing additional stages in the lower temperature range. Therefore, whether or not multiple stages should be implemented and how many stages should be implemented are strongly dependent on the relative economic value of the product water as compared to the capital cost.

2.5. Conclusion and Implications

In this study we first highlight the importance of balancing heat capacity flows between the feed and distillate streams in MD for optimal performance. We discuss the presence of two operating regimes, the distillate limiting regime (DLR) and the feed limiting regime (FLR), as demarcated by α^*, the critical flow rate ratio. The novelty of this work is the development of an approximation for the critical flow rate ratio that eases the understanding of module-scale MD energy analysis and optimization. We also define an approximation for the maximum single pass water recovery, R_{max}, for the two regimes based on a simple energy balance over the vapor. While some of these concepts have been derived in previous study, here we re-derive them using more intuitive and comprehensible principles and showed the approximation is both simple and accurate when compared to a precise numerical solution derived in previous work.

We also provide a framework for evaluating the energy efficiency of MD in two configurations, with and without an integrated heat exchanger (HX) to recover latent heat from the distillate stream. Our analysis reveals the presence of a critical condition to determine if the implementation of HX results to energy saving. Because MD is attractive for its ability to use low grade waste heat, for the first time we present a framework for analyzing energy efficiency of MD powered by waste heat stream. We define a new metric, specific yield, which quantifies the performance of MD powered by waste heat stream. For a single-stage MD powered by a waste heat stream, whether implementing latent heat recovery or not only affects the SEC_{th} (or GOR) of the process, but not the specific yield. In other words, although implementing latent heat recovery for a single-stage MD deriving heat from a waste heat stream appears to improve the efficiency in the conventional metrics such as SEC_{th} and GOR, it does not actually better utilize the available waste heat for desalination. Multi-stage MD with latent heat recovery can more efficiently harness the available waste heat, but its economics may be questionable and require further investigation.

The approximations derived in this work are not only satisfactorily accurate, but can be calculated from easily measurable quantities. The presented framework for energy efficiency analysis in MD does not involve computationally heavier heat and mass transfer simulations, consequently, this framework will be useful for high-level techno-economic evaluation and module-scale optimization, which is strongly relevant for practical application of MD in industry.

CHAPTER 3

3. Distinct Behaviors between Gypsum and Silica Scaling in Membrane Distillation

A version of this work was published in Environmental Science and Technology in 2019. Permission for reproduction in this dissertation was granted.

https://doi.org/10.1021/acs.est.9b06023

3.1. Introduction

Membrane distillation (MD) is an emerging water separation process suitable for the treatment of hypersaline wastewater.[13,17,60–62] In MD, a vapor pressure gradient generated between a heated feed solution and a cool distillate drives the transport of water vapor across a microporous hydrophobic membrane.[63] MD possesses several advantages compared to other desalination technologies such as reverse osmosis (RO) and mechanical vapor compression (MVC).[22] MD tolerates high salinity wastewater that cannot be desalinated by RO and requires lower temperature and capital costs than MVC.[14,17,22] Also, MD is capable of leveraging low-grade waste heat,[16,64] with its modularity rendering it adaptable to the dynamic wastewater treatment demand in industrial applications. These desirable features make MD a promising technological candidate for treating hypersaline wastewater from different industrial sectors.

Despite its desirable features for hypersaline wastewater management, MD has yet to be adopted widely in practice in part due to its vulnerability to membrane-related process failure. Like all other membrane processes, including those that have been extensively employed in practice (e.g., RO and nanofiltration), MD is subject to membrane fouling that results in flux decline. A unique challenge to MD is the wetting of membrane pores when the feed water contains a considerable level of amphiphilic molecules or low-surface-tension, water miscible contaminants. Fortunately, these problems can be satisfactorily addressed either by extensive pretreatment of the feed water[65–68] and/or by using novel membranes with special wettability.[17,69–75] What remains to be an important challenge is membrane scaling, which is particularly problematic if MD is to be used in its most promising application of recovering water from hypersaline wastewater.

As a long-standing challenge facing MD, membrane scaling involves the development of inorganic salt deposits on membrane surfaces.[67,76,77] During membrane scaling, scalants block membrane pores to cause a reduction in water vapor flux, thereby compromising the process efficiency and economic feasibility of MD. Mineral scaling can lead to pore wetting and the consequent contamination of the distillate.[78–80] Compared to organic fouling and pore wetting in MD, a comparable knowledge of inorganic scaling is still emerging,[76] and the mechanisms of membrane scaling in the MD process have not been fully understood.[81–83] For example, membrane wetting induced by mineral scaling is a mysterious phenomenon. While a previous study has shown that nucleation and subsequent growth of minerals on the membrane surface precede membrane wetting in vacuum MD experiments with synthetic seawater as the feed solution, the mechanism governing scaling-induced wetting was not clearly elucidated.[84] Unlike low-surface-energy or amphiphilic contaminants (e.g., surfactants), which result in membrane wetting by lowering the surface tension of feedwater,[85,86] it is still unclear how hydrophobic membranes fail as a barrier to salt transport in MD as a result of mineral scale formation.

Furthermore, due to the complex chemical composition of feedwaters, different types of scaling might occur in an MD process. Gypsum and silica are among the most commonly found scaling in membrane-based desalination. Both types of scaling have been reported in MD as responsible for the dramatic decline of water vapor flux.[87–89] It should be noted that gypsum and silica scaling have distinct formation mechanisms at the molecular level. Gypsum crystals are created via a crystallization process involving the hydrated reaction between Ca^{2+} and SO_4^{2-}. In contrast, the formation of silica scale, which is typically amorphous, pertains to the polymerization process of silicic acid. This fundamental difference might result in varied scaling behaviors in membrane desalination, and a comparative understanding of those behaviors will provide valuable insights to further elucidate the mechanisms of membrane scaling. To the best of our knowledge, however, such a comparison has not been performed in the literature.

In this study, we performed comparative direct-contact membrane distillation (DCMD) experiments with commercial polyvinylidene fluoride (PVDF) membranes using feed solutions that contain the precursors for gypsum and silica formation. The different behaviors of scaling by gypsum and silica were investigated by comparing the water vapor flux, feed salinity, distillate salinity, and transmembrane impedance obtained during DCMD experiments with these two types of scalants. We also characterized the PVDF membranes after the scaling experiments to further elucidate the different mechanisms of scaling. These characterizations included scanning electron microscopy (SEM) to analyze the surface and cross-section morphology of the membranes, energy-dispersive X-ray spectroscopy (EDS) to map the elemental distribution, and tensile testing to understand the impact of scaling on the mechanical strength of the membranes.

3.2. Materials and Methods

3.2.1. Chemicals and Membranes

Calcium chloride ($CaCl_2$) and sodium sulfate (Na_2SO_4) were purchased from Research Products International (Mount Prospect, IL). Sodium bicarbonate ($NaHCO_3$), sodium chloride (NaCl), and hydrochloric acid (HCl) were acquired from Fisher (Hampton, NH). Sodium metasilicate (Na_2SiO_3) was purchased from Alfa Aesar (Haverhill, MA). All salts and chemicals were used as received without further purification. PVDF membranes with a nominal pore diameter of 0.45 μm were purchased from GE Healthcare (Chicago, IL).

3.2.2. Experimental Setup for Membrane Distillation

We used a custom-built DCMD system to perform MD experiments in this study (Figure 3.1). The feed and distillate streams were circulated by centrifugal pumps through the DCMD cell. The temperatures of the feed and distillate streams were controlled using thermostatic water baths and were monitored using in-line temperature probes. Throughout the experiments, we measured the mass and electrical conductivity of the distillate, from which we can calculate the real-time flux and salt rejection. We also performed two additional measurements that are not typical in existing DCMD studies. The first measurement was the transmembrane impedance, which was introduced by our previous study to elucidate the surfactant-induced dynamic wetting phenomenon in MD.[85,90] Specifically, two 4 cm^2 titanium electrodes, one on each side of the membrane, were connected to a potentiostat (Bio-Logic, France). The time-dependent impedance between the two electrodes was measured during the MD experiments. The second additional measurement was feed conductivity, which was monitored by an in-line conductivity probe (eDAQ, Australia). The feed conductivity measurement provides critical information about the saturation level of the feed solution.

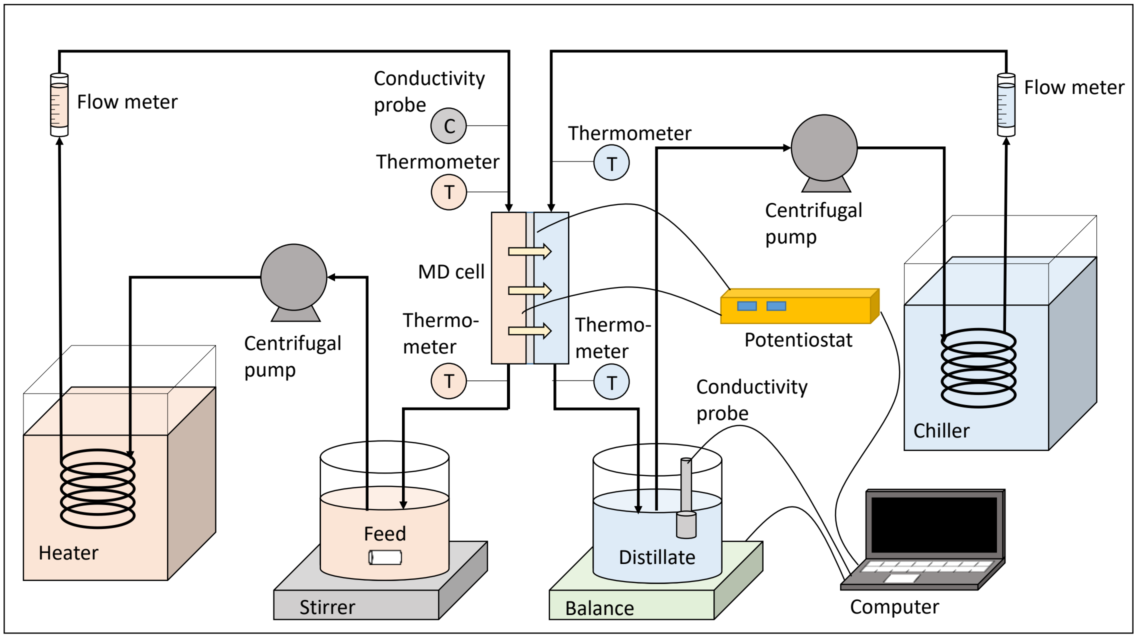

Figure 3.1 - Schematic of the MD setup used to perform transmembrane impedance measurements. The feed solution is pumped centrifugally through a heating bath as the flow rate, conductivity, and temperature of the solution are monitored throughout the experiment. The distillate solution is similarly pumped centrifugally through a cooling bath as the flow rate, conductivity, and temperature of the solution are monitored throughout the experiment. In the distillate solution vessel, a conductivity probe records the real time salinity of the solution in order to provide evidence of membrane failure, or wetting, throughout the experiment. A balance records the real time mass of the distillate solution in order to provide data with which to calculate water vapor flux through the membrane. A potentiostat is connected to the membrane testing module to apply alternating current at regular intervals to measure the impedance across the MD membrane at varying frequencies.

3.2.3. Scaling Experiments: Solution Chemistry and Detection Methods

We performed scaling experiments in DCMD using feed solutions of either gypsum or silica. The feed solutions were prepared using solution compositions similar to those used in the literature, which satisfied the criteria of having an initial concentration high enough to offer a reasonable induction time for silica scaling (less than 36 hr for an initial water flux of 25 L m^{-2} hr^{-1}).[87,91–93] Specifically, gypsum solutions were prepared by mixing $CaCl_2$ and Na_2SO_4 in deionized water to achieve an initial molar concentration of 24.5 mM for both Ca^{2+} and SO_4^{2-} ions, which corresponds to a bulk gypsum saturation index (SI) of 0.16. Silica solutions were prepared by combining 5 mM Na_2SiO_3, 50 mM NaCl, and 1 mM $NaHCO_3$, then adjusting the pH of the solution to 6.5 using an HCl solution (1 M) to achieve the same SI of 0.16 for amorphous silica. In both cases, the SI was calculated as the logarithm of the quotient of the ion activity products at the supersaturated state (K) and the saturation state (K_0), respectively:

$$SI = log\left(\frac{K}{K_0}\right) \qquad \text{Eq. 3.1}$$

PHREEQC, a program developed by the United States Geological Survey to perform aqueous geochemical calculations,[94] was used to calculate the saturation index of the relevant species within the solutions.

In all scaling experiments, the feed and distillate solution temperatures were maintained at 60 °C and 20 °C, respectively, whereas the flow rates of the feed and distillate streams were controlled as 0.45 L min^{-1} and 0.3 L min^{-1}, respectively. The feed flow rate was controlled to be higher than the distillate flow rate to enable a slightly higher hydraulic pressure on the feed side of the membrane, which allows for the facile detection of pore wetting.[70,71] The transmembrane impedance was measured using a sinusoidal perturbation with an amplitude of 5 mV and a frequency of 100 kHz. Each reported impedance data point represents the average of five measurements. Scaling was identified in each experiment by monitoring the water vapor flux over time. The formation of a mineral scale layer blocks the membrane pores, reduces the interfacial area for evaporation, and thus leads to vapor flux decline. We examined the possible occurrence of pore wetting via monitoring the distillate conductivity and the transmembrane impedance over time. As membrane pores become wetted, the penetration of the salty feed solution will result in a measurable increase of the distillate conductivity. Additionally, the progressive migration of the water-air interface (i.e., the thinning of the airgap in membrane pores) in the dynamic wetting process also results in the change of the transmembrane impedance.

3.2.4. Characterization of Scaled Membranes

To acquire more information regarding how scalants interact with the membranes and how such interactions result in performance failure, we performed detailed characterizations of the membrane samples after the scaling experiments. Both top-view and cross-section micrographs of the scaled membranes were captured using SEM (Zeiss, Germany). Besides, we also performed an elemental analysis of the scaled membranes using EDS. In addition, tensile testing was performed using a mechanical strength testing instrument (Instron, MA) on membrane coupons with a dimension of 5 × 25 mm to evaluate the impact of scaling on the mechanical strength, which was used to explain the mechanism of pore wetting induced by membrane scaling. Membrane coupons were dried in ambient conditions and gently handled during sample preparation and tensile testing in which no flaking or peeling of either scalant was observed. At least five replicates of membrane coupons were tested for each sample.

3.3. Results and Discussion

3.3.1. Distinct Behaviors between Gypsum and Silica Scaling in MD

The decline of vapor flux over time, as a result of pore blockage by mineral scale on the membrane surface, is a telltale indication of scaling in MD. The scaling induction time is defined as the point at which flux begins to decline. Comparing gypsum and silica feed solutions of equivalent SI (SI=0.16) under identical feed temperature and initial water vapor flux, the induction time for silica scaling was substantially longer than that for gypsum scaling (Figure 3.A vs. Figure B, red curves). The flux started to decline immediately after the gypsum scaling experiment started (Figure 3.A), whereas that caused by silica scaling did not occur until ~20 hours (Figure 3.2B). We also performed additional experiments with gypsum scaling at a lower SI (SI = 0.05) and observed the stable vapor flux for an extended period of time (Figure B), which suggests that gypsum scaling does not have to occur immediately after the experiment starts if the SI is not sufficiently high, and that a reduced initial SI results in a longer induction time. However, we chose to use an SI of 0.16 throughout this study as otherwise the silica scaling experiments would become impractically long.

Further, continuous measurement of the feed conductivity (a surrogate of salinity) revealed that the feed salinity barely changed in the course of gypsum scaling (Figure 3.2A). This is because the water flux (and therefore the rate of concentration of the feed solution) was quite low as a result of the short scaling induction time. The feed conductivity decreased slightly at the beginning of the gypsum scaling experiment and then increased very slowly as the MD process continuously removed water from the feed solution via evaporation and thus increased the concentration of NaCl (Figure B2).

On the contrary, the feed conductivity continued to increase throughout the silica scaling experiment (Figure 3.2B). In this case, additional 50 mM of NaCl was added with 5 mM Na_2SiO_3 to render the initial feed conductivity comparable to that of gypsum scaling. As a result, the increase of feed salinity was mostly attributable to the long scaling induction time leading to a notable increase of the concentration of the highly soluble NaCl. Starting with a feed conductivity of ~10 mS cm^{-1}, no flux decline was observed until the feed conductivity reached ~20 mS cm^{-1}, which implies that a dramatic increase of resistance against water vapor transport did not occur until total water recovery reached ~50%.

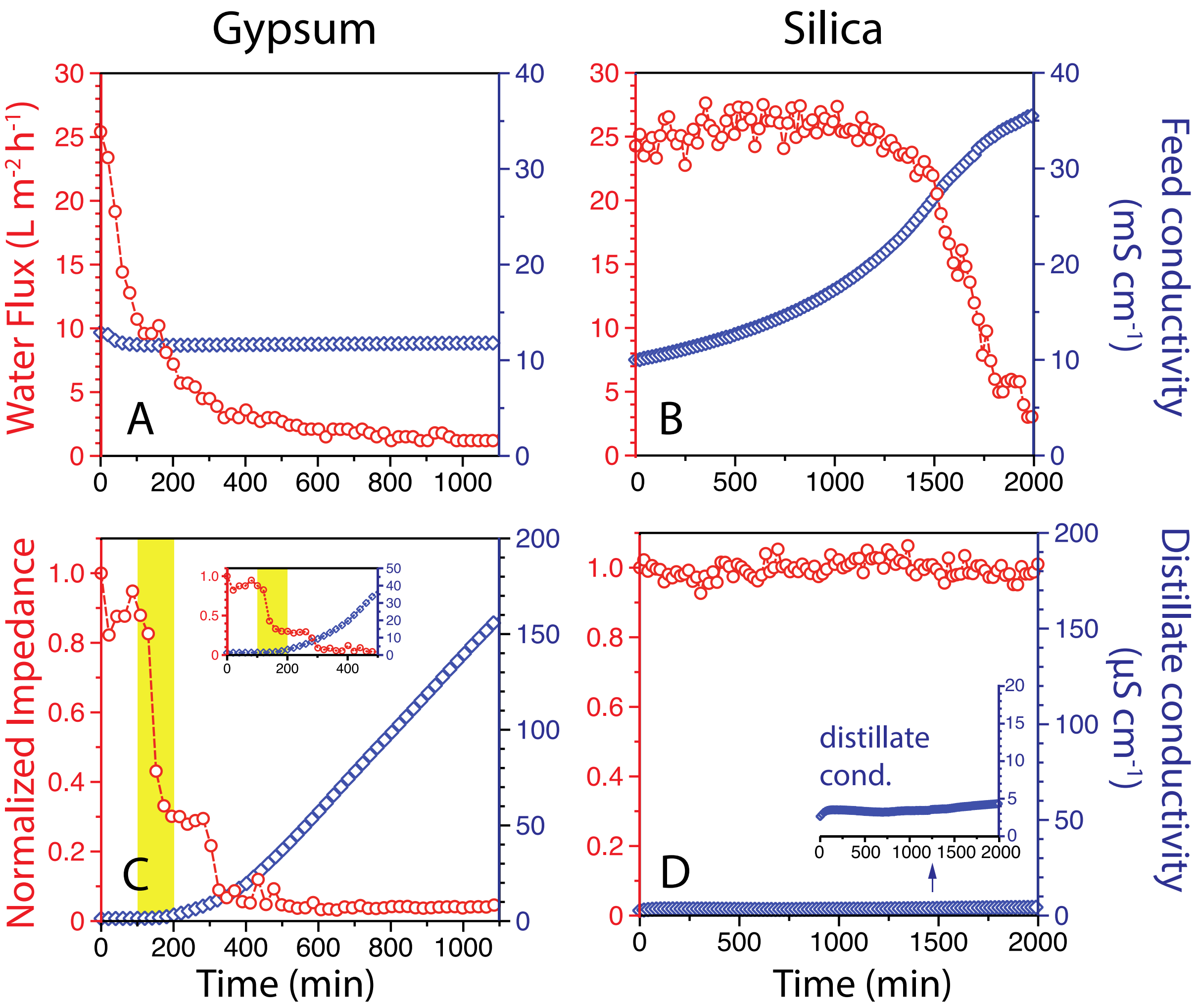

Figure 3.2 - (A and B) Water vapor flux (red) and feed conductivity (blue) in MD experiments with (A) gypsum scaling and (B) silica scaling. (C and D) Normalized transmembrane impedance at 100 kHz (red) and distillate conductivity (blue) in MD experiments with (C) gypsum scaling and (D) silica scaling. The initial pH of the feed solution was 6.5 in both cases. The gypsum feed solution had an initial gypsum SI of 0.16. The silica feed solution had an initial silica SI of 0.16. Figure 3.2A is also replotted as Figure B2 to more clearly show the small change of feed conductivity.

Besides the different scaling kinetics, another notable difference in the behavior of gypsum and silica scaling was whether pore wetting resulted from membrane scaling. Specifically, our experimental results suggest that pore wetting resulted from gypsum scaling but not from silica scaling (Figure 3.2). An obvious indication of pore wetting is the increase of distillate conductivity caused by the permeation of salt through the wetted pores. In experiments of gypsum scaling, the distillate conductivity started to increase in about three hours from the beginning of the experiment. The pore wetting induced by gypsum scaling continued to worsen as more water was recovered, with the real-time rejection decreasing from 98.7% at 200 min to 63.8% at 800 min. Similar differences between gypsum and silica scaling (i.e., earlier water flux decline and unique membrane wetting of gypsum scaling) were also observed in independent experiments using another commercial PVDF membrane (HVHP Durapore, Millipore Sigma) as shown in Figure B3 (Appendix B).

The single-frequency (100 kHz) impendence across the membrane was also monitored during the scaling experiments. In our previous studies of pore wetting induced by surfactants, the single-frequency impedance was found to be capable of monitoring imminent wetting before any salts enter the distillate stream.[85,90] Briefly, the progression of the feedwater-air interface within the pores toward the distillate changes the capacitance of the system and thereby results in a shift of impedance. Although the mechanism of wetting induced by surfactants and by mineral scale may be fundamentally different, similar behavior of impedance was observed in our experiments with gypsum scaling. Specifically, the impedance dropped dramatically before significant increase in distillate conductivity was observed (Figure 3.2C), which suggests that the feed-air interface within the membrane pores propagated toward the distillate progressively, in the time-scale of tens of minutes (see highlighted range in Figure 3.2C) and before any membrane pore was fully penetrated by the feed solution. In contrast to gypsum scaling, silica scaling did not result in any observable pore wetting, even though the DCMD experiment of silica scaling was performed for a much longer time than that of gypsum scaling. Both the distillate conductivity and the single-frequency impedance remained constant throughout the MD experiment (Figure 3.4D).

3.3.2. Microscopic Characterization of Scaled Membranes

The PVDF membranes after gypsum scaling and silica scaling demonstrated distinct surface morphologies (Figure 3.3). Compared to the pristine PVDF membrane (Figure B4, Appendix B), the surface of the PVDF membrane after gypsum scaling was covered by a layer of needle-like gypsum crystals with a magnitude of 100 µm (Figure 3.3A). While these distinct crystal particles physically overlapped each other, they did not form a single, chemically connected network. In contrast, the surface of the PVDF membrane after silica scaling showed an amorphous feature, with the sizes of silica particles much smaller than those of gypsum crystals (Figure 3.3B). Unlike the growth of gypsum, which follows a crystallization mechanism, the growth of silica follows a gelation mechanism that tends to form a continuous film which consists of submicron-sized, chemically bound silica particles (Figure 3.3B inset).

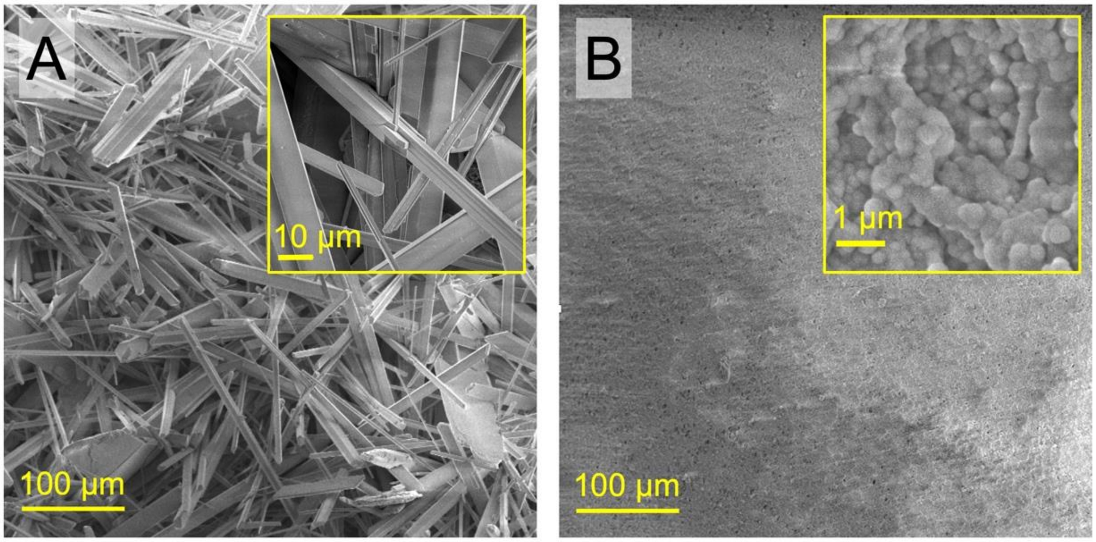

Figure 3.3 - Top-down scanning electron microscope (SEM) images of a polyvinylidene fluoride (PVDF) membrane scaled with (A) gypsum and (B) silica.

The occurrence of pore wetting induced by gypsum scaling was corroborated by the cross-section micrographs of SEM, which reveals the intrusion of gypsum crystals into the pores of the scaled PVDF membrane (Figure 3.4A to Figure 3.4E). More importantly, flaky gypsum crystals (indicated by the green arrows) were present deep within the PVDF membrane substrate (Figure 3.4C). The formation of gypsum both on the surface and within the pores of PVDF membrane was confirmed by the presence of Ca and S elements detected in the EDS analysis (Figure 3.4B, Figure 3.4D, and Figure 3.4E). On the other hand, no intrusion of silica into the pores of the scaled PVDF membrane was observed. Both the SEM micrograph (Figure 3.4F) and the corresponding EDS mapping of Si element (Figure 3.4G) suggest that the silica scale was only formed on the top surface of the PVDF membrane without intruding into the membrane pores. Also, the silica scale layer was much thinner than the gypsum scale layer, which was congruent with the slower kinetics of flux reduction due to silica scaling observed in Figure 3.2.

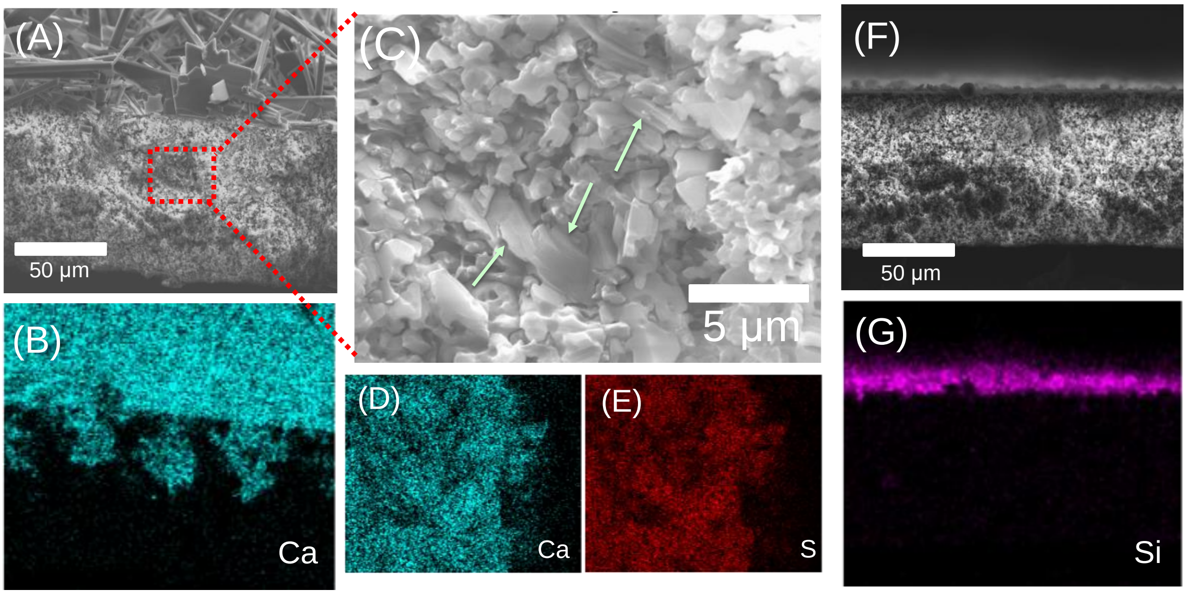

Figure 3.4 - SEM cross-section micrographs (A, C, and F) and the corresponding EDS mapping (B, D, E, and G) for PVDF membrane after gypsum scaling (A to E) and silica scaling (F and G). Panel C is a magnified view of the highlighted region in panel A, with its EDS mapping presented in panels D and E. The green arrows in panel C indicate flaky gypsum crystals observed deep within the membrane substrate.

3.3.3. Mechanisms of the Difference between Gypsum and Silica Scaling in MD

The dramatic difference in the behaviors between gypsum and silica scaling was attributable to their distinct scaling mechanisms. The different scaling kinetics (Figure 3.2) was likely a result of slower rate of silicic acid polymerization than that of gypsum crystallization, as evidenced by the generally much smaller sizes of silica scale observed in other desalination processes (e.g., RO and forward osmosis)[91–93,95–97] as well as our microscopic analysis (Figure 3.3 and Figure 3.4). As reported by Mbogoro *et al.*[98], the growth rate of a single gypsum crystal was ~0.05 μm min^{-1} for the most reactive [001] facet, using initial Ca^{2+} and SO_4^{2-} concentrations lower than that used in our experiments. Thus, gypsum crystals formed with a high kinetic rate were able to block the membrane pores (nominal diameter of 0.45 μm) quickly and reduce water vapor flux promptly. In contrast, the kinetics of silicic acid polymerization is much slower. Gilron *et al.*[99]

demonstrated that nanoscale silica particles could be observed after >10 hours of DCMD scaling experiment, with the SI of silica comparable to that of this study. Similarly, silica particles with sizes of 200-500 nm were observed after 2,000 min of silica scaling in the current study, forming a scaling layer that was much thinner than that by gypsum scaling (Figure 3.3 and Figure 3.4). The slow kinetics of silica scaling delayed the onset of water flux decline relative to that with gypsum scaling.

The even more intriguing phenomenon is the distinct wetting behaviors between gypsum and silica scaling in MD. The results of both distillate conductivity and transmembrane impedance indicate that pore wetting was induced by gypsum scaling but not by silica scaling. Although pore wetting induced by low-surface-tension or amphiphilic contaminants (e.g., surfactants) has attracted considerable attention and has been investigated extensively in the literature,[85,86,100] whether membrane wetting would occur concomitantly with mineral scaling remains uncertain. Also, the mechanism of scaling-induced wetting (when it indeed occurs) is ambiguous. It has been demonstrated that surfactants promote membrane wetting by reducing the surface tension of the feed solutions.[85,86] In such cases, pore wetting occurs when the liquid entry pressure (LEP) becomes lower than the hydraulic pressure difference, ΔP. In the case of scaling, however, the heightened feed salinity (as more water is recovered) increases the surface tension of feed solution and the corresponding LEP if all other factors are assumed to be unchanged.[101] Therefore, other mechanism(s) must exist for wetting that is induced by mineral scaling.

At the wetting frontier within the membrane pores, there are several possible interfaces for the addition of new crystal mass by precipitating out solutes from the feed solution. These interfaces include the water-membrane interface, the water-air interface, and the water-crystal interface. Thermodynamics of crystallization suggest that an interface with a lower interfacial energy also has a lower Gibbs free energy of crystallization and is thus more favorable for crystal growth.[102,103] Thus, crystal growth at the water-air interface, which possesses the highest interfacial energy, is as unfavorable as homogeneous precipitation,[104] while the growth of a crystal that has already formed is the most favorable. Consequently, gypsum crystals near the wetting frontier can grow bigger in the confined space within the membrane pores (Figure 3.5A). A similar but more-widely studied phenomenon is crystal growth in porous media, such as stone and concrete. Previous studies in this field have found that crystal growth in microscopic confined space can impose a substantial "crystallization pressure" against the confining "walls",[105–108] causing cracking and damage to buildings and geotechnical structures. The crystallization pressure, ΔP, can be quantified as[109]:

$$\Delta P = \frac{\upsilon RT}{V_m} SI \qquad \text{Eq. 3.2}$$

where υ is the van't Hoff factor of the solute ($\upsilon < 1$ for a saturated gypsum solution at 60 °C), R is the ideal gas constant, T is the absolute temperature, and V_m is the molar volume of the solid crystal (~73.8 $\text{cm}^3\ \text{mol}^{-1}$ for gypsum). For gypsum, $\upsilon RT/V_m$ is as high as ~75.0 J cm^{-3} at 60 °C, which suggests that gypsum can theoretically exert an enormous pressure (up to 6 MPa at SI=0.16) against the membrane pores even at a relatively low level of supersaturation.

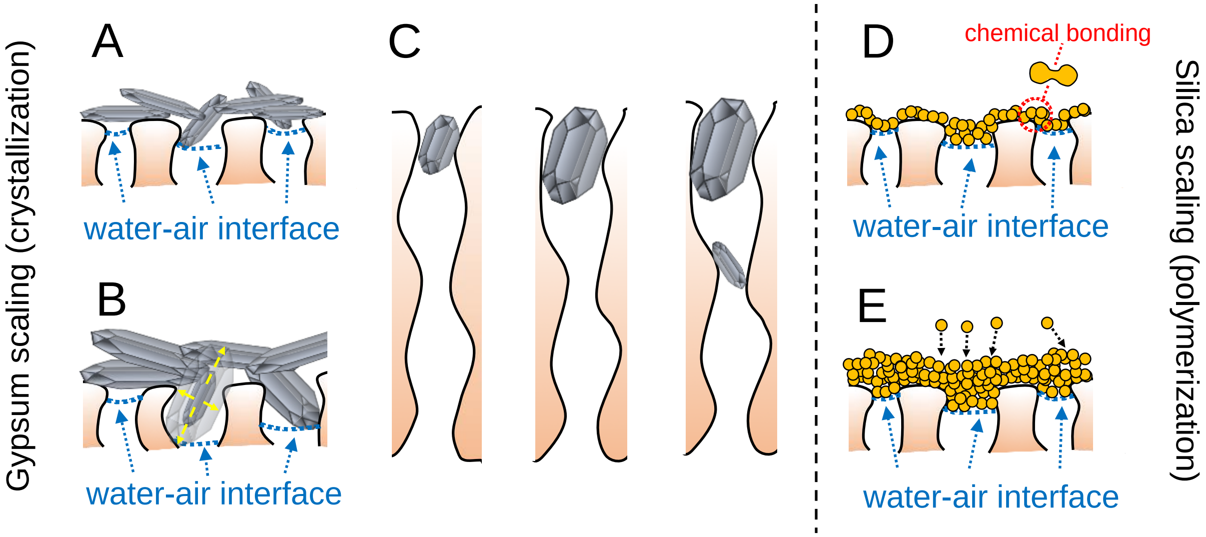

Figure 3.5 - Schematic illustration of (A) the initial formation of gypsum crystal particles near the wetting frontier before any wetting occurs; (B) Pore deformation caused by local growth of gypsum crystals that exert a large crystallization pressure; (C) Mechanism of wetting frontier propagation: the deformation of pores near the entrance results in reduced LEP and movement of the wetting frontier. The crystal growth at the new wetting frontier will again lead to local pore deformation and further movement of the wetting frontier; (D) Formation of a silica "mat" that covers the membrane pores; (E) Thickening of the silica "mat" by deposition of more silica particles and the further polymerization of silicic acid onto the formed silica "mat."

The water-crystal interface possesses the lowest interfacial energy due to the hydrophilic nature of gypsum crystals. Therefore, the water-crystal interface is most preferable for precipitating out additional solutes from the solution. Among all crystal particles that have already formed in the system, those near the wetting frontier are particularly prone to further growth because the local SI is the highest due to concentration polarization driven by evaporative flux (Figure 3.5A). Therefore, it is expected that the fastest crystal growth occurs to the crystals located near the wetting frontier, which locally deforms the membrane pores (Figure 3.5B). The local deformation of membrane pores results in an increase of membrane pore size and reduction of LEP (Figure 3.5C). If the local LEP is lower than the hydraulic pressure, wetting occurs and the water-air interface propagates toward the distillate until it reaches a small aperture with a corresponding local LEP that again exceeds the hydraulic pressure.

The exact mechanism for the new water-air interface to continue its propagation toward the distillate needs further elucidation. It is possible that smaller crystals begin to grow in the region near the new wetting frontier (Figure 3.4C and Figure 3.5C), and the crystallization pressure eventually leads to sufficient expansion of the aperture at the current wetting frontier so that the wetting frontier can move to the next position with a smaller aperture. This process of local deformation by crystallization pressure repeats itself, which eventually leads to percolation of the feedwater across the membrane (i.e., wetting). This theoretical postulation of the mechanism for crystallization-induced pore wetting suggests that such a wetting process is progressive, which is consistent with results observed in Figure 3.C. Specifically, the time difference between the onset of impedance drop and the onset of distillate conductivity increase was in the order of tens of minutes for wetting induced by gypsum scaling.

However, this mechanism of pore deformation due to crystallization pressure as described above does not apply to silica scaling which does not involve crystal growth. The formation of the silica scale layer follows two major steps. The first step is the polymerization of silicic acid to form silica particles,[110] and the second step is gelation in which silica particles aggregate to form a cake layer on the membrane surface (Figure 3.3B and Figure 3.5D).[111,112] Together, these two steps lead to the formation of a silica "mat" in which the primary particles are chemically bonded with each other. Different from gypsum crystals, silica particles are amorphous and lack of orientation preference for growth. The scaling precursors (i.e., silicate) in the feed solution grows the scale layer either by forming more silica particles that later deposit onto the existing scale layer, or by further polymerizing on the existing scale layer to make it thicker (Figure 3.5E). However, due to the lack of orientation preference for polymerization growth, the silica scale layer stays as a film on the membrane surface rather than forcefully intruding into the membrane pores (Figure 3.4F and Figure 3.4G). Therefore, the scaling by silica did not induce pore wetting in MD.

If this hypothesis of pore deformation by gypsum crystallization is correct, we should expect the mechanical properties of the PVDF membrane to be significantly affected by gypsum scaling. Therefore, we performed tensile testing of three PVDF membrane samples, including the reference membrane after an MD experiment using deionized (DI) water (without any scalant), the membrane after an MD experiment with silica scaling, and the membrane after an MD experiment with gypsum scaling. The experimental conditions of the MD experiments with scaling were identical to those for Figure 3.2. The representative stress-strain curves for these different samples are presented in Figure 3.6A.

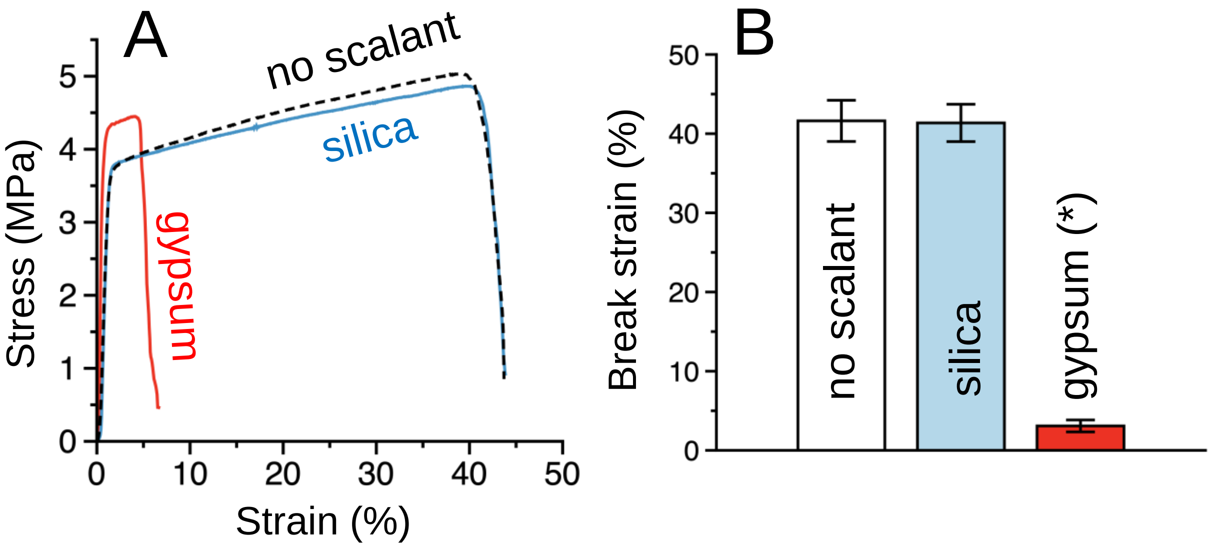

Figure 3.6 - Stress-strain curves for three different membrane samples, including the PVDF membrane after an MD experiment with deionized water (dash black), as well as the PVDF membranes subject to silica scaling (blue) and gypsum scaling (red). (B) Summary of the break point strain for the three membrane samples. Error bars represent standard deviations from five measurements. The asterisk (*) indicate that the break strain of a gypsum-scaled membrane was statistically different from a membrane subjected to an MD experiment without scalant (p < 10-5).

Comparing the representative stress-strain curves for the three membrane samples suggest that gypsum scaling significantly reduces the break point strain (i.e., the percent of membrane elongation upon fracture) as compared to the reference membrane subject to an MD experiment with DI water. In contrast, silica scaling does not seem to have any observable impact on the tensile properties of the PVDF membrane (Figure 3.6A). Statistical analysis (with five replicates for each sample) also confirms the break point strains for the reference membrane and membrane subject to silica scaling are similar and are both significantly higher than the membrane subject to gypsum scaling (Figure 3.6B). The decrease in break strain was likely associated with the increased pore sizes within membrane substrate due to pore deformation. Similarly, a decrease of break point strain caused by the increased depth and width of the voids within the polymer matrix has been observed in other studies.[113–115] Interestingly, scaling of either kind does not seem to reduce the break point stress (i.e., the stress upon fracture, Figure 3.6A and Table B1), which suggests that the most salient effect of gypsum scaling was to make the membrane more brittle. Overall, gypsum scaling reduced the toughness the membrane, which is proportional to the area under the stress-strain curve, i.e., the integral of stress with respect to strain (Table B1).

3.4. Implications

We have demonstrated contrasting behaviors between gypsum scaling and silica scaling in MD desalination. Gypsum scaling caused much earlier decline of water flux and induced membrane wetting that was not observed in silica scaling. Although it is known that these two scalants are produced from different mechanisms, i.e., crystallization and polymerization for gypsum scaling and silica scaling, respectively, our comparative experiments reveal, for the first time, that this mechanistic difference can translate to dramatically different impacts on membrane performance. In inland brackish water desalination where the saturation index of gypsum is typically higher than, or comparable to, that of silica,[7] gypsum scaling is more prone to initiate the water vapor flux decline while the detrimental effect of silica scaling on water productivity is not expected to occur until the feed solution is concentrated to a much greater extent. Even worse, gypsum scaling also has an additional detrimental effect of scaling-induced pore wetting. These considerations imply that cost-effective measures for scaling control, whether via pretreatment to remove scaling precursors, adding anti-scalant chemicals, or developing scaling-resistant membranes, should probably be prioritized toward mitigating scalants which are formed through crystallization.

CHAPTER 4

4. Decoupling the Effects of Feed Temperature and Water Flux on Gypsum Scaling in Membrane Distillation

4.1. Introduction

Water treatment technologies for high-efficiency desalination play an important role in the enhancement of freshwater resources without burdening our limited supply of energy. Membrane distillation (MD) carries the potential to supplement the production of water sustainably by utilizing low-grade waste heat to desalinate seawater, brackish water, and industrial wastewater.[17] In MD desalination, sparingly soluble mineral salts in the feed solution can rise above their saturation limits, especially when high recovery of pure water from the feed solution is attempted.[77] As a consequence, mineral scaling can occur due to nucleation directly onto the membrane surface and the accompanying crystal growth.[76] Theoretically, mineral scaling may also occur via deposition of crystals that form in the bulk solution of the MD feed channel (i.e. homogeneous nucleation), but, studies have shown that homogeneous nucleation is not common and only dominates at extremely high concentrations.[116,117] Membrane scaling can lead to a reduction in membrane permeability due to the blockage of pores by the growing crystals, which can cause membrane wetting and subsequent contamination of the recovered volume of pure water upon pore wetting.

The typical methods of scaling mitigation in MD desalination include pretreatment via the addition of antiscalants into the MD feed solution to slow down mineral salt nucleation and crystal growth,[118,119] and chemical membrane cleaning using acids with strong chelating ability.[120,121] Other scaling mitigation methods attempted include the reduction in feed solution residence time by increasing crossflow rate, backwashing with water or air, and the tailoring of membrane surface properties such as roughness, hydrophobicity, and charge.[83,122,123]

The development of improved scaling mitigation strategies relies on the fundamental understanding of the effects that operating parameters have on the propensity for scale formation. Calcium and sulfate ions are ubiquitously abundant in natural water, so calcium sulfate dihydrate

($CaSO_4{\cdot}2H_2O$, gypsum) is one of the most commonly encountered scale-forming compounds in membrane processes for brackish water and seawater desalination.[124–126] Studies have suggested that gypsum scaling propensity in membrane desalination can be influenced by feed solution temperature and water flux.[127,128] Specifically, gypsum induction is delayed when the feed solution temperature and the flux are simultaneously reduced. In direct-contact MD, liquid separation is driven by a vapor pressure gradient imposed between two solutions which are partitioned by a microporous, hydrophobic membrane.[13,63,129] The vapor pressure gradient is typically induced by heating the feed solution before it comes into contact with the hydrophobic membrane. Water evaporates at the membrane-feed interface before diffusing through the air trapped in the membrane pores and condensing at the cooler membrane-distillate interface (Figure 4.1). Because the water flux across the membrane is inherently linked to the temperature difference across the membrane, the isolation of one parameter is necessary to analyze the effects of the other parameter on mineral scaling.

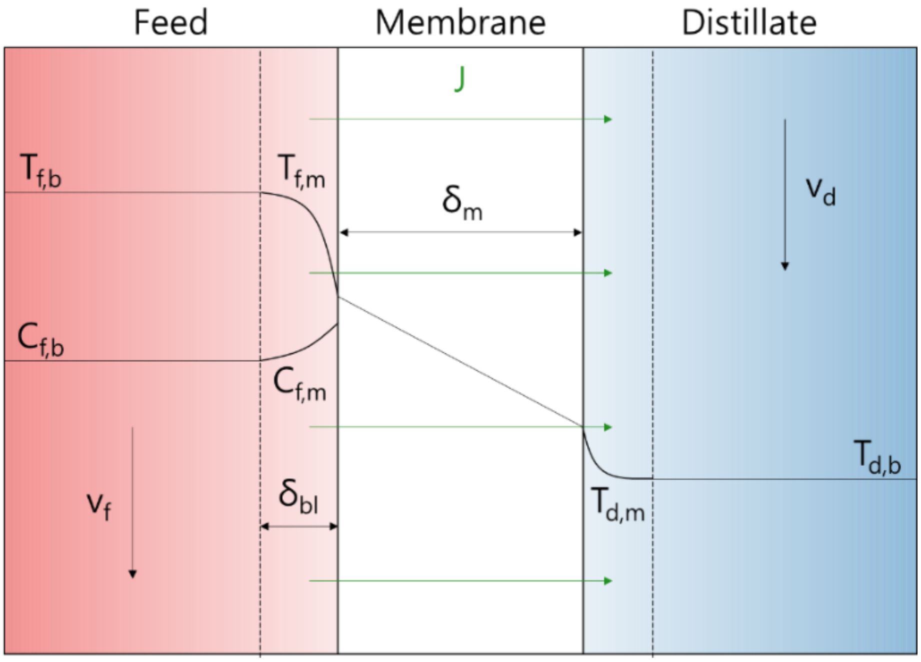

Figure 4.1 – Schematic of the membrane distillation (MD) process, including bulk feed temperature ($T_{f,b}$), interfacial feed temperature ($T_{f,m}$), bulk feed concentration ($c_{f,b}$), interfacial feed concentration ($c_{f,m}$), feed solution velocity (v_f), feed boundary layer for mass transfer (δ_{bl}), water flux (J), MD membrane thickness (δ_m), bulk distillate temperature ($T_{d,b}$), interfacial distillate temperature ($T_{d,m}$), and distillate solution velocity (v_d).

In this study, the individual effects of water flux and feed temperature on gypsum scaling in MD are systematically evaluated. By conducting two series of MD experiments to isolate the independent effects of water flux and feed temperature, then analyzing the critical water recovery at the point of flux decline (the generally accepted gypsum induction point), conclusions are drawn about the sensitivity of gypsum induction to either operating parameter. The influence of both temperature polarization and concentration polarization are considered through simple calculations based in established mass and heat transfer theory. The thermodynamic stability of the system is quantified using interfacial saturation index, and the energetic driving force for gypsum nucleation is considered via the Gibbs free energy for nucleation. It was observed that although water flux plays a larger role than feed temperature in the thermodynamic stability of the scale-forming precursors within the local feed-membrane interfacial region, feed temperature plays a larger role in the energetic formation of scale particles and is therefore more influential for gypsum nucleation in MD.

4.2. Theory and Methodology

4.2.1. Temperature and Concentration Polarization in MD

In order to describe the interfacial conditions for gypsum nucleation on the MD membrane surface and therefore yield meaningful comparisons between scaling events across several MD trials, it is necessary to evaluate the temperature polarization and concentration polarization within the MD module. Temperature polarization is affected by both the conductive heat transferred between the feed solution and the membrane and the convective heat transferred due to the transport of water vapor across the feed thermal boundary layer. Based on the method described by Qtaishat,[26] an overall heat balance was used to implicitly evaluate the interfacial temperatures in each experimental trial:

$$h_f\left(T_{f,b}-T_{f,m}\right)=JH_v+h_m\left(T_{f,m}-T_{d,m}\right)=h_d\left(T_{d,m}-T_{d,b}\right) \qquad \text{Eq. 4.1}$$

Where h_f, h_m, h_d are the heat transfer coefficients in the feed solution, membrane, and distillate solution, respectively. $T_{f,b}$ is the bulk feed temperature, $T_{f,m}$ is the interfacial feed temperature, J is the water flux, $T_{d,b}$ is the bulk distillate temperature, $T_{d,m}$ is the interfacial distillate temperature, and H_v is the enthalpy of water vapor. The heat transfer coefficients in the feed and distillate solutions were estimated using the definition of the Nusselt number (the convective to conductive heat transfer ratio at a fluid boundary):

$$h = \frac{Nu\kappa}{d} \qquad \text{Eq. 4.2}$$

Where h is the heat transfer coefficient, Nu is the Nusselt number, κ is the thermal conductivity of the solution, and d is the hydraulic diameter within the flow channel. The heat transfer coefficient through the membrane was calculated using the thermal conductivities of the hydrophobic membrane polymer and of the air trapped within the membrane's pores:

$$h_m = \frac{\kappa_g \varepsilon + \kappa_m (1 - \varepsilon)}{\delta_m} \qquad \text{Eq. 4.3}$$

Where κ_g is the thermal conductivity of air, κ_m is the thermal conductivity of polyvinylidene fluoride (PVDF), ε is the porosity of the membrane, and δ_m is the membrane thickness. The Nusselt number was estimated using the established correlation between the Nusselt number, the Reynolds number, and the Prandtl number:

$$Nu = ARe^b Pr^c \qquad \text{Eq. 4.4}$$

Where Nu is the Nusselt number, Re is the Reynolds number, Pr is the Prandtl number, and A, b, and c are the Nusselt coefficients. While c is usually assigned the value of 1/3 in MD literature,[30,130] the other Nusselt coefficients were determined iteratively using an optimization tool. The Reynolds and Prandtl numbers were calculated using the known physical properties of the solutions and of the flow channel.

Once the temperatures at the interfaces of the membrane surface and the solutions were determined, the temperature polarization coefficient (TPC) could be calculated to compare the magnitude of temperature polarization for each experimental trial.

$$TPC = \frac{T_{f,m} - T_{d,m}}{T_{f,b} - T_{d,b}} \quad \text{Eq. 4.5}$$

4.2.2. Gypsum Nucleation

The thermodynamic and kinetic stability of a salt solution is the most common gauge with which to indicate the likelihood of scale formation.[77,91,131] This stability can be evaluated through calculation of the saturation index (SI), which is the base-10 logarithm of the ratio of the ion activity product (IAP) and the solubility product constant (K_{sp}) (Eq. 4.6). The solubility product constant for gypsum as a function of temperature has been obtained by Marshall and Slusher[132] and others[133,134] for solutions from 0 to 100 °C, which informs the inverted solubility-temperature relationship above about 40 °C (Figure 4.2).

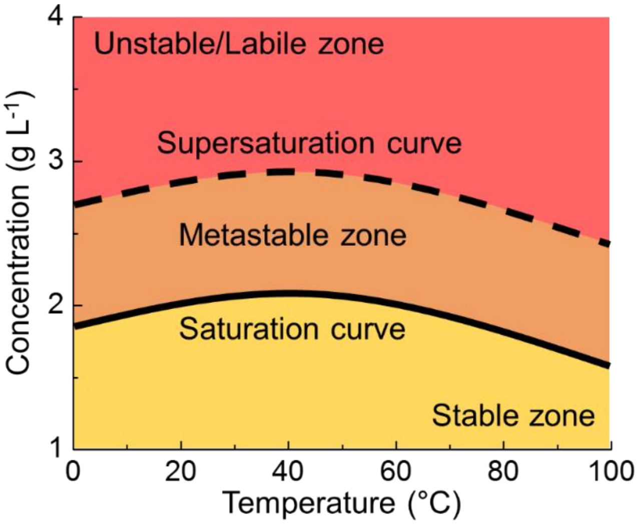

Figure 4.2 – Solubility of calcium sulfate dihydrate (gypsum) from 0-100 °C.[135] The stable zone (yellow region) indicates the concentration-temperature pairings that result in thermodynamically-favored dissolution of gypsum. Given enough time to equilibrate, all of the gypsum within the solution will dissolve into its associated calcium and sulfate ions. In the metastable zone (orange

region), gypsum crystals can form spontaneously. If a solution within the stable zone is concentrated or if the temperature is changed, and given enough time to equilibrate, some gypsum will precipitate out of the solution and the gypsum concentration within the solution will trend toward the solid line (the line separating the stable zone from the metastable zone) for any given temperature. The labile zone (red region) is poorly understood for heterogeneously-nucleating systems. It is unclear whether the dashed line (the line separating the metastable zone from the labile zone) represents a constant “meta equilibrium” point above which crystals begin to nucleate.

$$\mathrm{SI} = log\left(\frac{IAP}{K_{sp}}\right) \qquad \text{Eq. 4.6}$$

Solute concentration, which is increased at the feed-membrane interface by flux-dependent concentration polarization (CP), may increase the SI by increasing the IAP (Figure 4.3). Temperature, which is reduced at the feed-membrane interface by flux-dependent temperature polarization (TP) and directly controlled throughout the feed stream by the solution temperature chosen by the MD operator, affects precipitation kinetics via the temperature dependence of the free energy of reaction and the chemical potential difference which drives nucleation.[136]

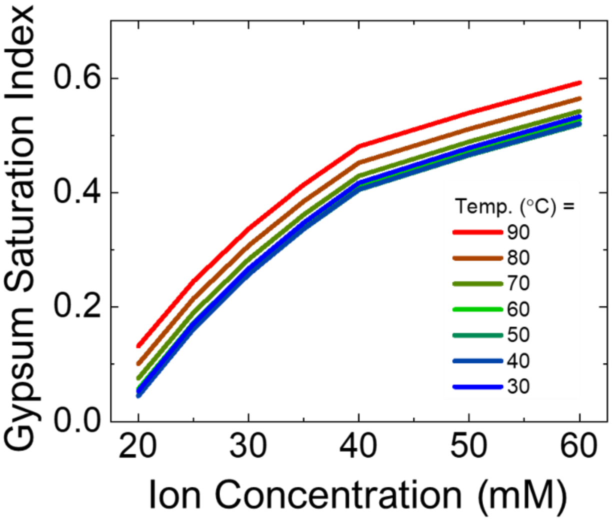

Figure 4.3 – Theoretical gypsum saturation index (calculated using PHREEQC[94]). Ion concentration represents the concentration of Ca^{2+} and SO_4^{2-} ions dissolved within the aqueous system. Higher ion concentrations correlate with a higher gypsum saturation index. A saturation index of zero represents perfect thermodynamic equilibrium in which, for a given temperature, no

more solute can be tolerated in the system without trending energetically toward precipitation. It should be noted that a saturation index above zero will not necessarily display immediate precipitation. Although a precipitation event would be favored energetically, the kinetics of the reaction must be taken into account. It may be the case that the energetically favored event is kinetically slow.

The SI, calculated using Eq. 4.6, is an ideal tool for the comparison of theoretical scaling propensity.

4.2.3. MD Experiments

4.2.3.1. Salts and membranes

Calcium chloride ($CaCl_2$) and sodium sulfate (Na_2SO_4) were purchased from Research Products International (Mount Prospect, IL). Both salts were used as received without further purification. PVDF membranes with a nominal pore diameter of 0.45 μm were purchased from GE Healthcare (Chicago, IL).

4.2.3.2. Experimental setup for membrane distillation

A co-current DCMD configuration was used to perform the experiments in this study (Figure C1). Centrifugal pumps were used to circulate the feed and the distillate solutions through the DCMD unit on either side of the MD membrane. The feed and distillate solution temperatures were monitored using digital temperature probes at the entrance and exit of both streams and adjusted using digitally-controlled constant-temperature baths in which heat exchanging coils were submerged. The distillate solution conductivity was measured over time through data captured by a dip-style conductivity probe. The water flux was monitored by calculating the volume of water transferred through the membrane over time using a balance (Eq. 4.7).

$$J = \frac{\Delta m}{(\Delta t)\rho A} \qquad \text{Eq. 4.7}$$

Where J is water flux, m is the mass of the distillate water, t is time, ρ is the density of the distillate water, and A is the active area of the membrane.

4.2.3.3. Membrane distillation scaling experiments

Each of the gypsum scaling experiments in this study were conducted using a 1 L feed solution composed of 20 mM $CaCl_2$ and 20 mM Na_2SO_4. The flowrates used for the feed and distillate solutions were 0.3 and 0.2 L min^{-1}, respectively. Prior to the commencement of each experiment, the temperatures of each stream and the water flux through the membrane were stabilized for at least 2 h using deionized (DI) water as both the feed and distillate solutions. $CaCl_2$ and Na_2SO_4 were added (5 min apart) once the DI water reached the target operating temperature and the target water flux was achieved. The change in both density and partial vapor pressure between DI water and the feed solutions was small (less than 2 %) for each solution,[137] so the values calculated for water flux during the stabilization period did not change after $CaCl_2$ and Na_2SO_4 were added.

The values for critical recovery (R*) in this study were taken to be the distillate water recovery percentage at the point where the gypsum scale coverage induced flux reduction of 85 % of its original value. This cutoff percentage is not meant to imply any theoretical significance, but rather to give a consistent rationale for the identification of the induction point described in other works without direct observation of gypsum nucleation via feed solution conductivity or quartz crystal microbalance measurements.[138,139] The identity of the scale layer which formed on the membrane surfaces was characterized using X-ray powder diffraction (XRD). The values for critical gypsum-forming ion concentration were calculated as the original bulk concentration multiplied by the volumetric concentration factor at the critical recovery point:

$$\mathrm{R}^* = \frac{\mathrm{V}^*}{V_0} \times 100 \qquad \text{Eq. 4.8}$$

$$\mathrm{c}^* = \frac{\mathrm{c}_0}{1 - \frac{\mathrm{V}^*}{V_0}} \qquad \text{Eq. 4.9}$$

Where V^* is the critical recovery volume, V_0 is the initial feed solution volume, c^* is the critical ion concentration of the feed solution, and c_0 is the initial ion concentration of the feed solution.

4.2.4. Evaluation of the Impact of Water Flux and Feed Temperature on Gypsum Scaling

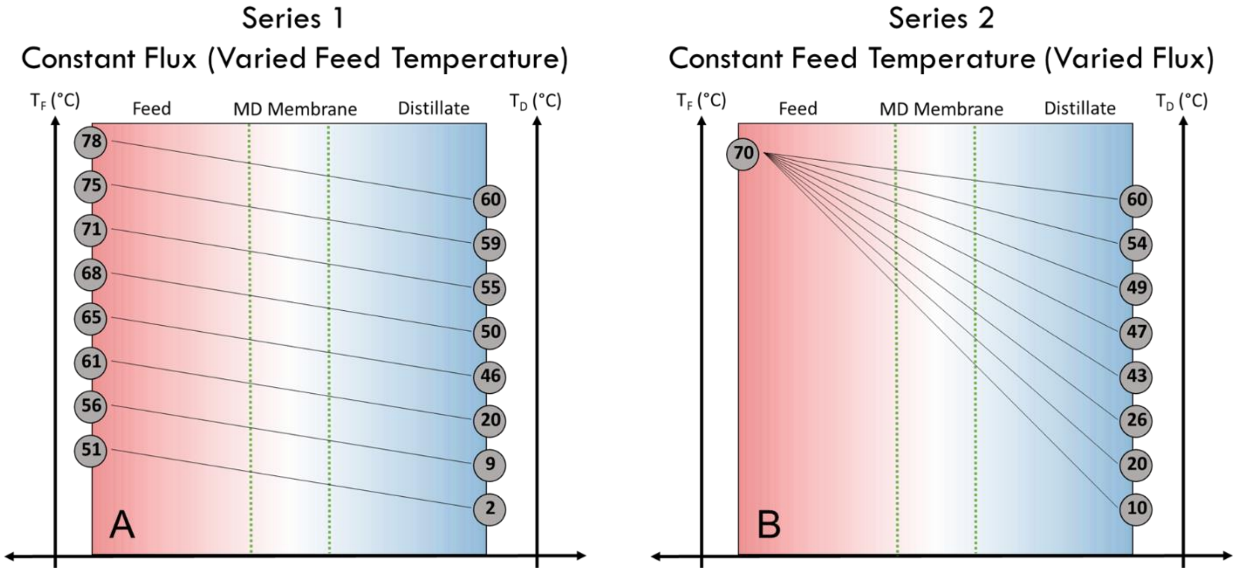

Figure 4.4 – Bulk feed and distillate solution temperature differences for gypsum scaling MD trials. Distillate solution temperature was unconventionally used to yield temperature-isolating and flux-isolating series of MD experiments. For series 1 (A), the water vapor flux was held constant at 15 L m^{-2} h^{-1} for temperature pairings ranging from a feed temperature of 50 – 80 °C. This feed temperature range was chosen because industrial applications of membrane distillation will most beneficially be coordinated with a low-grade waste heat source with an average temperature below 100 °C. For series 2 (B), the bulk feed solution temperature was held constant at 70 °C for water vapor fluxes ranging from 10 – 40 L m^{-2} h^{-1}.

4.2.4.1. MD experiments with constant water flux and varied feed temperature (Series 1)

By separating the effects of feed temperature from water flux, the sensitivity of gypsum nucleation to chemical potential differences can be evaluated without interference from the effects of CP and TP. This evaluation was carried out through a series of MD trials in which the feed solution temperature was increased from 30 to 80 °C, and the distillate temperature was simultaneously increased to yield a constant water flux of 15 L m^{-2} h^{-1} for each trial (Figure 4.4A).

4.2.4.2. MD experiments with constant feed temperature and varied water flux (Series 2)

Isolating the effects of water flux without influence from the effects of feed temperature allows for the evaluation of the direct effects of CP and TP on gypsum scaling in MD. In order to carry this out, a series of MD trials were conducted in which the feed solution temperature was maintained at 70 °C for each trial and the distillate solution temperature was adjusted to achieve water fluxes ranging from 10 to 40 L m^{-2} h^{-1} (Figure 4.4B). This feed temperature and water flux range were chosen because they are within the representative magnitude of the real parameters which are used in pilot-scale MD applications.[37,140,141].

Table 4.1 – Data table displaying key experimental values and calculated results for Chapter 4

			Bulk			Interface					
			Solution Temperature		Gypsum Ion Concentration	Solution Temperature		Gypsum Ion Concentration		Gypsum Saturation Index	
Series	Water Flux	Critical Recovery	Feed	Distillate	Initial	Feed	Distillate	Initial	Critical	Initial	Critical
	L m^{-2} h^{-1}	%	°C	°C	mM	°C	°C	mM	mM		
Constant Flux (Series 1)	15.6	34.7	77.8	60.1	20.0	71.5	67.5	24.9	38.2	0.192	0.409
	15.0	36.9	74.5	58.9	20.0	68.6	65.8	24.8	39.3	0.184	0.418
	15.2	39.6	71.2	55.0	20.0	65.1	62.2	24.9	41.2	0.179	0.436
	15.2	45.0	67.6	50.2	20.0	61.3	57.8	25.0	45.4	0.175	0.480
	15.0	46.9	64.5	46.2	20.0	58.1	54.0	25.0	47.1	0.170	0.495
	14.6	49.3	61.4	19.7	20.0	51.6	34.6	24.9	49.1	0.162	0.511
	14.9	52.3	56.1	8.99	20.0	45.6	26.67	25.1	52.6	0.163	0.545
	15.7	54.1	50.5	2.02	20.0	39.6	21.44	25.6	55.8	0.175	0.578
Constant Feed Temperature (Series 2)	38.9	39.8	71.8	9.72	20.0	54.6	39.7	35.0	58.2	0.340	0.599
	32.2	39.1	69.2	20.3	20.0	54.8	42.5	31.9	52.4	0.292	0.546
	28.0	39.6	70.8	26.3	20.0	57.9	45.3	29.9	49.5	0.262	0.520
	25.3	38.3	72.4	42.8	20.0	62.1	56.1	28.7	46.5	0.247	0.493
	22.6	37.8	70.6	47.1	20.0	61.8	58.1	27.7	44.5	0.228	0.470
	18.5	35.1	71.1	49.0	20.0	63.4	58.5	26.1	40.2	0.200	0.421
	15.2	34.3	71.1	54.4	20.0	65.0	61.7	24.9	37.9	0.179	0.393
	11.4	34.1	70.4	60.0	20.0	66.1	64.9	23.6	35.8	0.153	0.366

4.3. Results and Discussion

4.3.1. Gypsum Scaling Behavior

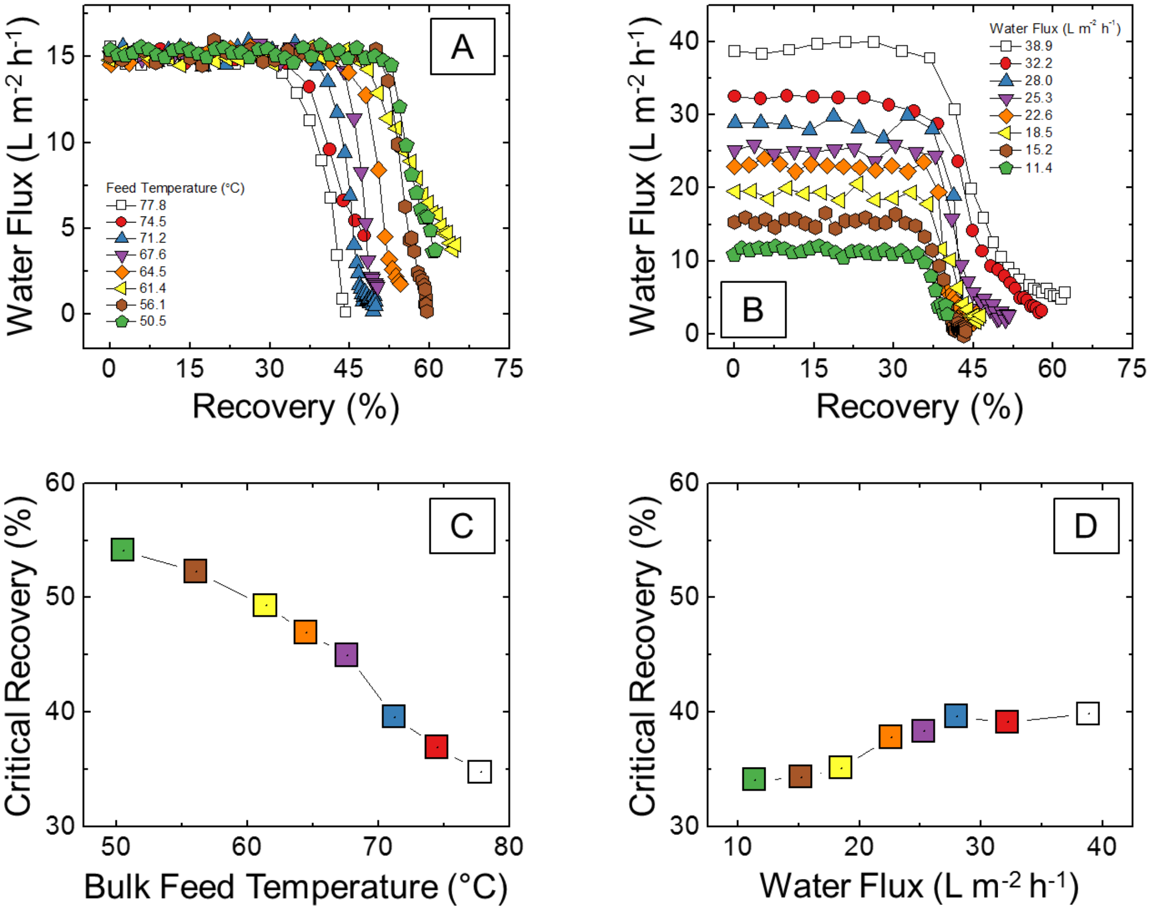

Figure 4.5 – (A,B) Water flux versus pure water recovery and (C,D) critical pure water recovery for gypsum scaling MD trials with (A,C) constant water flux, varied bulk feed solution temperature and (B,D) constant bulk feed solution temperature, varied water flux. The raw data from each MD trial is shown in Appendix C (Figure C5).

A total of sixteen different scaling experiments were performed to assess the individual impacts or either water flux or bulk feed solution temperature on critical pure water recovery and critical gypsum saturation index for a commercial microporous membrane. In each experiment, initial feed solution was composed of 20 mM $CaCl_2$ and 20 mM Na_2SO_4. As water was recovered on the distillate side of the membrane, the feed solution became increasingly concentrated and eventually supersaturated. Significant flux decline was observed in each trial as gypsum crystals formed and grew to cover the membrane pores.[91] The observation that gypsum was the only precipitating phase of calcium sulfate within the temperature range explored, as opposed to simultaneous or competitive precipitation of calcium sulfate anhydrite ($CaSO_4$) and calcium sulfate hemihydrate ($CaSO_4 \cdot 1/2H_2O$, bassanite), is confirmed by XRD analysis (Figure C6) and is in agreement with the results from previous studies.[142,143] The critical recovery achieved during each scaling experiment ranged from 30 to 60 % for varied-temperature Series 1 (Figure 4.5A,C) and from 30 to 40 % for varied-flux Series 2 (Figure 4.5B,D). It was observed that higher bulk feed temperature resulted in earlier flux decline and thus lower critical recovery (Figure 4.5C). The lower critical recovery observed at higher bulk feed temperature corresponds with a lower saturation index tolerated at the membrane surface. Similarly, lower interfacial feed temperature corresponds with lower critical saturation index for both Series 1 and Series 2 (Figure 4.6A). That is, regardless of the water flux applied during the MD desalination experiment, the systems with lower interfacial feed temperature always tolerated higher gypsum saturation index before flux decline. It was observed in Series 2 that higher water flux resulted in slightly delayed flux decline and thus higher critical recovery (Figure 4.5D). The slight change in critical recovery with varied flux is likely attributable to the lower interfacial solution temperature at higher flux due to increased TP. This observation gives support to the notion that temperature is more influential than ion concentration for gypsum scaling in MD. Furthermore, the results from Series 2 indicate that higher saturation index can be tolerated before flux decline for trials with higher water flux in spite of the higher interfacial ion concentration due to enhanced CP (Figure 4.6B). Interestingly, the higher propensity for scaling that one might expect at higher water flux (due to enhanced CP) is offset by the lowered interfacial solution temperature at higher water flux. Counterintuitively, in both Series 1 and Series 2, the trials in which the highest saturation index was tolerated were also the trials in which the most dramatic CP was observed, most likely due to the lower interfacial temperature described previously. These results are consistent with other studies that build upon the generally accepted theory of gypsum precipitation kinetics and thermodynamics,[144,145] in that higher temperatures accelerate nucleation kinetics.

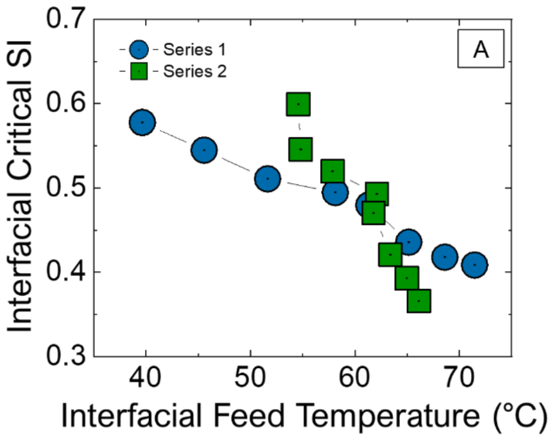

Figure 4.6 – Interfacial critical saturation index versus (A) bulk feed temperature and (B) water flux.

Maximizing critical pure water recovery by delaying the onset of membrane scaling using optimal operating conditions is beneficial for practical applications of MD for treating high-salinity brine. Intuition may lead one to expect that the critical saturation index observed during each trial would be the same. This incorrect assumption is quite forgivable since the saturation index is a thermodynamic metric of phase stability and is calculated with consideration to both ion activity and solution temperature. While the theoretical saturation index may be an accurate metric to quantify the stability of a supersaturated solution, it is incomplete to view saturation index as a predictive governing metric for comparative crystal nucleation and subsequent growth in MD. That is, two solutions of identical composition and differing temperature will begin to precipitate gypsum at different saturation indices. The saturation index is a metric for thermodynamic favorability of the precipitation reaction, but says nothing of the kinetic favorability of the precipitation reaction.

4.3.2. Explanation for Variation in Critical Saturation Index

The crystallization mechanism is well-understood for solutions which are supersaturated with salt-forming ions. The force which drives the growth of crystals in liquid solutions is the supersaturation of crystal-forming species within a solution. The supersaturation can be considered as the difference between the chemical potential of a molecule in the solution and the chemical potential of a molecule in the bulk of the crystal phase.[146] Nucleation, the process with which the formation of new phases begins, will only occur when the chemical potential difference is positive.

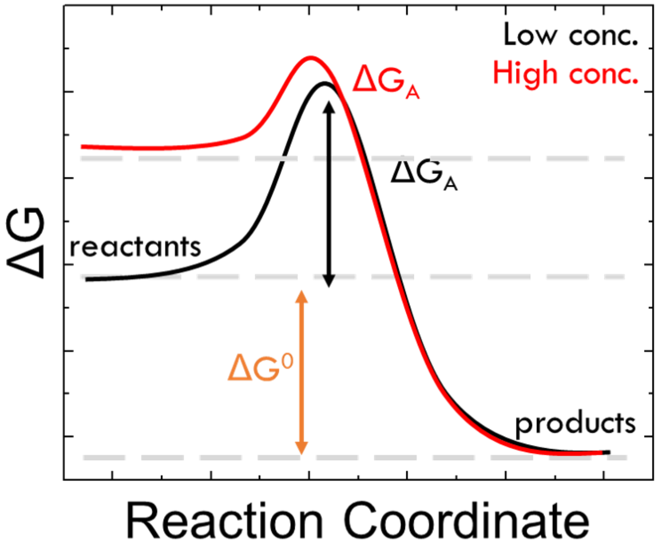

Figure 4.7 – Plot showing the typical trend in Gibbs free energy as a precipitation reaction proceeds. As the concentration of the reactant ions increases, either temporally via pure water removal (i.e., distillation-driven concentration) or generally via implementation of a high water vapor flux during MD (which would increase concentration polarization effects), the energy barrier which resists crystal formation shrinks. When the influence of temperature is considered, heating will tend to increase the kinetic energy of the nucleus-forming ions, thereby increasing the kinetic favorability of the reaction, which can be observed as a higher propensity for crystal formation and therefore scaling in MD.

Once a nucleus of adequate size is formed in a crystal-precipitating solution, progressive crystal growth is observed to be carried out as governed by the various rate equations discussed in the related literature.[147] This mechanism is in fact the pathway through which gypsum precipitation proceeds. In order for ions within a liquid solution to spontaneously bond, the ions within the supersaturated solution must first shed their hydration shell and overcome the energy difference between the dissolved and crystalline states of matter (i.e. the chemical potential difference). This barrier for nucleation may be influenced by the solution temperature. Alternatively, this barrier for nucleation may be influenced by the concentration of the ions within the solution. Figure 4.7

illustrates how the height of the energetic barrier for nucleation may affect the precipitation in a supersaturated aqueous environment.

The Series 2 trials displayed variation in interfacial feed temperature even though the bulk feed temperature was held constant at 70 °C. This is attributable to the TP phenomenon in which more latent heat leaves the feed stream at higher water flux values. This decrease in interfacial temperature in the feed stream among each of the trials was unintended, but interesting, nonetheless. The goal was to isolate the effects of water flux in Series 2, but actually, the effects of water flux and solution temperature were both impacting gypsum nucleation. Therefore, the intended comparison of temperature effects vs. flux effects turned into a comparison of temperature effects vs. flux and temperature effects. In order to truly isolate the effects of water flux on gypsum nucleation, one must vary the bulk feed temperature such that the TP phenomena yields the same interfacial temperature in each trial. However, this unintended change in interfacial solution temperature during Series 2 allowed us to further probe the dependence of gypsum nucleation conditions on the solution temperature. From both Series 1 and Series 2, it is apparent that feed temperature plays the largest role in gypsum scaling in MD.

4.4. Implications

This work revealed, through a systematic series of experiments in which the exclusive effects of either feed temperature or water flux were isolated, that gypsum scaling in direct-contact membrane distillation (DCMD) is predominantly influenced by the temperature of the feed solution at the membrane-feed interface. The estimate of the apparent standard free energy of reaction supported further this conclusion. The interfacial temperature calculations were performed using established mass and heat transfer theory alongside experimentally derived flux values. The critical recoveries afforded to the lowest feed temperatures employed were greater than those at the highest feed temperatures by almost 200%. Contrastingly, the variations in ion concentration at the membrane-feed interface did not display any notable trend.

This work sheds useful insights into the effect that water flux and feed solution temperature play in gypsum scaling in MD. Based on the results herein, we propose the application of the highest water flux achievable with the lowest temperature feasible for MD treatment of high-salinity brine that is saturated with gypsum forming ions, calcium and sulfate. It should be noted that each membrane cell has its own physical characteristics that will change the mass and heat transfer calculations in MD. The results reported here require validation across a range of feed and distillate flow rates, feed solution compositions, and MD operating regimes for broad-sweeping claims to be extracted regarding gypsum nucleation. Also, further characterization of the morphology and growth rate of the scale layers in each trial will provide valuable insights onto the physical characteristics of the crystals grown in the most aggressive scaling environments.

CHAPTER 5

5. Conclusions and Future Work

5.1. Conclusions

The work presented in this dissertation has centered on the energy efficiency and scaling vulnerability of MD for applications in high-salinity brine treatment. In order for MD to be applied effectively, it is crucial that we improve our understanding of the utilization efficiency of the thermal energy used to drive separation, the key mechanisms for scaling-induced membrane wetting, and the effects that operating parameters have on the nucleation and growth of scale-forming minerals.

Chapter 1 gave the motivation and outlook for this dissertation. Global water scarcity and growing environmental awareness contribute to the necessity for the development and optimization of efficient and resilient technologies for brine treatment.

Chapter 2 offered the energy efficiency analysis of an MD system in varying operational contexts. First, the importance of balancing heat capacity flows between the feed and distillate streams in MD for optimal performance was demonstrated. Then, an approximation for the maximum single pass water recovery was presented based on a simple energy balance over the vapor. We then provide a framework for evaluating the energy efficiency of MD in two configurations, with and without an integrated heat exchanger (HX) to recover latent heat from the distillate stream. Then, we define a new metric, specific yield, which quantifies the performance of MD powered by waste heat stream. For a single-stage MD powered by a waste heat stream, whether implementing latent heat recovery or not only affects the SEC_{th} (or GOR) of the process, but not the specific yield. This result is notable because the wide-spread use of MD hinges upon its successful integration with waste heat streams.

Chapter 3 identified distinctions between the effects of two of the most common scalants in membrane wastewater treatment, gypsum and silica. When experiments of identical initial saturation index were conducted, gypsum scaling caused much earlier decline of water flux and induced membrane wetting that was not observed in silica scaling. These results lead to the conclusion that cost-effective measures for scaling control, whether via pretreatment to remove scaling precursors, adding anti-scalant chemicals, or developing scaling-resistant membranes, should be prioritized toward mitigating scalants which are formed through crystallization.

Chapter 4 investigated the individual impacts of water flux and feed solution temperature on gypsum scaling in MD. Sixteen individual trials were conducted, and, through the application of distillate temperature control, half of the trials displayed constant feed temperature and varied flux, and the other half of the trials displayed constant water flux and varied feed temperature. By combining the resulting experimental data with a semi-empirical mass transfer and heat transfer model, the characteristics and scaling propensity at the local membrane-feed interface were evaluated and compared across each trial. It was observed that the maximum saturation index tolerated (i.e., critical SI) before crystal growth varies with temperature. That is, the thermodynamic stability of the system (SI) is insufficient for the prediction of nucleation and growth in MD. In practice, the driving force for crystal growth is more closely linked to temperature than ion concentration or thermodynamic stability.

Overall, this work provided a novel enhancement to our understanding of the barriers and considerations for the application of MD to brine treatment. The broader impacts of this work lie squarely within the goals of the water treatment community, which include the efficient management of high-salinity brines and wastewaters with complex and sparingly-soluble composition while moving toward complete water recovery and ZLD. As a result of the quantitative analyses presented here, we have moved one step closer to the optimization of a promising liquid separation mechanism that can help to alleviate global water scarcity by enabling the efficient reuse of water from high-salinity brines without performance failure from scaling and scaling-induced pore wetting.

5.2. Future Work

There are many additional research questions and future areas of work that arise from the overall conclusions and findings of this dissertation. For example, the theoretical analysis presented in Chapter 2 may be applied to real systems to evaluate the agreement between the predicted and experimentally acquired efficiency values. The analysis presented was built upon the assumption that the membrane used during MD was one with adequate membrane area to allow for the maximum heat and vapor transport. In practice, sub-maximal heat and vapor transport due to insufficient membrane area can alter the resulting analytical insights. Also, the natural conclusion of the work reflects the complex nature of high-efficiency desalination. Multiple stages of DCMD modules integrated with an HX to recover latent heat may be implemented to simultaneously improve η_{ws} and SEC_{th}. This assertion can be easily tested experimentally, and will certainly be of interest for any industrial partners who seek to maximize the efficient output of their MD systems for brine treatment.

The experimental investigation presented in Chapter 3 may be extended to include other common scale-forming minerals like calcium carbonate, sodium chloride, and sodium sulfate, as well as the co-precipitation of each combination of scalants. This analysis is critical because it is rare that one lone scaling species challenges an MD membrane during real applications. Furthermore, it has been shown that the co-precipitation of certain species can exhibit worse outcome than the precipitation of either species alone.[148] Also, it would be highly relevant to explore the different scaling mechanisms and outcomes for various salts on superhydrophobic membranes. Superhydrophobic membranes have been shown to delay incipient nucleation due to the low surface energy of the outermost chemical functional groups reducing the favorability of heterogeneous nucleation.

Chapter 4 shows that the main function of operating parameter control for MD of high-salinity brines is to regulate the interfacial temperature. Whether controlling the bulk feed temperature, the water flux, the cross flow rate, the MD configuration, the membrane thickness, or any other controllable parameter in MD, it is expected that the interfacial temperature is the dominant manipulator of gypsum scaling propensity. This is due to the dependence of the thermal energy of the dissolved ions on temperature. We can verify this expectation to explore whether the other operating parameters, especially feed solution residence time, plays as large of a role as temperature on gypsum nucleation.

APPENDIX

A. Supporting Information for Chapter 2

A.1. Expressions for Critical Flow Rate Ratio (FRR, α*)

Precise FRR (distillate-limited regime, DLR):

$$\alpha \leq \alpha_{DLR} = \alpha^{*} = \frac{(T_H - T_C^{*})\left(\frac{\bar{h}_{v,D}}{c_D} - \frac{T_H^{*} - T_C}{2}\right)}{(T_H^{*} - T_C)\left(\frac{\bar{h}_{v,D}}{c_F} + \frac{c_D}{c_F}\frac{T_H + T_C^{*}}{2} - T_C^{*}\right)} \qquad \text{Eq. A1}$$

Precise FRR (feed-limited regime, FLR):

$$\alpha \geq \alpha_{FLR} = \alpha^{*} = \frac{(T_H - T_C^{*})\left(\frac{\bar{h}_{v,F}}{c_D} + \frac{T_H + T_C^{*}}{2} - T_H^{*}\right)}{(T_H^{*} - T_C)\left(\frac{\bar{h}_{v,F}}{c_F} + \frac{c_D}{c_F}\frac{T_H + T_C^{*}}{2} - T_C^{*}\right)} \qquad \text{Eq. A2}$$

Estimated FRR:

$$\alpha^{*} = \frac{c_F}{c_D} \qquad \text{Eq. A3}$$

Improved estimated FRR:

$$\alpha^{*} = \frac{c_F}{c_D}\frac{\bar{h}_v - c_F\,\Delta T/2}{\bar{h}_v + c_D\,\Delta T/2} \qquad \text{Eq. A4}$$

A.2. Threshold Temperature Difference

The threshold temperature difference (ΔT_{th}) accounts for partial vapor pressure depression in the feed solution due to the presence of solute and is defined as:

$$\Delta T_{th} = T_H^* - T_C \quad (or\ T_H - T_C^*) \qquad \text{Eq. A5}$$

When the temperature difference between feed and distillate at position x along the MD module ($\Delta T(x)$) reaches the threshold temperature difference, the driving force for vapor flux, or transmembrane vapor pressure difference, goes to zero. Mathematically the threshold feed temperature (T_H^*) is:

$$p_w\big(C(x), T_H^*(x)\big) = p_w(0, T_C(x)) \qquad \text{Eq. A6}$$

and the threshold distillate temperature (T_C^*) is:

$$p_w\big(C(x), T_H(x)\big) = p_w(0, T_C^*(x)) \qquad \text{Eq. A7}$$

A.3. Values for Critical Flow Rate Ratio (FRR, α*)

Table A2 – Values for the precise critical flow rate ratio at varied feed influent temperatures and feed influent salinities

Precise FRR (Eq. A2)						
Feed Influent Salinity (mol NaCl kg^{-1} H$_2$O)	*Feed Influent Temperature (°C)*					
	40	**50**	**60**	**70**	**80**	**90**
0.0	0.966	0.950	0.933	0.916	0.900	0.884
0.5	0.935	0.919	0.903	0.888	0.872	0.856
1.0	0.909	0.894	0.879	0.863	0.848	0.832
1.5	0.887	0.872	0.858	0.843	0.828	0.813
2.0	0.868	0.854	0.839	0.825	0.810	0.796
2.5	0.851	0.838	0.824	0.810	0.795	0.781
3.0	0.837	0.824	0.810	0.796	0.782	0.768
3.5	0.825	0.812	0.798	0.785	0.771	0.757
4.0	0.815	0.802	0.788	0.775	0.761	0.748
4.5	0.806	0.793	0.780	0.767	0.753	0.740
5.0	0.799	0.786	0.773	0.760	0.747	0.734

Table A3 – Values for the estimated critical flow rate ratio at varied feed influent temperatures and feed influent salinities

Estimated FRR (Eq. A3)						
Feed Influent Salinity (mol NaCl kg^{-1} H$_2$O)	*Feed Influent Temperature (°C)*					
	40	**50**	**60**	**70**	**80**	**90**
0.0	0.999	0.999	1.00	1.00	1.01	1.01
0.5	0.966	0.967	0.969	0.971	0.975	0.980
1.0	0.938	0.939	0.941	0.943	0.947	0.951
1.5	0.913	0.914	0.916	0.919	0.922	0.926
2.0	0.891	0.892	0.894	0.896	0.900	0.904
2.5	0.871	0.873	0.874	0.876	0.880	0.884
3.0	0.853	0.855	0.857	0.859	0.862	0.866
3.5	0.838	0.839	0.841	0.843	0.846	0.850
4.0	0.824	0.825	0.827	0.829	0.832	0.835
4.5	0.812	0.813	0.814	0.816	0.819	0.823
5.0	0.801	0.802	0.803	0.805	0.808	0.812

Table A4 – Values for the improved estimate for critical flow rate ratio at varied feed influent temperatures and feed influent salinities

Improved Estimated FRR (Eq. A4)						
Feed Influent Salinity (mol NaCl kg^{-1} H$_2$O)	*Feed Influent Temperature (°C)*					
	40	**50**	**60**	**70**	**80**	**90**
0.0	0.965	0.949	0.933	0.919	0.906	0.894
0.5	0.934	0.919	0.904	0.891	0.879	0.867
1.0	0.907	0.893	0.880	0.867	0.855	0.844
1.5	0.883	0.870	0.857	0.845	0.833	0.823
2.0	0.862	0.849	0.837	0.825	0.814	0.804
2.5	0.843	0.831	0.819	0.808	0.797	0.787
3.0	0.827	0.815	0.803	0.793	0.782	0.772
3.5	0.812	0.800	0.789	0.778	0.768	0.759
4.0	0.799	0.787	0.776	0.765	0.756	0.747
4.5	0.787	0.775	0.765	0.754	0.745	0.736
5.0	0.776	0.765	0.755	0.744	0.735	0.726

Table A5 – Percentage difference between the precise and estimated critical flow rate ratio at varied feed influent temperatures and feed influent salinities

Percentage Difference Between Precise (Eq. A2) and Estimated FRR (Eq. A3) (%)						
Feed Influent Salinity (mol NaCl kg^{-1} H$_2$O)	*Feed Influent Temperature (°C)*					
	40	**50**	**60**	**70**	**80**	**90**
0.0	3.37	5.24	7.25	9.43	11.8	14.5
0.5	3.32	5.22	7.24	9.42	11.8	14.5
1.0	3.16	5.07	7.09	9.25	11.6	14.3
1.5	2.92	4.81	6.83	8.98	11.3	14.0
2.0	2.63	4.52	6.50	8.64	11.0	13.6
2.5	2.30	4.17	6.14	8.26	10.6	13.2
3.0	1.92	3.79	5.74	7.85	10.2	12.7
3.5	1.54	3.38	5.32	7.41	9.70	12.2
4.0	1.13	2.94	4.87	6.93	9.21	11.7
4.5	0.695	2.48	4.39	6.44	8.71	11.2
5.0	0.225	2.01	3.89	5.93	8.18	10.7

Table A6 – Percentage difference between the precise and improved estimate for critical flow rate ratio at varied feed influent temperatures and feed influent salinities

Percentage Difference Between Precise (Eq. A2) and Improved Estimated FRR (Eq. A4) (%)						
Feed Influent Salinity (mol NaCl kg^{-1} H$_2$O)	*Feed Influent Temperature (°C)*					
	40	**50**	**60**	**70**	**80**	**90**
0.0	0.125	0.075	0.047	0.271	0.634	1.171
0.5	0.11	0.004	0.158	0.411	0.792	1.336
1.0	0.217	0.077	0.114	0.388	0.786	1.341
1.5	0.406	0.245	0.036	0.254	0.667	1.235
2.0	0.653	0.478	0.257	0.046	0.472	1.054
2.5	0.941	0.759	0.529	0.216	0.221	0.815
3.0	1.264	1.078	0.842	0.521	0.075	0.53
3.5	1.616	1.428	1.188	0.861	0.408	0.207
4.0	1.993	1.806	1.563	1.232	0.773	0.15
4.5	2.394	2.207	1.963	1.629	1.166	0.538
5.0	2.817	2.632	2.387	2.052	1.586	0.954

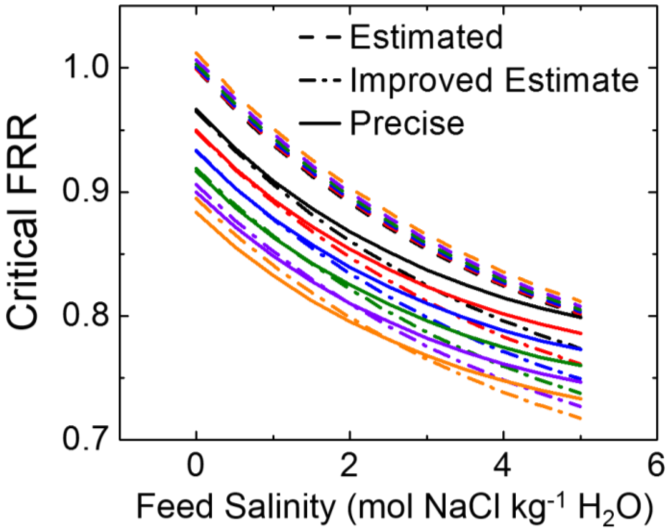

Figure A1 – Precise and estimated critical flow rate ratio (FRR) for feed influent temperatures of 40 °C (black), 50 °C (red), 60 °C (blue), 70 °C (green), 80 °C (purple), and 90 °C (orange)

A.4. Expressions for Water Recovery (R)

Precise R^{DLR} (distillate limiting regime, DLR):

$$R^{DLR} = \alpha \frac{T_H^* - T_C}{\left(\frac{\bar{h}_{v,D}}{c_D} - \frac{T_H^* - T_C}{2}\right)} \qquad \text{Eq. A8}$$

Precise R^{FLR} (feed limiting regime, FLR):

$$R^{FLR} = R_{max} = \frac{T_H - T_C^*}{\frac{\bar{h}_{v,F}}{c_F} + \frac{c_D}{c_F}\left(\frac{T_H^* + T_C}{2}\right) - T_C^*} \qquad \text{Eq. A9}$$

Estimated R_{max}:

$$R_{max} = R_{max}^{FLR} = \frac{\Delta Q_{max}}{Q_F} = \frac{\eta_{th} c_F}{\bar{h}_v} \Delta T \qquad \text{Eq. A10}$$

A.5. Values for Water Recovery Limit (R_{max})

Table A7 – Values for the precise water recovery limit at varied feed influent temperatures and feed influent salinities

Precise R_{max} (Eq. A9) (%)						
Feed Influent Salinity (mol NaCl kg^{-1} H$_2$O)	*Feed Influent Temperature (°C)*					
	40	**50**	**60**	**70**	**80**	**90**
0.0	3.38	5.05	6.71	8.38	10.1	11.7
0.5	3.22	4.84	6.45	8.06	9.68	11.3
1.0	3.08	4.65	6.21	7.78	9.34	10.9
1.5	2.95	4.48	6.00	7.52	9.05	10.6
2.0	2.83	4.32	5.80	7.29	8.77	10.3
2.5	2.72	4.17	5.62	7.07	8.53	9.99
3.0	2.61	4.04	5.46	6.88	8.30	9.73
3.5	2.51	3.91	5.30	6.69	8.09	9.49
4.0	2.41	3.79	5.16	6.53	7.90	9.28
4.5	2.32	3.68	5.02	6.37	7.72	9.08
5.0	2.24	3.57	4.90	6.23	7.56	8.90

Table A8 – Values for the estimated water recovery limit at varied feed influent temperatures and feed influent salinities

Estimated R_{max} (Eq. A10) (%)						
Feed Influent Salinity (mol NaCl kg^{-1} H$_2$O)	*Feed Influent Temperature (°C)*					
	40	**50**	**60**	**70**	**80**	**90**
0.0	3.44	5.18	6.95	8.74	10.6	12.5
0.5	3.32	5.01	6.72	8.46	10.2	12.1
1.0	3.22	4.87	6.53	8.22	9.94	11.7
1.5	3.14	4.74	6.36	8.00	9.68	11.4
2.0	3.06	4.62	6.20	7.80	9.44	11.1
2.5	2.99	4.52	6.06	7.63	9.23	10.9
3.0	2.93	4.42	5.94	7.47	9.04	10.6
3.5	2.88	4.34	5.83	7.33	8.87	10.4
4.0	2.83	4.27	5.73	7.21	8.72	10.3
4.5	2.79	4.20	5.64	7.10	8.58	10.1
5.0	2.75	4.15	5.56	7.00	8.46	9.97

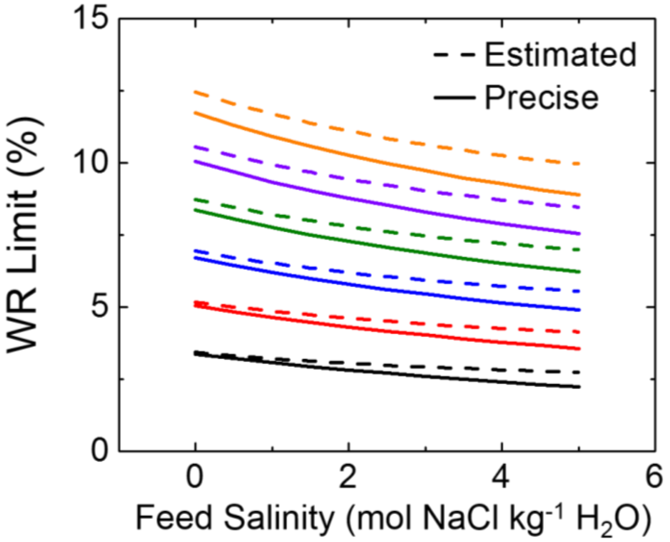

Figure A2 – Precise and estimated water recovery (WR) limit for feed influent temperatures of 40 °C (black), 50 °C (red), 60 °C (blue), 70 °C (green), 80 °C (purple), and 90 °C (orange)

A.6. Nomenclature

Table A9 – Description of the symbols used in the equations of Appendix A

Symbol	Description
α	Flow rate ratio (Q_D/Q_F)
α^*	Critical flow rate ratio (flow rate ratio at which heat and mass transfer across the MD membrane is optimized within and MD module)
α_{DLR}	Critical flow rate ratio in the distillate limiting regime
α_{FLR}	Critical flow rate ratio in the feed limiting regime
T_H	Temperature of the heat source (°C)
T_C	Temperature of the heat sink (°C)
ΔT	$T_H - T_C$ (°C)
ΔT_{th}	Threshold temperature difference
T_H^*	Feed threshold temperature (temperature of pure water at which its partial vapor pressure is equal to the water partial vapor pressure of an NaCl solution at temperature T_H) (°C)
T_C^*	Distillate threshold temperature (temperature of an NaCl solution at which its water partial vapor pressure is equal to the partial vapor pressure of pure water at temperature T_C) (°C)
$p_w(C(x), T_i(x))$	Partial vapor pressure of water as a function of the solute concentration at position x along the MD module ($C(x)$) and temperature of stream "i" at position x along the MD module ($T_i(x)$)

$\bar{h}_{v,D}$	Average specific enthalpy of vaporization of the distillate stream (kJ kg^{-1})
$\bar{h}_{v,F}$	Average specific enthalpy of vaporization of the feed stream (kJ kg^{-1})
$\bar{h}_{v}$	Average specific enthalpy of vaporization of water for $\Delta T/2$ (kJ kg^{-1})
c_D	Heat capacity of the distillate stream (kJ kg^{-1} °C^{-1})
c_F	Heat capacity of the feed stream (kJ kg^{-1} °C^{-1})
R^{DLR}	Water recovery in the distillate limiting regime
R^{FLR}	Water recovery in the feed limiting regime

B. Supporting Information for Chapter 3

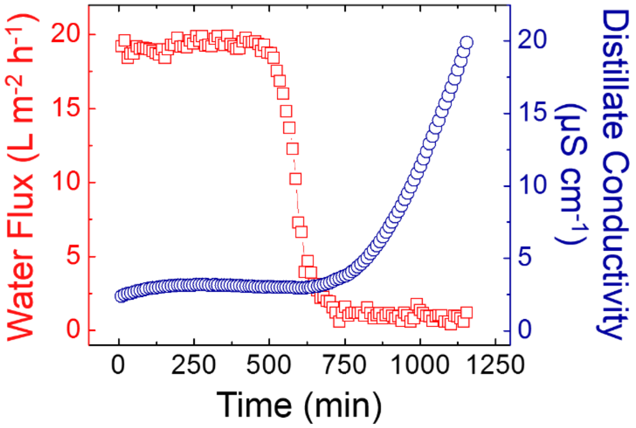

Figure B1 – Water flux (red) and distillate conductivity (blue) in MD experiments with gypsum scaling. The feed solution had an initial gypsum SI of 0.05. The feed and distillate temperatures were 60 °C and 20 °C, respectively, and the feed and distillate flow rates were 0.45 and 0.3 L min-1, respectively. A commercial PVDF membrane (Amersham Hybond, GE Healthcare) was used to generate the date in this figure.

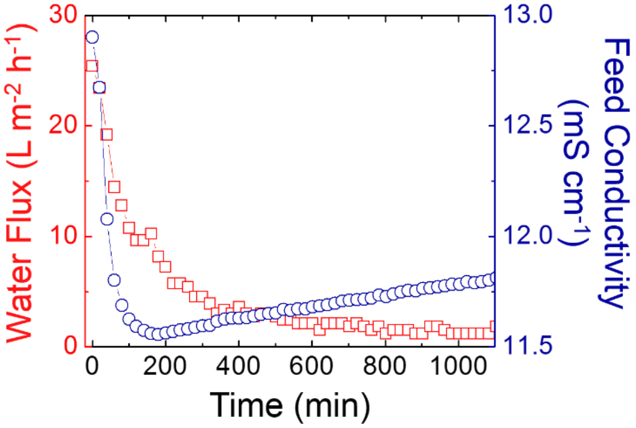

Figure B2 – Water vapor flux (red) and feed conductivity (blue) in MD experiments with gypsum scaling. This data is replotted from Figure 3.2A of the main text to display (by narrowing the range of the right y-axis) the slight increase in feed conductivity observed throughout the trial.

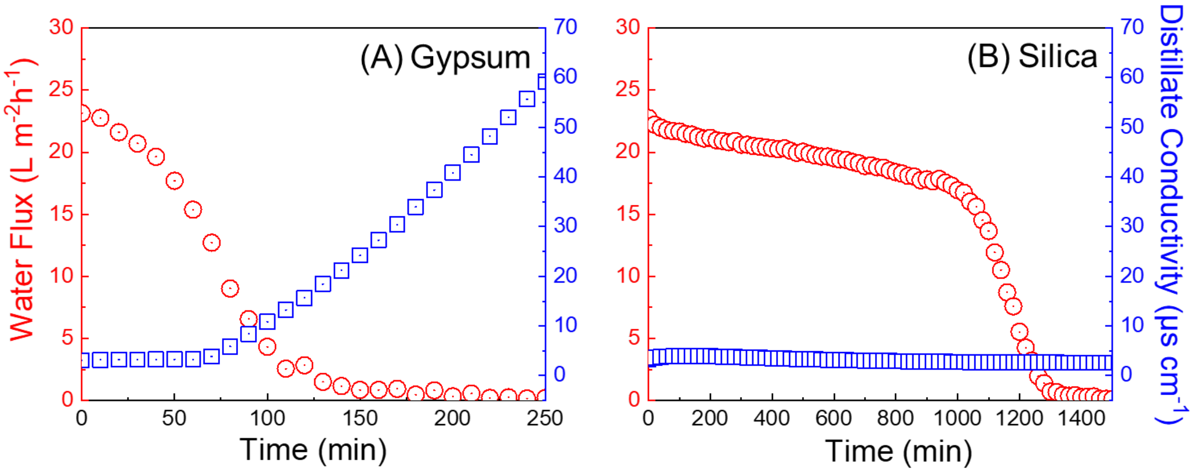

Figure B3 - (A and B) Water vapor flux (red) and distillate conductivity (blue) in MD experiments with (A) gypsum scaling and (B) silica scaling. The initial pH of the feed solution was 6.5 in both cases. A commercial PVDF membrane (HVHP Durapore, Millipore Sigma) was used to generate the data of this figure, which serves as independent results to support those of Figure 3.2 of the main text.

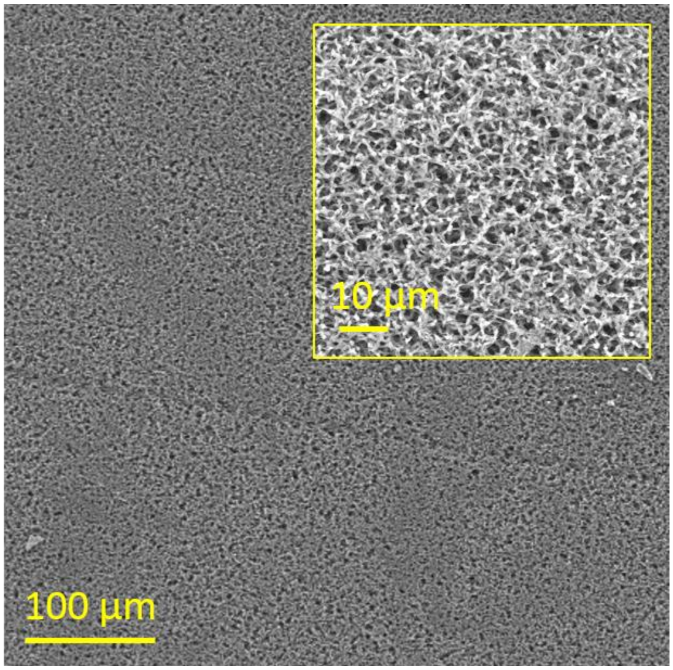

Figure B4 - Top-down scanning electron microscope (SEM) image of a pristine polyvinylidene fluoride (PVDF) membrane

Table B1 - Summary of Mechanical Properties from Tensile Testing

Break Strain (%)			
Sample #	No scalant	Silica scaling	Gypsum scaling
1	45.9	43.7	2.7
2	39.0	44.1	2.1
3	38.6	40.1	3.2
4	42.7	39.3	4.1
5	41.9	39.6	3.4
Mean	41.6	41.4	3.1
Standard Deviation	3.0	2.4	0.75
Break Stress (MPa)			
Sample #	No scalant	Silica scaling	Gypsum scaling
1	5.06	4.76	4.92
2	5.03	4.34	4.94
3	4.53	4.57	4.42
4	4.81	4.29	4.45
5	4.37	4.46	4.69
Mean	4.76	4.48	4.68
Standard Deviation	0.31	0.19	0.25
Toughness (MPa)			
Sample #	No scalant	Silica scaling	Gypsum scaling
1	2.18	1.77	0.298
2	1.90	1.89	0.231
3	1.69	1.66	0.233
4	1.95	1.68	0.254
5	1.74	1.85	0.214
Mean	1.89	1.77	0.246
Standard Deviation	0.20	0.10	0.032

C. Supporting Information for Chapter 4

C.1. Setup and Characterization

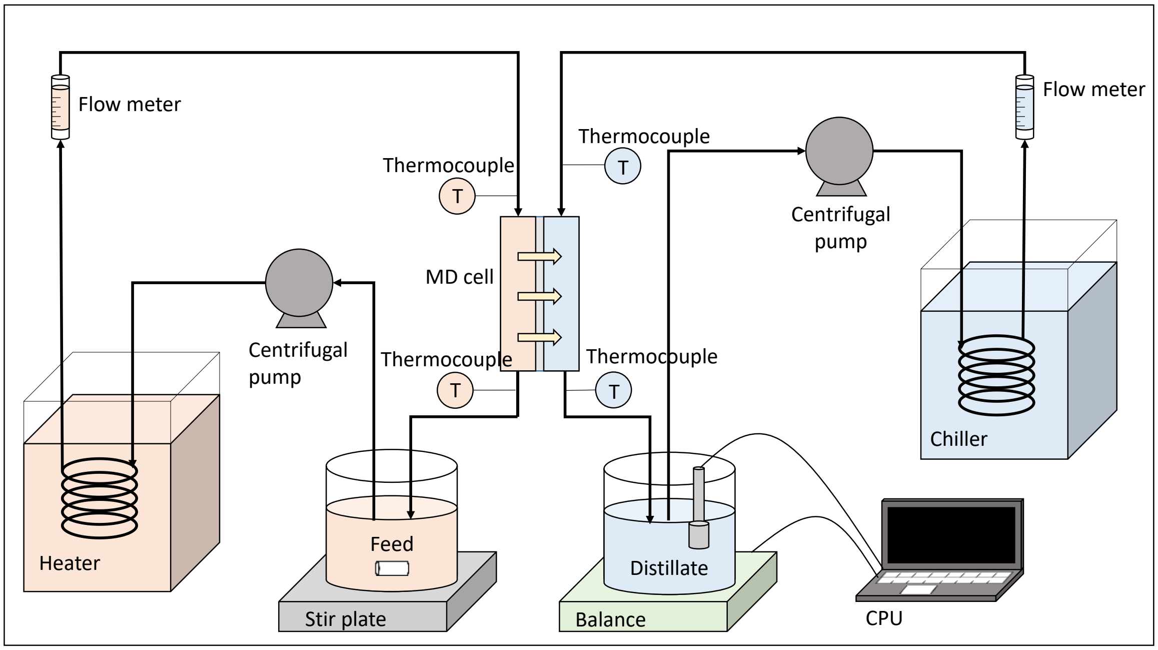

Figure C1 – Setup used for direct-contact membrane distillation (DCMD) experiments.

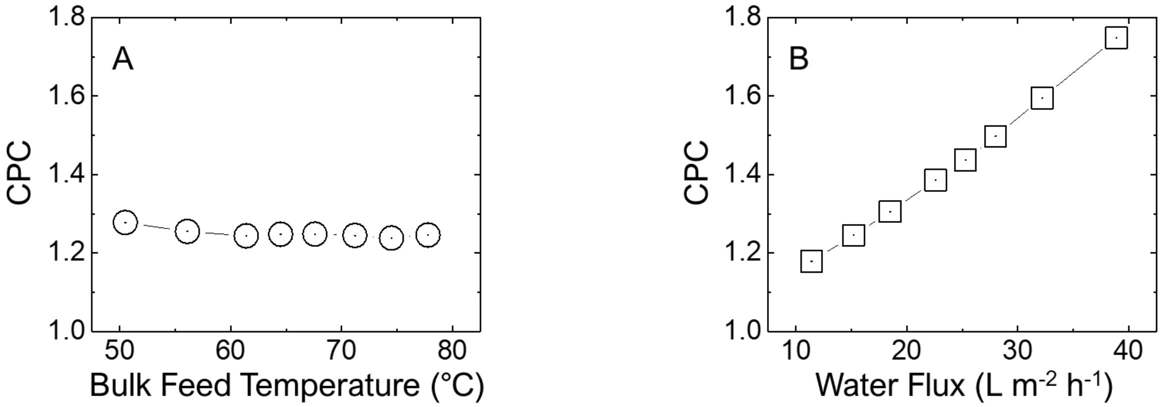

Figure C2 – Concentration polarization coefficients for A) the constant flux series and B) the constant feed temperature series, calculated using the semi-empirical polarization model established using accepted mass and heat transfer correlations.

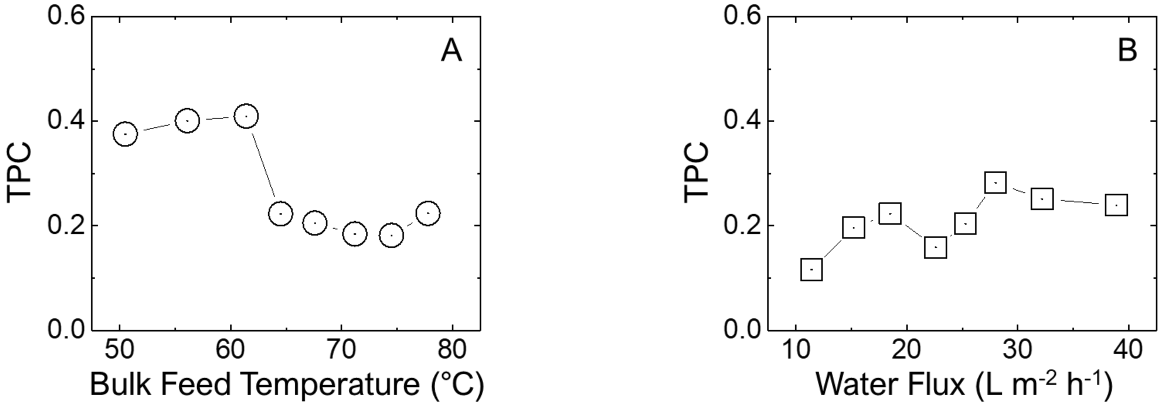

Figure C3 – Temperature polarization coefficients for A) the constant flux series and B) the constant feed temperature series, calculated using the semi-empirical polarization model established using accepted mass and heat transfer correlations.

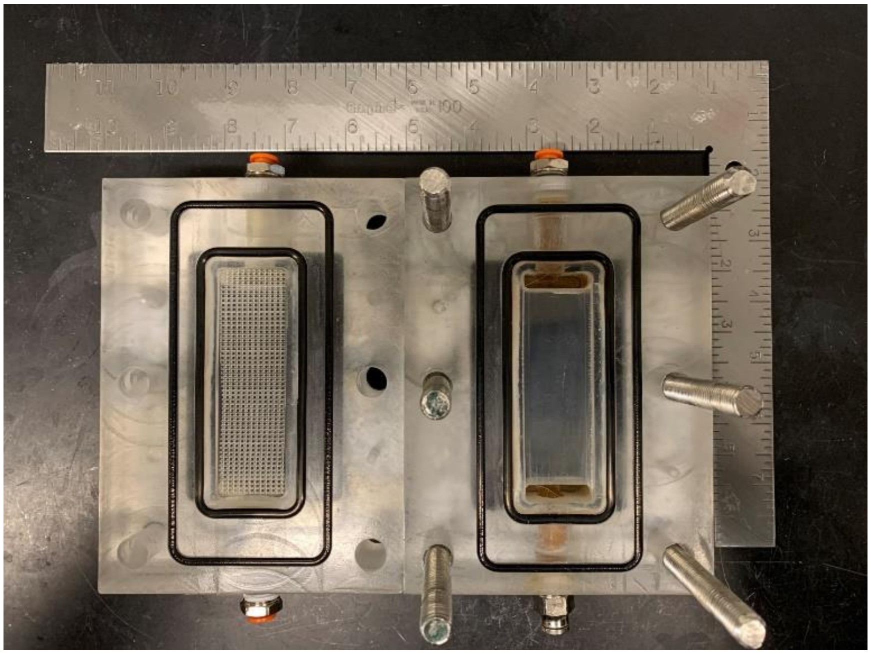

Figure C4 – Test cell used for direct-contact membrane distillation (DCMD) experiments

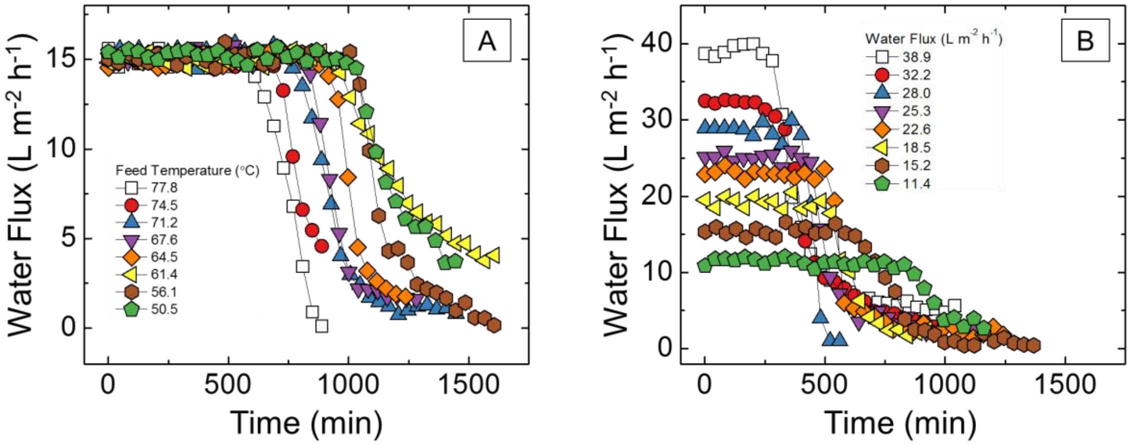

Figure C5 – Water flux versus time plots for A) Series 1 with constant water flux and varied bulk feed temperature and B) Series 2 with constant bulk feed temperature and varied water flux.

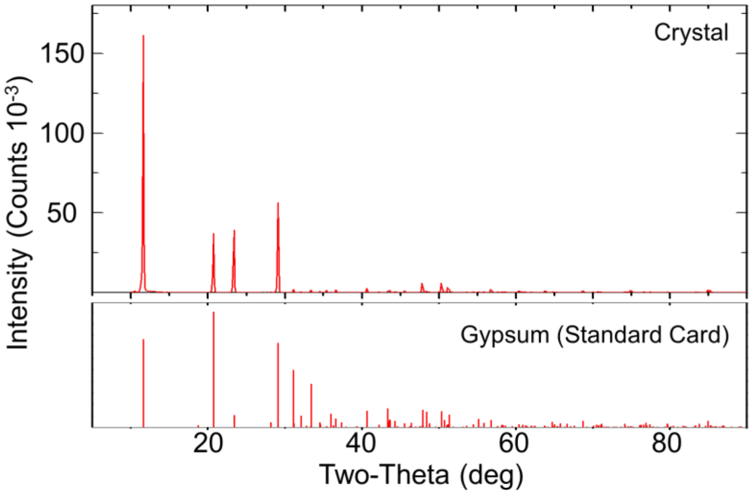

Figure C6 – X-ray powder diffraction (XRD) pattern of the crystals adhered onto the membrane surface.

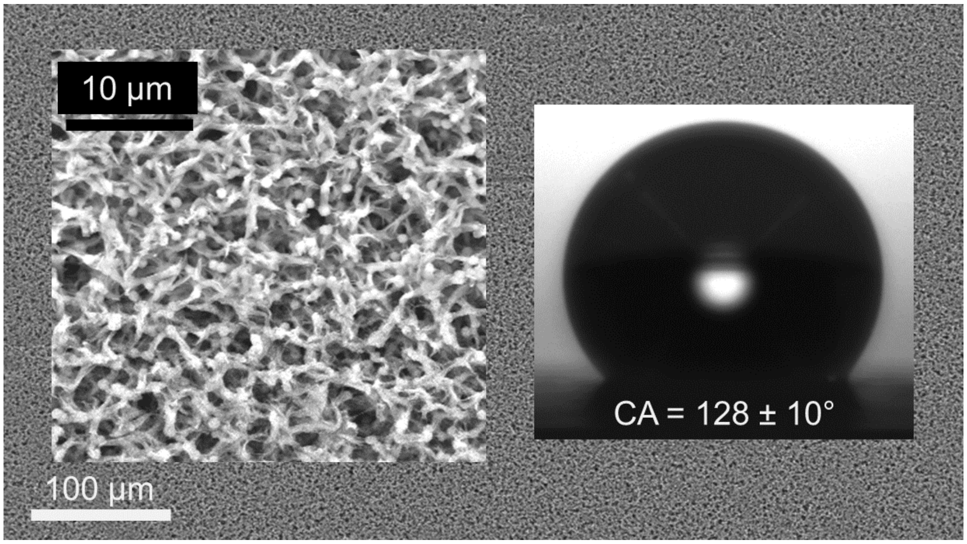

Figure C7 - Scanning electron microscopy (SEM) images and water contact angle of the pristine polyvinylidene fluoride (PVDF) membrane used in this study.

C.2. Matlab Script for Interfacial Temperature and Ion Concentration Calculation

```
%This script calculates interfacial temperature and ion
concentration during DCMD
%-------------------------------------------------------------
----------

close all
clear variables
clc

syms xTmd xTmf

%Inputs
Tbf=[71.8 69.2 70.8 72.4 70.6 71.1 71.1 70.4 77.8 74.5 71.2
67.6 64.5 61.4 56.1 50.5]+273.15;
Tbd=[9.72 20.3 26.3 42.8 47.1 49.0 54.4 60.0 60.1 58.9 55.0
50.2 46.2 19.7 8.99 2.02]+273.15;
%Distillate solution temperature (K)
J_LMH = [38.9 32.2 28.0 25.3 22.6 18.5 15.2 11.4 15.6 15 15.2
15.2 15 14.6 14.9 15.7];
J=LMH_to_molm2s(J_LMH); %flux (mol/m2/s)
C_Ca = 0.020; %Ca ion concentration in bulk solution (M)
C_SO4 = 0.020; %SO4 ion concentration in bulk solution (M)
V = 1; %Solution volume (L)

h=0.0025; %channel height (m)
w=0.025; %channel width (m)
Qf=0.3; %feed flow rate (L/min)
Qd=0.2; %distillate flow rate (L/min)
p=0.70; %membrane porosity (V_pores/V_polymer)
dm=0.00014; %membrane thickness (m)
kg=0.02735; %thermal conductivity of air (W/m/K)
```

```
kpvdf=0.19; %thermal conductivity of pvdf (W/m/K)

cl=d(h,w); %characteristic length/hydraulic diameter;
vf=vel(Qf,h,w); %feed velocity (m/s)
vd=vel(Qd,h,w); %distillate velocity (m/s)
km=k_mem(p,kpvdf,kg); %membrane thermal conductivity (W/m/K)
TbfC=K_to_C(Tbf); %feed temperature (C)
TbdC=K_to_C(Tbd); %distillate temeprature (C)

kf = 0.7; %Feed thermal conductivity (W/m/K) (BSL)
kd = 0.6; %Permeate thermal conductivity (W/m/K) (BSL)
pf = (-4E-6*(TbfC.^2)-5E-5*TbfC+1.005)*1E6; %Feed density
(g/m^3)
pd = (-4E-6*(TbdC.^2)-5E-5*TbdC+1.005)*1E6; %Permeate density
(g/m^3)
A_u = 2.414E-5; %Dynamic viscosity coefficient (Pa*s)
B_u = 247.8; %Dynamic viscosity coefficient (K)
C_u = 140; %Dynamic viscosity coefficient (K)
Pas = 1000; %Pa-s to g/m/s
uf = Pas.*(A_u.*10.^(B_u./(Tbf-C_u))); %Feed viscosity (g/m/s)
(BSL)
ud = Pas.*(A_u.*10.^(B_u./(Tbd-C_u))); %Permeate viscosity
(g/m/s) (BSL)
Cpf = 4.19; %Feed specific heat capacity (J/g/K) (BSL)
Cpd = 4.18; %Permeate specific heat capacity (J/g/K) (BSL)

D_Ca = 1.25E-9; %Molecular diffusivity of calcium ion (m^2/s)
D_SO4 = 1.25E-9; %Molecular diffusivity of sulfate ion (m^2/s)
y_Ca = 0.4; %Activity coeficient of calcium ion
y_SO4 = 0.36; %Activity coeficient of sulfate ion
A = 8.07131; %Antoine parameter
B = 1730.63; %Antoine parameter
C = 233.426; %Antoine parameter
V = 1; %Solution volume (L)
molW = V*1000/18.01528; %Mole fraction of water
xW = molW/(C_Ca*V+C_SO4*V+molW); %Mole fraction of salt
mmHg = 7.50062; %kPa to mmHg

%Calculations to determine Tm
Ref = vf.*cl.*pf./uf; %Feed reynolds number
Red = vd.*cl.*pd./ud; %Permeate reynolds number
Prf = uf*Cpf/kf; %Feed prandtl number
Prd = ud*Cpd/kd; %Permeate prandtl number
A_Nuf = 0.11013019; %Feed Nusselt coefficient
b_Nuf = 0.598524057; %Feed Nusselt coefficient
c_Nuf = 1/3; %Feed Nusselt coefficient
A_Nud = 0.061966464; %Distillate Nusselt coefficient
b_Nud = 0.758561245; %Distillate Nusselt coefficient
c_Nud = 1/3; %Distillate Nusselt coefficient
Nuf = A_Nuf.*Ref.^b_Nuf.*Prf.^c_Nuf; %Feed Nusselt number
Nud = A_Nud.*Red.^b_Nud.*Prd.^c_Nud; %Permeate Nusselt number
Scf = uf./pf./D_Ca; %Feed Schmidt number
Scd = ud./pd./D_Ca; %Distillate Schmidt number
Shf = A_Nuf.*Ref.^b_Nuf.*Scf.^c_Nuf; %Feed Sherwood number
Shd = A_Nud.*Red.^b_Nuf.*Scd.^c_Nud; %Distillate Sherwood
number
ks_Ca = Shf.*D_Ca./cl; %Mass transfer coefficient for calcium
ion
```

```
ks_SO4 = Shd.*D_SO4./cl; %Mass transfer coefficient for
sulfate ion
hf = Nuf*kf/cl; %Feed heat transfer coefficient (W/m2/K)
hd = Nud*kd/cl; %Permeate heat transfer coefficient (W/m2/K)
BLTf = cl./Shf; %Feed boundary layer thickness
BLTd = cl./Shd; %Distillate boundary layer thickness
hm = km/dm; %Membrane heat transfer coefficient (W/m2/K)
hv = (1E-08)*exp(0.0528*Tbf); %Vapor heat transfer coefficient
(W/m2/K)
Hvf = 18.01528*(1.7535*Tbf + 2024.3); %Feed vapor enthalpy
(j/mol)
Hvd = 18.01528*(1.7535*Tbd + 2024.3); %Permeate vapor enthalpy
(j/mol)
Tmf=zeros(1,length(Tbf)); %Blank matrix for Tmf calculation
Tmd=zeros(1,length(Tbd)); %Blank matrix for TmP calculation

for j = 1:length(Tbf)
    W1 = (hm*(Tbd(j)+hf(j)*Tbf(j)/hd(j))+hf(j)*Tbf(j)-
J(j)*Hvf(j))/(hm+hf(j)*(1+hm/hd(j)))-xTmf;
    W2 =
(hm*(Tbf(j)+hd(j)*Tbd(j)/hf(j))+hd(j)*Tbd(j)+J(j)*Hvd(j))/(hm+
hd(j)*(1+hm/hf(j)))-xTmd;
        eqns = [W1==0,W2==0];
        vars = [xTmf,xTmd];
        range = [Tbf(j),Tbd(j)];
    Q = vpasolve(eqns,vars,range);
        Tmf(j) = Q.xTmf;
        Tmd(j) = Q.xTmd;
end

%Calculations to determine Cm
Cm_Ca = C_Ca*exp(J*18E-6./ks_Ca); %Ca ion concentration at
membrane surface (M)
Cm_SO4 = C_SO4*exp(J*18E-6./ks_SO4); %SO4 ion concentration at
membrane surface (M)

%Determine partial vapor pressure
TmfC = Tmf-273.15;TmdC = Tmd-273.15;
xWm = molW./(Cm_Ca*V+Cm_SO4*V+molW); %Mole fraction of salt
vp_f=xW*((1/mmHg)*10.^(A-B./(C+TbfC))); %Partial vapor
pressure of bulk feed (kpa)
vp_d=((1/mmHg)*10.^(A-B./(C+TbdC))); %Partial vapor pressure
of bulk distillate (kpa)
vp_fm=xWm.*((1/mmHg)*10.^(A-B./(C+TmfC))); %Partial vapor
pressure of interfacial feed (kpa)
vp_dm=((1/mmHg)*10.^(A-B./(C+TmdC))); %Partial vapor pressure
of interfacial distillate (kpa)

%Flux
B = (J_LMH)./(vp_fm-vp_dm);
Jm = B.*(vp_fm-vp_dm);

%Display
no_TP = linspace(45,80,length(J));
disp('Tbf, Tbd, Tmf, Tmd, TPC, Cm, CPC, B');
disp([TbfC' TbdC' (Tmf-273.15)' (Tmd-273.15)' ((Tmf-
Tmd)./(Tbf-Tbd))' ...
    Cm_Ca' (Cm_Ca/C_Ca)' B']);
```

```
%Plots
%-------------------------------------------------------------
----------
%Figure 1
figure;
hold on;
set(0,'DefaultFigureWindowStyle','docked')
scatter(Tbf-273.15,Tmf-273.15,200,'linewidth',2)
hold on
      plot(no_TP,no_TP,'linestyle','--
','linewidth',2,'color','r');
      hold off
title('Temperature Polarization'); %Title of plot
xlabel(['Bulk Feed Temperature (' char(0176) 'C)']); %Title of
x-axis
xlim([30 100]);
ylim([30 85]);
ylabel(['Interfacial Feed Temperature (' char(0176) 'C)']);
%Title of y-axis
legend('TP','No TP'); %Title of legend
box on; % Tick marks around plot
legend('boxon'); % Box around legend
grid on; % Grid lines
hold off;

%Figure 2
figure;
hold on;
set(0,'DefaultFigureWindowStyle','docked')
scatter(J*0.018*3600,Cm_Ca.*1000,200,'linewidth',2)
hold on
plot(J*0.018*3600,ones(1,length(J))*C_Ca*1000,'linestyle','--
','linewidth',2,'color','r');
hold off
title('Concentration Polarization'); %Title of plot
xlabel('Flux (LMH)'); %Title of x-axis
xlim([(min(J_LMH)-5) (max(J_LMH)+15)]);
ylim([(min(Cm_Ca)*1000-15) (max(Cm_Ca)*1000+15)]);
ylabel('Interfacial Feed Concentration (mM)'); %Title of y-
axis
legend('CP','No CP'); %Title of legend
box on; %Tick marks around plot
legend('boxon'); %Box around legend
grid on; %Grid lines
hold off;
```

REFERENCES

1. UNESCO. *The United Nations World Water Development Report 2019: Leaving No One Behind*. (2019).
2. Viala, E. Water for food, water for life a comprehensive assessment of water management in agriculture. *Irrig. Drain. Syst.* **22**, 127–129 (2008).
3. Bond, R. & Veerapaneni, S. *Zero liquid discharge for inland desalination*. (2007).
4. Ahmed, M., Hoey, D., Shayya, W. & Goosen, M. F. A. Brine Disposal from Inland Desalination Plants: Current Status, Problems, and Opportunities. *Environ. Sci. Environ. Comput.* **II**, (2004).
5. Frohlich, C. Two-year survey comparing earthquake activity and injection-well locations in the Barnett Shale, Texas. *Proc. Natl. Acad. Sci. U. S. A.* **109**, 13934–13938 (2012).
6. Patnode, K. A., Hittle, E., Anderson, R. M., Zimmerman, L. & Fulton, J. W. Effects of high salinity wastewater discharges on unionid mussels in the allegheny river, Pennsylvania. *J. Fish Wildl. Manag.* **6**, 55–70 (2015).
7. Bond, P. & Veerapaneni, S. Zeroing in on ZLD technologies for inland desalination. *J. / Am. Water Work. Assoc.* **100**, (2008).
8. Miller, J. E. *Review of Water Resources and Desalination Technologies*. (2003).
9. Semiat, R. Energy issues in desalination processes. *Environ. Sci. Technol.* **42**, 8193–8201 (2008).
10. Gude, V. G. Desalination and sustainability - An appraisal and current perspective. *Water Res.* **89**, 87–106 (2016).
11. Likhachev, D. S. & Li, F. C. Large-scale water desalination methods: A review and new perspectives. *Desalin. Water Treat.* **51**, 2836–2849 (2013).
12. Subramani, A. & Jacangelo, J. G. Emerging desalination technologies for water treatment: A critical review. *Water Res.* **75**, 164–187 (2015).
13. Alkhudhiri, A., Darwish, N. & Hilal, N. Membrane distillation: A comprehensive review. *Desalination* **287**, 2–18 (2012).
14. Chang, H. *et al.* Potential and implemented membrane-based technologies for the treatment and reuse of flowback and produced water from shale gas and oil plays: A review. *Desalination* **455**, 34–57 (2019).
15. Warsinger, D. E. M. Thermodynamic Design and Fouling of Membrane Distillation Systems. (Massachussetts Institute of Technology, 2015).
16. Shaffer, D. L. *et al.* Desalination and reuse of high-salinity shale gas produced water: Drivers, technologies, and future directions. *Environ. Sci. Technol.* **47**, 9569–9583 (2013).
17. Deshmukh, A. *et al.* Membrane distillation at the water-energy nexus: Limits, opportunities,

and challenges. *Energy Environ. Sci.* **11**, 1177–1196 (2018).

18. Curcio, E. & Drioli, E. Membrane distillation and related operations - A review. *Sep. Purif. Rev.* **34**, 35–86 (2005).

19. Drioli, E., Ali, A. & Macedonio, F. Membrane distillation: Recent developments and perspectives. *Desalination* **356**, 56–84 (2015).

20. Camacho, L. M. *et al.* Advances in membrane distillation for water desalination and purification applications. *Water (Switzerland)* **5**, 94–196 (2013).

21. Creusen, R. *et al.* Integrated membrane distillation-crystallization: Process design and cost estimations for seawater treatment and fluxes of single salt solutions. *Desalination* **323**, 8–16 (2013).

22. Tong, T. & Elimelech, M. The Global Rise of Zero Liquid Discharge for Wastewater Management: Drivers, Technologies, and Future Directions. *Environ. Sci. Technol.* **50**, 6846–6855 (2016).

23. Semblante, G. U., Lee, J. Z., Lee, L. Y., Ong, S. L. & Ng, H. Y. Brine pre-treatment technologies for zero liquid discharge systems. *Desalination* **441**, 96–111 (2018).

24. Alklaibi, A. M. & Lior, N. Heat and mass transfer resistance analysis of membrane distillation. *J. Memb. Sci.* **282**, 362–369 (2006).

25. Schofield, R. W., Fane, a. G. & Fell, C. J. D. Heat and mass transfer in membrane distillation. *J. Memb. Sci.* **33**, 299–313 (1987).

26. Qtaishat, M., Matsuura, T., Kruczek, B. & Khayet, M. Heat and mass transfer analysis in direct contact membrane distillation. *Desalination* **219**, 272–292 (2008).

27. Termpiyakul, P., Jiraratananon, R. & Srisurichan, S. Heat and mass transfer characteristics of a direct contact membrane distillation process for desalination. *Desalination* **177**, 133–141 (2005).

28. Phattaranawik, J. & Jiraratananon, R. Direct contact membrane distillation: Effect of mass transfer on heat transfer. *J. Memb. Sci.* **188**, 137–143 (2001).

29. Gryta, M. & Tomaszewska, M. Heat transport in the membrane distillation process. *J. Memb. Sci.* **144**, 211–222 (1998).

30. Phattaranawik, J., Jiraratananon, R. & Fane, A. G. Heat transport and membrane distillation coefficients in direct contact membrane distillation. *J. Memb. Sci.* **212**, 177–193 (2003).

31. Martínez-Díez, L., Vázquez-González, M. I. & Florido-Díaz, F. J. Study of membrane distillation using channel spacers. *J. Memb. Sci.* **144**, 45–56 (1998).

32. Martínez-Díez, L. & Vázquez-González, M. I. A method to evaluate coefficients affecting flux in membrane distillation. *J. Memb. Sci.* **173**, 225–234 (2000).

33. Phattaranawik, J., Jiraratananon, R., Fane, A. G. & Halim, C. Mass flux enhancement using spacer filled channels in direct contact membrane distillation. *J. Memb. Sci.* **187**, 193–201 (2001).

34. Cath, T. Y., Adams, V. D. & Childress, A. E. Experimental study of desalination using direct contact membrane distillation: A new approach to flux enhancement. *J. Memb. Sci.* **228**, 5–16 (2004).

35. Swaminathan, J., Chung, H. W., Warsinger, D. M. & Lienhard V, J. H. Membrane distillation model based on heat exchanger theory and configuration comparison. *Appl. Energy* **184**, 491–505 (2016).

36. Swaminathan, J. *et al.* Energy efficiency of permeate gap and novel conductive gap membrane distillation. *J. Memb. Sci.* **502**, 171–178 (2016).

37. Song, L., Li, B., Sirkar, K. K. & Gilron, J. L. Direct contact membrane distillation-based desalination: Novel membranes, devices, larger-scale studies, and a model. *Ind. Eng. Chem. Res.* **46**, 2307–2323 (2007).

38. Cheng, L. H., Wu, P. C. & Chen, J. Modeling and optimization of hollow fiber DCMD module for desalination. *J. Memb. Sci.* **318**, 154–166 (2008).

39. Bui, V. A., Vu, L. T. T. & Nguyen, M. H. Modelling the simultaneous heat and mass transfer of direct contact membrane distillation in hollow fibre modules. *J. Memb. Sci.* **353**, 85–93 (2010).

40. Zuo, G., Wang, R., Field, R. & Fane, A. G. Energy efficiency evaluation and economic analyses of direct contact membrane distillation system using Aspen Plus. *Desalination* **283**, 237–244 (2011).

41. Summers, E. K., Arafat, H. A. & Lienhard V, J. H. Energy efficiency comparison of single-stage membrane distillation (MD) desalination cycles in different configurations. *Desalination* **290**, 54–66 (2012).

42. Swaminathan, J., Chung, H. W., Warsinger, D. M. & Lienhard, J. H. Simple method for balancing direct contact membrane distillation. *Desalination* (2016). doi:10.1016/j.desal.2016.01.014

43. Warsinger, D. M., Mistry, K. H., Nayar, K. G., Chung, H. W. & Lienhard, J. H. V. Entropy generation of desalination powered by variable temperature waste heat. *Entropy* **17**, 7530–7566 (2015).

44. Shannon, M. A. *et al.* Science and technology for water purification in the coming decades. *Nanosci. Technol. A Collect. Rev. from Nat. Journals* **452**, 337–346 (2009).

45. Lee, H., He, F., Song, L., Gilron, J. & Sirkar, K. K. Desalination with a Cascade of Cross-Flow Hollow Fiber Membrane Distillation Devices Integrated with a Heat Exchanger. *Am. Inst. Chem. Eng. J.* **57**, 1780–1795 (2011).

46. Hausmann, A., Sanciolo, P., Vasiljevic, T., Weeks, M. & Duke, M. Integration of membrane distillation into heat paths of industrial processes. *Chem. Eng. J.* **211**–**212**, 378–387 (2012).

47. Maheswari, K. S., Kalidasa Murugavel, K. & Esakkimuthu, G. Thermal desalination using diesel engine exhaust waste heat - an experimental analysis. *Desalination* **358**, 94–100 (2015).

48. Kim, Y. D., Thu, K. & Choi, S. H. Solar-assisted multi-stage vacuum membrane distillation system with heat recovery unit. *Desalination* **367**, 161–171 (2015).

49. Lu, Y. & Chen, J. Integration design of heat exchanger networks into membrane distillation systems to save energy. *Ind. Eng. Chem. Res.* **51**, 6798–6810 (2012).

50. González-Bravo, R., Elsayed, N. A., Ponce-Ortega, J. M., Nápoles-Rivera, F. & El-Halwagi, M. M. Optimal design of thermal membrane distillation systems with heat integration with process plants. *Appl. Therm. Eng.* **75**, 154–166 (2015).

51. Chung, S., Seo, C. D., Lee, H., Choi, J. H. & Chung, J. Design strategy for networking membrane module and heat exchanger for direct contact membrane distillation process in seawater desalination. *Desalination* **349**, 126–135 (2014).

52. Guan, G., Yang, X., Wang, R. & Fane, A. G. Evaluation of heat utilization in membrane distillation desalination system integrated with heat recovery. *Desalination* **366**, 80–93 (2015).

53. Gustafson, R. D., Hiibel, S. R. & Childress, A. E. Membrane distillation driven by intermittent and variable-temperature waste heat: System arrangements for water production and heat storage. *Desalination* **448**, 49–59 (2018).

54. Schofield, R. W., Fane, A. G., Fell, C. J. D. & Macoun, R. Factors affecting flux in membrane distillation. *Desalination* **77**, 279–294 (1990).

55. Lin, S., Yip, N. Y. & Elimelech, M. Direct contact membrane distillation with heat recovery: Thermodynamic insights from module scale modeling. *J. Memb. Sci.* **453**, 498–515 (2014).

56. Bergman, T. L., Lavine, A. S., Incropera, F. P. & Dewitt, D. P. *Fundamentals of Heat and Mass Transfer*. (John Wiley & Sons, Inc., 2011).

57. Lin, S. & Elimelech, M. Kinetics and energetics trade-off in reverse osmosis desalination with different configurations. *Desalination* **401**, 42–52 (2017).

58. Wang, L. & Lin, S. Intrinsic tradeoff between kinetic and energetic efficiencies in membrane capacitive deionization. *Water Res.* **129**, 394–401 (2018).

59. Sandler, S. I. *Chemical, Biochemical, and Engineering Thermodynamics*. (John Wiley & Sons, Inc., 2006).

60. Dongare, P. D. *et al.* Nanophotonics-enabled solar membrane distillation for off-grid water purification. *Proc. Natl. Acad. Sci. U. S. A.* **114**, 6936–6941 (2017).

61. Thomas, N., Mavukkandy, M. O., Loutatidou, S. & Arafat, H. A. Membrane distillation research & implementation: Lessons from the past five decades. *Sep. Purif. Technol.* **189**, 108–127 (2017).

62. Wang, W. *et al.* Trade-off in membrane distillation with monolithic omniphobic membranes. *Nat. Commun.* **10**, 1–9 (2019).

63. Lawson, K. W. & Lloyd, D. R. Membrane distillation. *J. Memb. Sci.* **124**, 1–25 (1997).

64. Lokare, O. R., Tavakkoli, S., Wadekar, S., Khanna, V. & Vidic, R. D. Fouling in direct contact membrane distillation of produced water from unconventional gas extraction. *J. Memb. Sci.* **524**, 493–501 (2017).

65. Gryta, M. Fouling in direct contact membrane distillation process. *J. Memb. Sci.* **325**, 383–394 (2008).

66. Wang, J. *et al.* Effect of coagulation pretreatment on membrane distillation process for desalination of recirculating cooling water. *Sep. Purif. Technol.* **64**, 108–115 (2008).

67. Tijing, L. D. *et al.* Fouling and its control in membrane distillation-A review. *J. Memb. Sci.* **475**, 215–244 (2015).

68. Zhang, Z., Du, X., Carlson, K. H., Robbins, C. A. & Tong, T. Effective treatment of shale oil and gas produced water by membrane distillation coupled with precipitative softening and walnut shell filtration. *Desalination* **454**, 82–90 (2019).

69. Wang, Z., Elimelech, M. & Lin, S. Environmental Applications of Interfacial Materials with Special Wettability. *Environ. Sci. Technol.* **50**, 2132–2150 (2016).

70. Lin, S. *et al.* Omniphobic Membrane for Robust Membrane Distillation. *Environ. Sci. Technol. Lett.* **1**, 443–447 (2014).

71. Lee, J., Boo, C., Ryu, W. H., Taylor, A. D. & Elimelech, M. Development of Omniphobic Desalination Membranes Using a Charged Electrospun Nanofiber Scaffold. *ACS Appl. Mater. Interfaces* **8**, 11154–11161 (2016).

72. Wang, Z., Hou, D. & Lin, S. Composite Membrane with Underwater-Oleophobic Surface for Anti-Oil-Fouling Membrane Distillation. *Environ. Sci. Technol.* **50**, 3866–3874 (2016).

73. Wang, Z. & Lin, S. Membrane fouling and wetting in membrane distillation and their mitigation by novel membranes with special wettability. *Water Res.* **112**, 38–47 (2017).

74. Huang, Y. X., Wang, Z., Jin, J. & Lin, S. Novel Janus Membrane for Membrane Distillation with Simultaneous Fouling and Wetting Resistance. *Environ. Sci. Technol.* **51**, 13304–13310 (2017).

75. Li, C. *et al.* Antiwetting and Antifouling Janus Membrane for Desalination of Saline Oily Wastewater by Membrane Distillation. *ACS Appl. Mater. Interfaces* **11**, 18456–18465 (2019).

76. Tong, T., Wallace, A. F., Zhao, S. & Wang, Z. Mineral scaling in membrane desalination: Mechanisms, mitigation strategies, and feasibility of scaling-resistant membranes. *J. Memb. Sci.* **579**, 52–69 (2019).

77. Warsinger, D. M., Swaminathan, J., Guillen-Burrieza, E., Arafat, H. A. & Lienhard V, J. H. Scaling and fouling in membrane distillation for desalination applications: A review. *Desalination* **356**, 294–313 (2015).

78. Karanikola, V., Boo, C., Rolf, J. & Elimelech, M. Engineered Slippery Surface to Mitigate Gypsum Scaling in Membrane Distillation for Treatment of Hypersaline Industrial Wastewaters. *Environ. Sci. Technol.* **52**, acs.est.8b04836 (2018).

79. Rezaei, M. *et al.* Wetting phenomena in membrane distillation: Mechanisms, reversal, and prevention. *Water Res.* **139**, 329–352 (2018).

80. Gryta, M. Calcium sulphate scaling in membrane distillation process. *Chem. Pap.* **63**, 146–151 (2009).

81. Xiao, Z. *et al.* Scaling mitigation in membrane distillation: From superhydrophobic to slippery. *Desalination* **466**, 36–43 (2019).

82. Zheng, R. *et al.* Slippery for scaling resistance in membrane distillation: a novel porous micropillared superhydrophobic surface. *Water Res.* **155**, 152–161 (2019).

83. Su, C. *et al.* Robust Superhydrophobic Membrane for Membrane Distillation with Excellent Scaling Resistance. *Environ. Sci. Technol.* (2019). doi:10.1021/acs.est.9b04362

84. Kiefer, F., Präbst, A., Rodewald, K. S. & Sattelmayer, T. Membrane scaling in Vacuum Membrane Distillation - Part 1: In-situ observation of crystal growth and membrane wetting. *J. Memb. Sci.* **590**, 117294 (2019).

85. Wang, Z., Chen, Y., Sun, X., Duddu, R. & Lin, S. Mechanism of pore wetting in membrane distillation with alcohol vs. surfactant. *J. Memb. Sci.* **559**, 183–195 (2018).

86. Wang, Z., Chen, Y. & Lin, S. Kinetic model for surfactant-induced pore wetting in membrane distillation. *J. Memb. Sci.* **564**, 275–288 (2018).

87. Neofotistou, E. & Demadis, K. D. Use of antiscalants for mitigation of silica (SiO2) fouling and deposition: Fundamentals and applications in desalination systems. *Desalination* **167**, 257–272 (2004).

88. Tong, T., Zhao, S., Boo, C., Hashmi, S. M. & Elimelech, M. Relating Silica Scaling in Reverse Osmosis to Membrane Surface Properties. *Environ. Sci. Technol.* **51**, 4396–4406 (2017).

89. Yin, Y., Wang, W., Kota, A. K., Zhao, S. & Tong, T. Elucidating mechanisms of silica scaling in membrane distillation: Effects of membrane surface wettability. *Environ. Sci. Water Res. Technol.* **5**, 2004–2014 (2019).

90. Chen, Y., Wang, Z., Jennings, G. K. & Lin, S. Probing Pore Wetting in Membrane Distillation Using Impedance: Early Detection and Mechanism of Surfactant-Induced Wetting. *Environ. Sci. Technol. Lett.* **4**, 505–510 (2017).

91. Mi, B., Elimelech, M., Baoxia, M. I. & Elimelech, M. Gypsum scaling and cleaning in forward osmosis: Measurements and mechanisms. *Environ. Sci. Technol.* **44**, 2022–2028 (2010).

92. Mi, B. & Elimelech, M. Silica scaling and scaling reversibility in forward osmosis. *Desalination* **312**, 75–81 (2013).

93. Xie, M. & Gray, S. R. Gypsum scaling in forward osmosis: Role of membrane surface chemistry. *J. Memb. Sci.* **513**, 250–259 (2016).

94. Parkhurst, D. L. & Appelo, C. A. J. *Description of input and examples for PHREEQC version 3—A computer program for speciation, batch-reaction, one-dimensional transport,*

and inverse geochemical calculations: U.S. Geological Survey Techniques and Methods, book 6, chap. A43, 497 p. United States Geological Survey (2013).

95. Uchymiak, M., Lyster, E., Glater, J. & Cohen, Y. Kinetics of gypsum crystal growth on a reverse osmosis membrane. *J. Memb. Sci.* **314**, 163–172 (2008).

96. Thompson, J. *et al.* Real-time direct detection of silica scaling on RO membranes. *J. Memb. Sci.* **528**, 346–358 (2017).

97. Xie, M. & Gray, S. R. Silica scaling in forward osmosis: From solution to membrane interface. *Water Res.* **108**, 232–239 (2017).

98. Mbogoro, M. M. *et al.* Quantitative 3D Visualization of the Growth of Individual Gypsum Microcrystals: Effect of Ca2+:SO42- Ratio on Kinetics and Crystal Morphology. *J. Phys. Chem. C* **121**, 12726–12734 (2017).

99. Gilron, J., Ladizansky, Y. & Korin, E. Silica fouling in direct contact membrane distillation. *Ind. Eng. Chem. Res.* **52**, 10521–10529 (2013).

100. Wang, Z., Chen, Y., Zhang, F. & Lin, S. Significance of surface excess concentration in the kinetics of surfactant-induced pore wetting in membrane distillation. *Desalination* **450**, 46–53 (2019).

101. Wang, X. *et al.* Molecular dynamics simulation of the surface tension of aqueous sodium chloride: From dilute to highly supersaturated solutions and molten salt. *Atmos. Chem. Phys.* **18**, 17077–17086 (2018).

102. Christenson, H. K. Two-step crystal nucleation via capillary condensation. *CrystEngComm* **15**, 2030–2039 (2013).

103. Kashchiev, D. & Firoozabadi, A. Nucleation of gas hydrates. *J. Cryst. Growth* **243**, 476–489 (2002).

104. Wu, W. & Nancollas, G. H. Interfacial free energies and crystallization in aqueous media. *J. Colloid Interface Sci.* **182**, 365–373 (1996).

105. Correns, C. W. Growth and Dissolution of Crystals Under Linear Pressure. *Discuss. Faraday Soc.* 267–271 (1949).

106. Ping, X. & Beaudoin, J. J. Mechanism of sulphate expansion I. Thermodynamic principle of crystallization pressure. *Cem. Concr. Res.* **22**, 631–640 (1992).

107. Scherer, G. W. Stress from crystallization of salt. *Cem. Concr. Res.* **34**, 1613–1624 (2004).

108. Flatt, R. J., Steiger, M. & Scherer, G. W. A commented translation of the paper by C.W. Correns and W. Steinborn on crystallization pressure. *Environ. Geol.* **52**, 187–195 (2007).

109. Steiger, M. Crystal growth in porous materials - I: The crystallization pressure of large crystals. *J. Cryst. Growth* **282**, 455–469 (2005).

110. Belton, D. J., Deschaume, O. & Perry, C. C. An overview of the fundamentals of the chemistry of silica with relevance to biosilicification and technological advances. *FEBS J.* **279**, 1710–1720 (2012).

111. Brinker, C. J. & Scherer, G. W. Sol → gel → glass: I. Gelation and gel structure. *J. Non. Cryst. Solids* **70**, 301–322 (1985).

112. Dietler, G., Aubert, C., Cannell, D. S. & Wiltzius, P. Gelation of colloidal silica. *Phys. Rev. Lett.* **57**, 3117–3120 (1986).

113. Lai, C. Y., Groth, A., Gray, S. & Duke, M. Preparation and characterization of poly(vinylidene fluoride)/nanoclay nanocomposite flat sheet membranes for abrasion resistance. *Water Res.* **57**, 56–66 (2014).

114. Tsai, H. A. *et al.* Effect of DGDE additive on the morphology and pervaporation performances of asymmetric PSf hollow fiber membranes. *J. Memb. Sci.* **208**, 233–245 (2002).

115. Shi, L. *et al.* Fabrication of poly(vinylidene fluoride-co-hexafluropropylene) (PVDF-HFP) asymmetric microporous hollow fiber membranes. *J. Memb. Sci.* **305**, 215–225 (2007).

116. Dydo, P., Turek, M., Ciba, J., Wandachowicz, K. & Misztal, J. The nucleation kinetic aspects of gypsum nanofiltration membrane scaling. *Desalination* **164**, 41–52 (2004).

117. Packter, A. The precipitation of calcium sulphate dihydrate from aqueous solution. *J. Cryst. Growth* **21**, 191–194 (1974).

118. Zhang, P., Knötig, P., Gray, S. & Duke, M. Scale reduction and cleaning techniques during direct contact membrane distillation of seawater reverse osmosis brine. *Desalination* **374**, 20–30 (2015).

119. He, F., Sirkar, K. K. & Gilron, J. L. Effects of antiscalants to mitigate membrane scaling by direct contact membrane distillation. *J. Memb. Sci.* **345**, 53–58 (2009).

120. Gryta, M. Calcium sulphate scaling in membrane distillation process. *Chem. Pap.* **63**, 146–151 (2009).

121. Peng, Y., Ge, J., Li, Z. & Wang, S. Effects of anti-scaling and cleaning chemicals on membrane scale in direct contact membrane distillation process for RO brine concentrate. *Sep. Purif. Technol.* **154**, 22–26 (2015).

122. Hasson, D. & Cornel, A. Effect of residence time on the degree of CaCO3precipitation in the presence of an anti-scalant. *Desalination* **401**, 64–67 (2017).

123. Horseman, T., Su, C., Christie, K. S. S. & Lin, S. Highly Effective Scaling Mitigation in Membrane Distillation Using a Superhydrophobic Membrane with Gas Purging. *Environ. Sci. Technol. Lett.* (2019). doi:10.1021/acs.estlett.9b00354

124. Antony, A. *et al.* Scale formation and control in high pressure membrane water treatment systems: A review. *J. Memb. Sci.* **383**, 1–16 (2011).

125. Greenlee, L. F., Lawler, D. F., Freeman, B. D., Marrot, B. & Moulin, P. Reverse osmosis desalination: Water sources, technology, and today's challenges. *Water Res.* **43**, 2317–2348 (2009).

126. Le Gouellec, Y. A. & Elimelech, M. Calcium sulfate (gypsum) scaling in nanofiltration of agricultural drainage water. *J. Memb. Sci.* **205**, 279–291 (2002).

127. Nghiem, L. D. & Cath, T. A scaling mitigation approach during direct contact membrane distillation. *Sep. Purif. Technol.* **80**, 315–322 (2011).

128. Anvari, A., Kekre, K. M. & Ronen, A. Scaling mitigation in radio-frequency induction heated membrane distillation. *J. Memb. Sci.* **600**, 117859 (2020).

129. Khayet, M. & Matsuura, T. *Membrane Distillation: Principles and Applications*. (2011).

130. Leitch, M. E., Lowry, G. V. & Mauter, M. S. Characterizing convective heat transfer coefficients in membrane distillation cassettes. *J. Memb. Sci.* **538**, 108–121 (2017).

131. Abdel-Aal, E. A., Rashad, M. M. & El-Shall, H. Crystallization of calcium sulfate dihydrate at different supersaturation ratios and different free sulfate concentrations. *Cryst. Res. Technol.* **39**, 313–321 (2004).

132. Marshall, W. L. & Slusher, R. Thermodynamics of calcium sulfate dihydrate in aqueous sodium chloride solutions, 0-110°. *J. Phys. Chem.* **70**, 4015–4027 (1966).

133. Barba, D., Brandani, V. & di Giacomo, G. A thermodynamic model of CaSO4 solubility in multicomponent aqueous solutions. *Chem. Eng. J.* **24**, 191–200 (1982).

134. Budz, J., Jones, A. G. & Mullin, J. W. Effect of selected impurities on the continuous precipitation of calcium sulphate (gypsum). *J. Chem. Technol. Biotechnol.* **36**, 153–161 (1986).

135. Marshall, W. L. & Slusher, R. Aqueous Systems at High Temperature: Solubility to 200° C. of Calcium Sulfate and Its Hydrates in Sea Water and Saline Water Concentrates, and Temperature-Concentration Limits. *J. Chem. Eng. Data* **13**, 83–93 (1968).

136. Hoang, T. A., Ang, H. M. & Rohl, A. L. Effects of temperature on the scaling of calcium sulphate in pipes. *Powder Technol.* **179**, 31–37 (2007).

137. Nayar, K. G., Sharqawy, M. H., Banchik, L. D. & Lienhard, J. H. Thermophysical properties of seawater: A review and new correlations that include pressure dependence. *Desalination* **390**, 1–24 (2016).

138. Alimi, F. & Gadri, A. Kinetics and morphology of formed gypsum •. *Desalination* **166**, 427–434 (2004).

139. Klepetsanis, P. G., Dalas, E. & Koutsoukos, P. G. Role of Temperature in the Spontaneous Precipitation of Calcium Sulfate Dihydrate. *Langmuir* **15**, 1534–1540 (1999).

140. Song, L. *et al.* Pilot plant studies of novel membranes and devices for direct contact membrane distillation-based desalination. *J. Memb. Sci.* **323**, 257–270 (2008).

141. Adham, S., Hussain, A., Matar, J. M., Dores, R. & Janson, A. Application of Membrane Distillation for desalting brines from thermal desalination plants. *Desalination* **314**, 101–108 (2013).

142. Alimi, F. & Gadri, A. Kinetics and morphology of formed gypsum. *Desalination* **166**, 427–434 (2004).

143. Alimi, F., Elfil, H. & Gadri, A. Kinetics of the precipitation of calcium sulfate dihydrate in

a desalination unit. *Desalination* **158**, 9–16 (2003).

144. He, F., Gilron, J., Lee, H., Song, L. & Sirkar, K. K. Potential for scaling by sparingly soluble salts in crossflow DCMD. *J. Memb. Sci.* **311**, 68–80 (2008).

145. Prisciandaro, M., Lancia, A. & Musmarra, D. Calcium sulfate dihydrate nucleation in the presence of calcium and sodium chloride salts. *Ind. Eng. Chem. Res.* **40**, 2335–2339 (2001).

146. Kashchiev, D. & van Rosmalen, G. M. Review: Nucleation in solutions revisited. *Cryst. Res. Technol.* **38**, 555–574 (2003).

147. Bansal, B., Chen, X. D. & Müller-Steinhagen, H. Analysis of ‘classical’ deposition rate law for crystallisation fouling. *Chem. Eng. Process. Process Intensif.* **47**, 1201–1210 (2008).

148. Chong, T. H. & Sheikholeslami, R. Thermodynamics and kinetics for mixed calcium carbonate and calcium sulfate precipitation. *Chem. Eng. Sci.* **56**, 5391–5400 (2001).